Linking Lasers and Mass Spectrometers: Investigating CID+UV as a New Fragmentation Tool for Analytical Chemistry of Biomolecules

Alexander Patrick Hawes

MSc by Research

University of York

Chemistry

July 2015

Abstract

Fragmentation methods in tandem mass spectrometry are of critical importance for the analysis of biomolecular ions, and the development of new tools to effect fragmentation is therefore an area of great current interest. In this thesis, a potential new tool for initiating biomolecule fragmentation is investigated. This method combines low-energy collision induced dissociation, CID, with UV diode (375 nm) irradiation as a single fragmentation tool, named CID+UV. Initial experiments were conducted on the nucleobases uracil, adenine, thymine and cytosine complexed to an iodide ion. The results showed a significant increase in the amount of depletion of I$^-$·uracil and I$^-$·adenine using CID+UV when compared to conventional low-energy CID fragmentation, while I$^-$·thymine and I$^-$·cytosine showed no detectable enhanced depletion. To further investigate the possible fragmentation processes operating, UV laser photodissociation spectra of the I$^-$·uracil and I$^-$·thymine clusters were obtained. These spectra displayed strong absorptions associated with excitation of nucleobase centred chromophores, associated with production of an I$^-$ photofragment. CID+UV fragmentation was also tested as a fragmentation tool on the proteins melittin and angiotensin I human acetate. Melittin proved to be unsuitable for the experimental setup due to its m/z being beyond the range of the mass spectrometer. Angiotensin I human acetate showed several peaks unique for the CID+UV mass spectrum against the conventional CID results, demonstrating the potential of the new CID+UV as a new fragmentation tool.

Contents

List of Figures

Figure 2.4: Diagram of a 3D quadrupole ion trap highlighting the three hyperbolic electrodes and the stable orbit of isolated ions formed by the effects of the electric fields with exit to detector marked on diagram. Taken from Ref 35.

Figure 2.5: Diagram showing energy levels involved in the emission of a laser beam of 946 nm, 1064 nm and 1322 nm. Taken from Ref 39.

Figure 3.1: Diagram of the abinitio calculated structure of $U{\cdot}I^{-}$ with the arrow indicator the dipole direction for the nucleobase. Hydrogen bond lengths are marked on the diagram as is the atom numbering scheme with 1,3 representing nitrogen and 2,4,5,6 representing carbon. Taken from Ref 41.

Figure 3.2: Diagram of the abinitio calculated structure of the (a) $T{\cdot}I^{-}$ and (b) $U{\cdot}I^{-}$ complexes with bond distances for the hydrogen bond lengths labelled. Also, atom numbering is shown with 1,3 representing nitrogen, and 2,4,5,6 representing carbon. Taken from Ref 42.

Figure 3.3: Negative ion mode ESI-MS of the $U{\cdot}I^{-}$ complex. Peaks; 110.9 m/z, 126.9 m/z, 238.9 m/z represent $[U\text{-}H]^{-}$, I^{-} and $U{\cdot}I^{-}$ respectively.

Figure 3.4: Negative ion mode ESI-MS of the $T{\cdot}I^{-}$ complex. Peaks; 125.0 m/z, 126.8 m/z, 252.9 m/z represent $[T\text{-}H]^{-}$, I^{-} and $T{\cdot}I^{-}$ respectively. Zoomed section represented by insert highlights peak m/z.

Figure 3.5: Negative ion mode ESI-MS of the $A{\cdot}I^{-}$ complex. Peaks; 126.8 m/z, 134.0 m/z, 261.9 m/z represent I^{-}, $[A\text{-}H]^{-}$ and $A{\cdot}I^{-}$ respectively.

Figure 3.6: Negative ion mode ESI-MS of the $C{\cdot}I^-$ complex. Peaks; 110.1 m/z, 126.8 m/z, 237.9 m/z represent $[C\text{-}H]^-$, I^- and $C{\cdot}I^-$ respectively.

Figure 3.7: Mass spectrum of $U{\cdot}I^-$ complex, CID excitation energy 0.34 V. Peaks at 126.8 m/z, 239.1 m/z represent I^- and $U{\cdot}I^-$ respectively.

Figure 3.8: Mass spectrum of $T{\cdot}I^-$ complex, CID excitation energy 0.34 V. Peaks at 126.8 m/z, 253.2 m/z represent I^- and $T{\cdot}I^-$ respectively.

Figure 3.9: Mass spectrum of $A{\cdot}I^-$ complex, CID excitation energy 0.34 V. Peaks at 126.8 m/z, 261.9 m/z represent I^- and $A{\cdot}I^-$ respectively.

Figure 3.10: Mass spectrum of $C{\cdot}I^-$ complex, CID excitation energy 0.34 V. Peaks at 126.8 m/z, 237.9 m/z represent I^- and $C{\cdot}I^-$ respectively.

Figure 3.11: % fragmentation curves for $U{\cdot}I^-$. Square symbols represent intensity of parent complex $U{\cdot}I^-$ while circle symbols represent intensity of fragment I^-.The E_h is 0.20-0.21 V. An average variation of less than 5% recorded between repeats.

Figure 3.12: % fragmentation curves for $T{\cdot}I^-$. Square symbols represent intensity of parent complex $T{\cdot}I^-$ while circle symbols represent intensity of fragment I^-. The E_h is 0.12-0.13 V. An average variation of less than 10% recorded between repeats.

Figure 3.13: % fragmentation curves for $A{\cdot}I^-$. Square symbols represent intensity of parent complex $A{\cdot}I^-$ while circle symbols represent intensity of fragment I^-. The E_h is 0.29-0.30 V. An average variation of less than 8% recorded between repeats.

Figure 3.14: % fragmentation curves for $C^{\cdot}I^{-}$. Square symbols represent intensity of parent complex $C^{\cdot}I^{-}$ while circle symbols represent intensity of fragment I^{-}. The E_h is 0.12-0.13 V. An average variation of less than 9% recorded between repeats.

Figure 3.15: % decay curves for $U^{\cdot}I^{-}$. Open symbols represent CID data and closed symbols represent CID+UV data. The three lines on the graph split the data into the four different sections with S1 ranging from 0.00-0.12 V, S2 from 0.13-0.24 V, S3 from 0.25-0.28 V and S4 which ranges from 0.29-0.40 V. An average variation for CID+UV of less than 8% recorded between repeats.

Figure 3.16: Expanded view of regions S3 and S4 from Fig.3.15 highlighting difference in parent intensity between the CID and CID+UV curves.

Figure 3.17: The change in parent peak intensity for the $U^{\cdot}I^{-}$ complex for CID of the selected data point (X) in respect to the previous data point (X-1) using the formula: (X-1) – X = Change in intensity. Peaks labelled A-C are maximum changes in intensity at points 0.12, 0.19 and 0.22 V respectively while peak D is less distinct and resides between the values 0.33-0.35 V.

Figure 3.18: The change in parent peak intensity for the $U^{\cdot}I^{-}$ complex for CID+UV of the selected data point (X) in respect to the previous data point (X-1) using the formula: (X-1) – X = Change in intensity. Peak labelled E is a maximum change in intensity at point 0.13 V while peak F is less distinct and resides between the values 0.30-0.32 V.

Figure 4.5: Negative ion photofragment mass spectrum of the solution $T{\cdot}I^{-}$ complex. Laser set at 260 nm with energy 0.4 mJ. Peaks 252.6 m/z, 126.6 m/z represent $T{\cdot}I^{-}$ and I^{-} respectively.

Figure 4.6: Photodepletion (absorption) spectra of $T{\cdot}I^{-}$ complex parent peak across the 3.6−5.8 eV range.

Figure 4.7: Photodepletion (absorption) spectra of $T{\cdot}I^{-}$ complex parent peak across the 3.5−5.5 eV range.

Figure 5.1: The sequence of amino acids in angiotensin. Taken from Ref 64. Asp, aspartic acid, Arg, argenine, Val, valine, Tyr, tyrosine, Ile, isoleucine, His, histidine, Pro, proline, Phe, phenylalanine, Leu, leucine.

Figure 5.2: Mass spectrum of $[M\text{-}2H]^{2-}$ angiotensin after laser irradiation of 262 nm with parent peak of 647.25 m/z with zoomed insert highlighting doubly deprotonated singly charged angiotensin. Taken from Ref 66.

Figure 5.3: a) MS^3 of the isolated $[M\text{-}2H]^{2-\cdot}$ Fragment and subsequent CID fragmentation with insert highlighting isolated peak. The isolated fragment was formed via UV ionization of the $[M\text{-}2H]^{2-}$ parent peak. b) MS^2 of $[M\text{-}H]^{-}$ parent ion with subsequent CID fragmentation with insert highlighting isolated peak. Significant differences in fragment mass spectra are clearly observed between the two methods. Taken from Ref 66.

Figure 5.4: Mass spectrum of melittin solution with high resolution.

List of Tables

Acknowledgements

I would like to take this opportunity to thank my supervisor Dr Caroline Dessent for both accepting me onto this course and her support throughout this thesis. I would also like to thank Dr Naruo Yoshikawa for his continuing support and, far more importantly, his enduring patience.

Author's Declaration

I hereby certify that the content presented in this thesis is of my own work and, to the best of my knowledge, is original except where referenced otherwise.

This work has not previously been presented for an award at this, or any other, University.

Chapter 1: Introduction

1.1 Fragmentation Methods in Tandem Mass Spectrometry

Mass spectrometry is an important analytical technique with a variety of present day uses and applications since its invention a century ago[1,2,3,4]. For modern day research using mass spectrometers ion fragmentation techniques are of vital importance. This is especially true for the study of gas phase ions where the target ions are fragmented using one of a variety of different methods and the resulting peaks analysed to characterise the parent structure[5]. Without the ability to fragment an isolated parent peak there is little structural information that can be ascertained. This importance becomes even greater when dealing with soft ionization techniques such as electrospray ionization, ESI, which is classified as the softest ionization technique able to presently couple to a mass spectrometer[5,6]. In electrospray ionization mass spectrometry, ESI-MS, often only the parent ion will be present in the parent mass spectrum, since the technique is soft enough to transfer the parent ion to the gas phase without fragmentation[6].

The information gathered using fragmentation in a mass spectrometer is an essential process in the sequencing of biomolecules and allows researchers to probe the structure and hence functionality of a large variety of biological ions. As biomolecules can take on a large variety of different forms from small simple structures through to large proteins the chosen method for inducing fragmentation is of great importance, with different methods creating differing resulting fragment mass spectra, Fig.1.1.

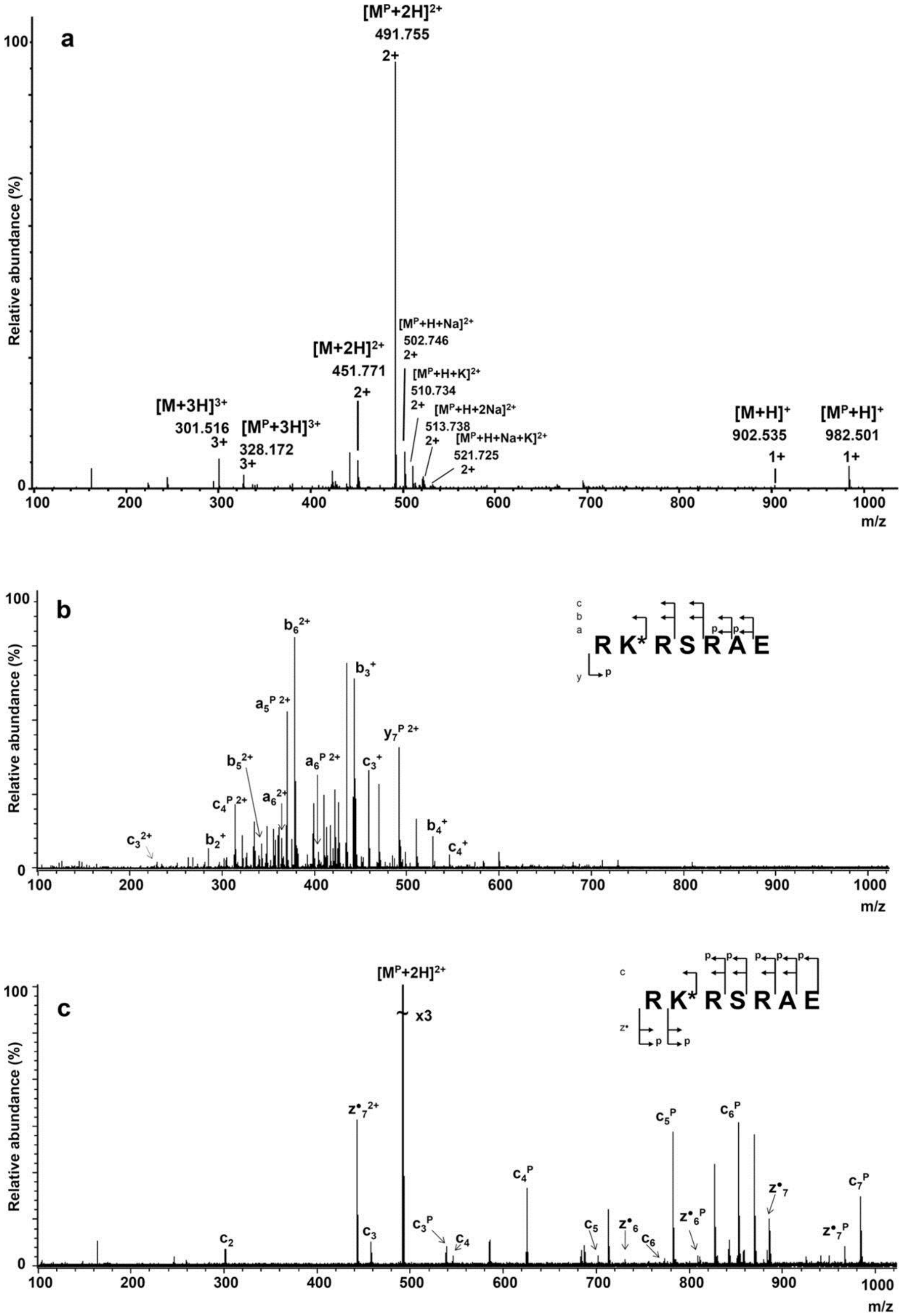

Figure 1.1: Results of phosphorylated RK^{P}RSRAE peptide taken from Ref 7 to highlight differences between fragmentation methods, recorded for CID and ECD. A: ESI mass spectrum. B: CID fragmentation spectrum. C: ECD fragmentation spectrum.

There are a variety of factors that control the differences between different fragmentation techniques and their ability to fragment different biomolecular ions. The maximum possible energy that a fragmentation method can introduce to a target ion is considered a limiting factor as the more strongly bound a biomolecule is the greater the amount of energy to induce fragmentation will be required[8,9]. A second important factor regarding the choice of fragmentation method is the range that the energy can scan across, by analysing a target ion across multiple points onset energies for different fragments can be recorded[8,9]. The different methods of fragmentation also have different timeframes specific to each one which also have to be considered against the limitations of the spectroscope in use, a selection of common methods are displayed in Fig.1.2 to emphasize the contrast.

Common fragmentation techniques include both low and high energy collision induced dissociation[9,10,11,12], CID, also known as collision activated dissociation, CAD, electron capture dissociation[10,13,14,15,16], ECD, and electron detachment dissociation[11,17], EDD.

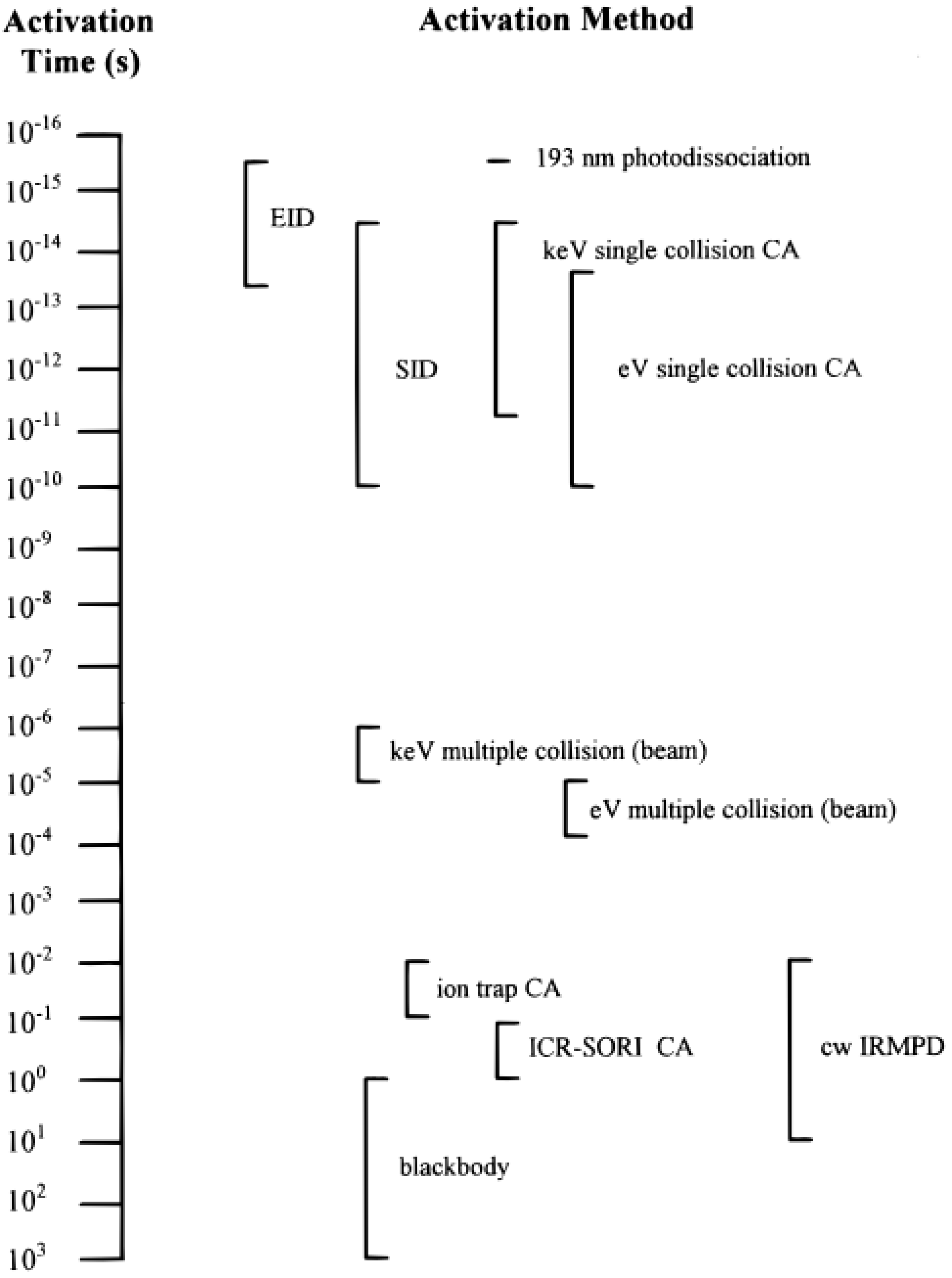

Figure 1.2: Activation times for common activation methods. EID; Electron Induced Dissociation, SID; Surface Induced Dissociation, CA; Collisional Dissociation, IRMPD; Infra-Red Multiple Photon Dissociation, ICR-SORI CA; Ion Cyclotron Resonance Sustained Off-Resonance Irradiation Collisional Activation. Taken from Ref 8.

Low-energy CID is a process in which a target ion isolated inside the quadrupole ion trap of a tandem mass spectrometer is subjected to an electric field to accelerate it into a neutral buffer gas molecule. The impact transfers some of the kinetic energy from the target ion into internal energy which is quickly redistributed across all available bonds. By repeating this process multiple times a significant amount of energy can be transferred which can lead to bond breakage and ion fragmentation[9,10]. The total energy transferred can be easily varied by changing either the length of activation time or the strength of the electric field which leads to either more or less collisions over a total time frame or collisions with either a higher or lower collision energy respectively. The mechanisms at work for the CID of ions <500 Da has been researched in great detail with important work spanning throughout the last half a century[9,10]. However, the energy transfer mechanisms regarding ions >1000 Da, which for biomolecules includes ions of both peptides and proteins, is still unclear and under investigation to the present day[9,10].

The process of low-energy CID is a two-step process where the energy is firstly transferred onto the target ion via collisions to create an unstable yet excited state ion followed by the second step where the excited target ion breaks down into fragments[11]. An advantage of the intermediate excited state is that it allows an opportunity for the target ion to be influenced by a secondary source of energy, such as irradiation via photons from a laser beam and is an important factor regarding the work to combined CID and UV in this thesis. The low-energy CID method is the fragmentation process that is used in the mass spectrometers in this thesis and is explained in further detail in Section 2.1.4.

ECD can be used with a large range of different target ions with the positive, negative and neutral states all possible. However, for the detection of fragments in a mass spectrometer this commonly limits this potential just to polycationic parent target ions to produce singly charged positive ion fragments[13]. Additionally, polycationic parent ions are more commonly used with ECD as the electron capture cross section for a target ion is proportional to the square of the ion charge[14]. The process of ECD is the use of a heated filament to introduce low energy electrons, <0.2eV, to the isolated target ion[10,11,13,14]. The addition of this electron to a polycationic state causes charge neutralisation which generates a significant amount of energy which can transform into internal energy and lead to specific bond cleavage of the target ion structure backbone[15,18]. This method creates radical target ions and as such is a bond specific fragmentation tool for mass spectrometry[15,18]. For ECD in peptides the ‘hot hydrogen atom model’ is introduced to explain the mechanism that occurs. In this model after electron absorption a hydrogen radical is cleaved from the target ion with a high excess energy (~6 eV). This high energy hydrogen atom can transfer along the peptide and induce bond cleavage mainly regarding N-C_α and S-S bonds[11,15].

EDD is similar to ECD but with a detachment of an electron as the result[11,17]. As such, EDD is more commonly used in combination with polyanionic target ions to create singly charged negative ion fragments, effectively electron ionization[11]. What specifically determines this ionization as EDD is the ability to form local positive radical ions on a peptide chain, leading to charge neutralisation with a local electron and energy created which is capable of cleaving the backbone bonds and fragmenting the target ion[11]. Despite the similarities between ECD and

EDD, however, both methods are capable of producing different fragment mass spectra[17].

1.2 Mass Spectrometer Laser Fragmentation Methods

The use of lasers of a variety of different wavelengths in combination with tandem mass spectrometers has created additional methods for the fragmentation of target ions. By absorbing either a single photon or multiple photons target ions can become excited which can lead to a variety of different reaction mechanisms dependant on the fragmentation method selected[19,20,21,22,23]. These laser induced fragmentation methods have the potential to form different fragment peaks in the mass spectra compared to collision induced and electron based fragmentation methods. Two common and significantly different laser fragmentation methods are infrared multiphoton dissociation, IRMPD[10,19], and ultraviolet photodisociation, UVPD[10,24].

IRMPD is the process of irradiating a target ion with multiple photons in the infra-red wavelength to excite upwards through the vibrational levels until dissociation occurs[19], most commonly used is a CO_2 laser which produces a continuous wave laser beam at 10.6 µm[10,19]. IRMPD can be thought of as being the laser equivalent of CID in such a way that it requires a two-step process where multiple photons are necessary to excite the target ion up through the vibrational energy levels in the first step and then the excited ion fragments in the second step[10]. Due to the, on average, considerably longer activation time required compared to other fragmentation methods IRMPD is more commonly coupled with a Fourier transform ion cyclotron mass spectrometer where the ions are capable of being isolated for longer periods of time[25].

UVPD is the process of using a UV laser beam to ionize an electron to a point of excitement above its binding energy, thus removing the electron and leaving the target ion in an oxidised state[19,21,24,26]. The fragmentation that can then occur for UVPD is different from the methods described above as once the target ion has become oxidised in the first step it can either carry on to fragment independently or the oxidised ion can be stable enough that a second stage of isolation can be conducted using the tandem properties of the mass spectrometer and a different source of energy can be used to input energy and fragment the ion, most commonly CID[21,24,26] which is referred to as activated-UVPD.

1.3 Aims of Thesis

Chapters 3, 4 and 5 of this thesis each contain different aims and direction regarding the research that was undertook. The aim of Chapter 3 and 5 was to research the potential of combining CID and UV light from a 375 nm diode laser as a new fragmentation tool for the fragmentation of biomolecules using tandem mass spectrometry. Chapter 3 used nucleobases complexed to iodide while Chapter 5 used doubly deprotonated proteins melittin and angiotensin I human acetate to analyse the effects of the CID+UV tool.

The aim of Chapter 4 was to further analyse the reaction mechanisms of $\mathrm{I}^{-}\cdot$uracil and $\mathrm{I}^{-}\cdot$thymine complexes when irradiated with UV photons of varying wavelengths.

Chapter 2: Experimental Setup

2.1.1 Mass Spectrometer

The two mass spectrometers used in this project are the Bruker AmaZon SL and the Bruker Esquire 6000, referred to henceforth as the AmaZon and Esquire respectively. Both mass spectrometers are electrospray ionization quadrupole ion trap mass spectrometers that use low-energy CID as a fragmentation tool. The mass spectrometers used in this thesis are standard commercial units that have been altered to allow for a laser beam to enter the ion trap.

The AmaZon operates for a *m/z* range of 50-2200 at a scan rate of 8100 *m/z/sec* while the Esquire operates at a *m/z* range 50-3000 and at an identical scan rate.

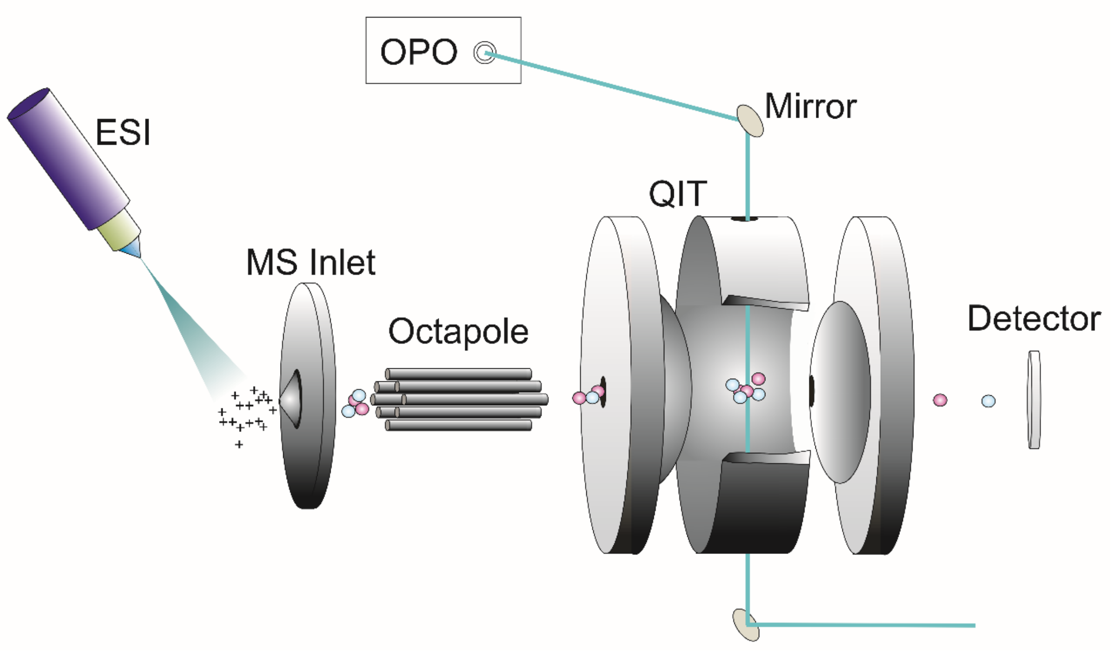

Figure 2.1: Schematic diagram of the mass spectrometer fundamental components. Diagram designed by N. Yoshikawa of the University of York.

2.1.2 Electrospray Ionization

Electrospray ionisation, ESI, is an atmospheric pressure based process in which ions are transferred from a solution to the gas phase[6,28,29]. The process is labelled soft ionization meaning that the ions that originate in solution arrive in the mass spectrometer with little or no fragmentation of their structure. ESI can be operated in both positive and negative modes allowing for both cations and anions to be analysed respectively and allows for multiply charged ions to transfer into the gas phase which greatly increases the detectable mass range by folding of the *m/z* values[6,28,29].

Once the sample is dissolved into a solvent the sample solution is filled via hypodermic needle into a syringe and injected into the electrospray region, with use of a syringe pumped injection process, where the extraction of ions into the gas phase takes place[6], Fig.2.2.

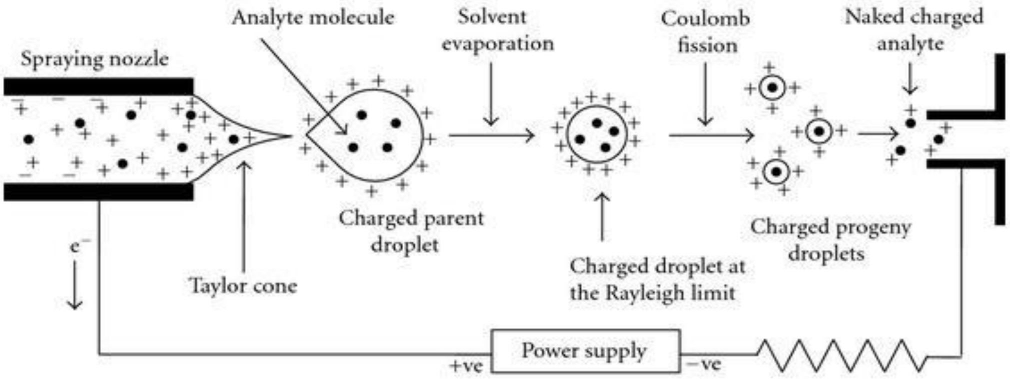

Figure 2.2: Schematic diagram showing process of ESI from capillary tip to gas phase in positive mode. Taken from Ref 27. For negative mode the power supply is reversed and the signs on the analytes exchange positive to negative and vice versa.

ESI is capable of the formation of small, charged droplets with an efficiency that is affected by a variety of factors including flow rate, surface tension of solvent and concentration[6]. When these factors are increased the efficiency of the process is reduced requiring an increase of the electric field across the ESI cavity. At optimum conditions the electric field is in place between the spraying nozzle and the electrospray cavity created by a potential difference in the range of 3-4 kV. However, the electric field can only be raised to a certain value before electrical discharges take place. As an alternative to high electric fields a number of different variations on the capillary design exist with both mass spectrometer units in this thesis run with the variation of a sheath gas of nitrogen with adjustable flow rates that nebulizes the solution and assists in aerosol creation.

The electric field that is in effect across the cavity affects the ions as they emerge from the tip of the spraying nozzle which, when the mass spectrometer is set to negative mode, attracts the negative ions to the edge of the droplet while the positive ions gather towards the nozzle itself[6]. This forms the emerging droplet of solution into a Taylor cone at the tip of the nozzle with the surface tension restraining the anions from the attractive force of the electric field. As the strength of the field is increased the anions eventually overcome this and break out of the Taylor cone as a jet of negative ions which evolves from the centre of the cone which then breaks down into a fine spray. The effect of the positive and negative ions travelling in different directions is called the electrophoretic mechanism[31]. Dry nitrogen gas is introduced at the skimmer as a form of heat to aid in desolvation which has adjustable temperature and flow rates[30].

Fig.2.3 shows the mechanism behind solvent evaporation, a process which leads to droplets with an ever decreasing volume yet contain a constant quantity of charge and thus an ever increasing charge density. These droplets eventually reach a critical charge density called the Rayleigh limit[32] and destabilise, ejecting a plume of even smaller droplets which after further desolvation and ejection cycles leads to analyte ions from the original sample solution in the gas phase[11].

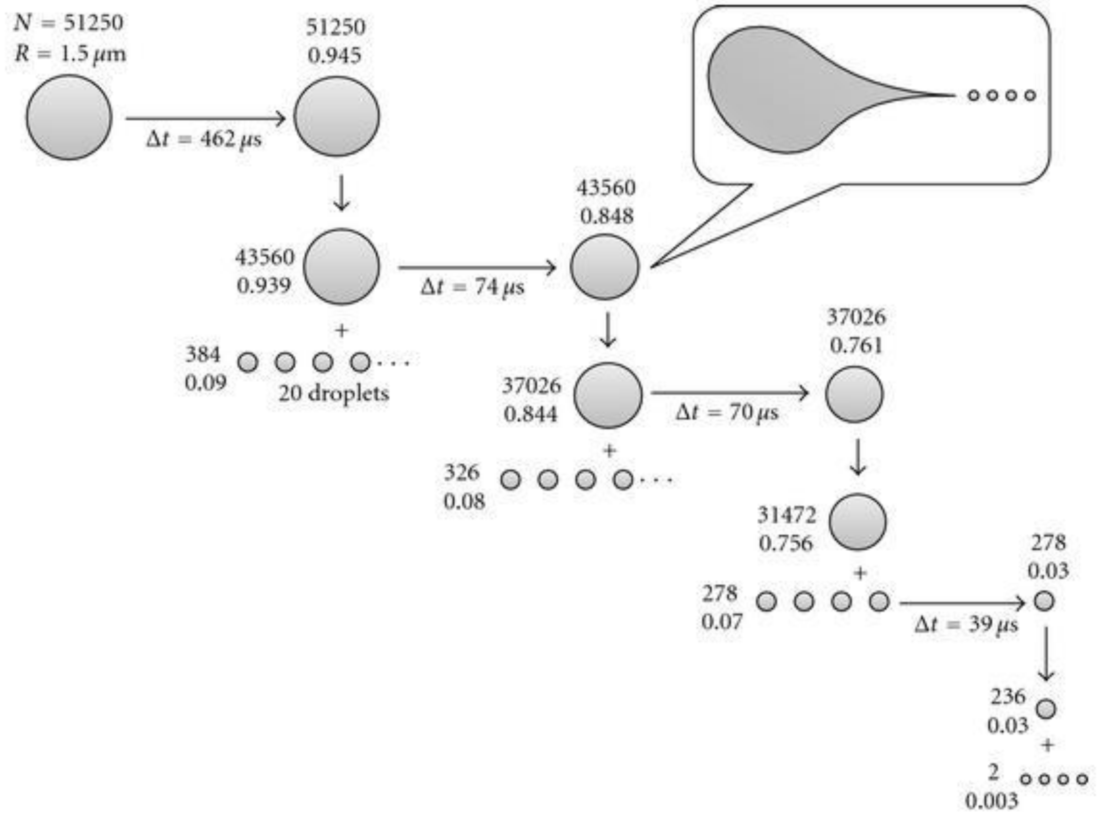

Figure 2.3: Diagram displaying one proposed mechanism for the breakdown of droplets formed from the ejection of the Taylor cone with typical radius and charge quantity of droplets labelled. Insert displays shape of droplet during ejection in the process of tearing off of smaller droplets. Taken from Ref 27.

A skimmer then separates the ions from any remaining solvent or neutral molecules from the entering gas stream allowing only charged molecules to actually enter the mass spectrometer. The sprayer/skimmer for both mass spectrometers in this thesis is orthogonal in design; the two are offset so only ions that are electrostatically attracted toward it enter the skimmer aiding the separation of ions from solvent spray.

2.1.3 The Quadrupole Ion Trap

The quadrupole ion trap uses electric fields to contain charged particles in a 3-dimensional space. This allows for the isolation, temporary trapping and subsequent activation of ions via CID before releasing them towards the detector. The isolation of a particular *m/z* range in the ion trap is carried out by a process called resonance ejection[11,33]. As the ions are suspended in the ion trap they each resonate with a particular frequency related to their *m/z*. By altering the strength of the electric fields in the ion trap ions the highest and lowest *m/z* value ions can be forced to destabilize and lost from isolation. By performing this process for both high and low fields, also called forward and reverse scanning, a range of *m/z* ions can be isolated[11].

The ion traps used in the mass spectrometer instruments in this thesis utilise the 3-D ion trap design consisting of two hyperbolic electrodes combined with a hyperbolic ring electrode, Fig.2.4. The ions isolated in the ion trap are not kept stationary and instead have a continuous motion that is kept stable via the combined effects of the applied electric fields and the helium dampening gas[34].

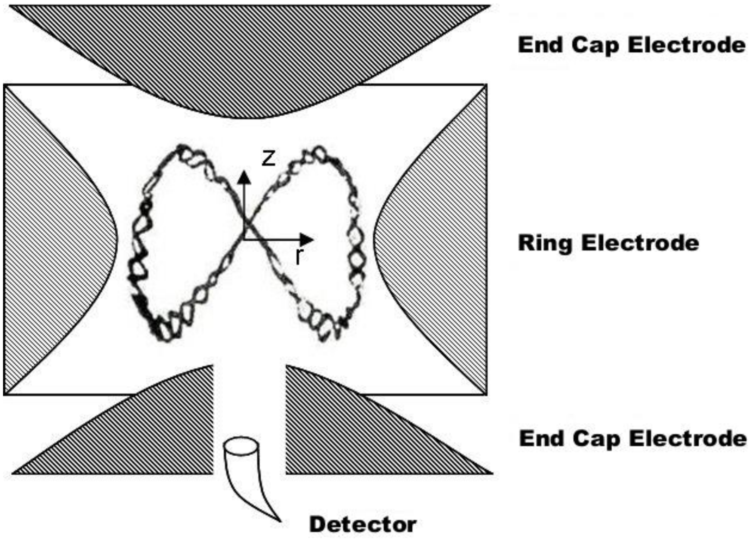

Figure 2.4: Diagram of a 3D quadrupole ion trap highlighting the three hyperbolic electrodes and the stable orbit of isolated ions formed by the effects of the electric fields with exit to detector marked on diagram. Taken from Ref 35.

The ion traps in this thesis have been modified to allow laser beams to enter the ion trap. In the AmaZon this modification was done by the manufacturer. External modifications were done with the addition of two windows, for beam entry and exit, installed into the shell of the mass spectrometer unit while the ion trap ring electrode had a small hole drilled through on both sides. As the design of the ion trap had been altered examinations of the efficiency of the quadrupole were carried out by the supplier. The ion trap was re-tuned to correct the alterations effects on the efficiency of the ion trap. The seal produced by the windows which was necessary in keeping the vacuum for the ion trap was monitored by an array of pressure sensors through the mass spectrometer which allows the user up-to-date knowledge regarding the pressure throughout the unit.

2.1.4 Collision Induced Dissociation

Collision induced dissociation in a quadrupole ion trap, CID, is the process of using an electric field to induce multiple inelastic collisions of a target ion with small buffer gas molecules. In the mass spectrometer units used in this thesis the buffer gas is helium. The aim is to activate the target ion by transforming a small amount of the ions kinetic energy into internal energy after collision. The higher the electric field is set the faster the collision and the more energy imparted onto the target ion. After multiple collisions it is possible to impart enough energy to break bonds and fragment the target ion[34].

Equation 2.1, taken from Ref 12, shows the maximum possible fraction of energy that can be converted into internal energy, E_{Com}, which is related to the mass of the ion, M_i, the mass of the target gas, M_t, which in this thesis is helium and the ion kinetic energy from the laboratory frame of reference, E_{Lab}. For the low energy collisions in this thesis the E_{Com} is approximately at its maximum and thus equal to the actual amount transferred[12]. The trap control software is able to control the strength of the applied electric field in steps of 0.01 V which changes the E_{Lab} by small, discrete increments allowing for specific control over the energy transferred.

$$E_{Com} = E_{Lab}\frac{M_t}{M_i+M_t} \qquad 2.1$$

Finally the remaining ions are scanned out of the ion trap and a fragmentation mass spectrum is generated.

2.2.1 Diode Laser

A diode laser is an electrically pumped pn-junction diode capable of generating a continuous fixed wavelength beam[19,36,37,38,69]. The pn-junction diode is the active material in the diode laser which consists of a combination of both a p-type and an n-type material joined on opposing sides of a thin, high resistance material called a junction. The n-type material is doped by substituting a group 5 element, chosen by having an occupied energy band only slightly lower in energy than the conduction band which allows for easy thermal excitation, into the silicon lattice which supplies an extra electron into the structure. The p-type is doped with a group 3 element, chosen by having an unoccupied energy band just above the valence band allowing for availability for electron recombination, into the silicon lattice which removes a potential electron from the structure leaving a vacant space, hole. As the junction is made from semiconductor material the diode laser falls into the category of a semiconductor laser[19,26,36,37,38].

The active medium is pumped via electric current which when applied in such a way so that the n-type section is supplied with electrons, forward bias, then electrons transverse from the n-type to the p-type[36,37]. As an electron travels from one section to the other it finds itself in an increasing population inversion as the concentration of local excited electrons decreases while available vacant holes increases which will inevitably lead to recombination via photon emission. The recombination process can occur independently of outside influence in a process called spontaneous emission but to create a laser beam with sufficient power the process of stimulated emission is required where the emitted photons of the desired wavelength are trapped inside the active medium to form an active cavity via the use of mirrors, called an optical cavity. These photons are capable of instigating the recombination of electrons they pass which can emit a photon of identical wavelength. This process is repeated multiple times amplifying the photons with a portion of all photons released from the cavity forming the laser beam[19,36,37].

The diode laser used in this thesis is a 375 nm, 3.31 eV, continuous wavelength diode laser. It was purchased from Photonic Solutions and produces an average power of 40 mW. At this wavelength it is the bluest commercially available diode laser. The use of the diode laser is a simple procedure which involves using the control box to set the required voltage for the diode laser, 1.10 V, to produce a laser beam at the operational power which was checked with the use of an external power meter. The beam was directed using the optics setup described in Section 2.4.1.

2.3.1 Nd:YAG OPO

The Nd:YAG OPO laser is comprised of two separate components, the neodymium-doped yttrium aluminium garnet, Nd:YAG, and the optical parametric oscillator, OPO, which combine to provide a pulsed, variable wavelength laser beam. The Nd:YAG is a solid state laser as the active medium is a solid crystal of yttrium aluminium garnet that is doped with neodymium in its trivalent state, Nd^{3+}. The laser is pumped by the use of a flash lamp which emits an intense series of flashes with a wide variety of wavelengths although the majority is in the visible spectrum making the Nd:YAG an optically pumped laser[19,26,69].

The beam of photons is created by the radiative transition of an electron from one excited state down to a lower excited state, the energy gap between these two levels equals the desired wavelength of the emitted photon, Fig.2.5. To create the necessary population inversion and thus avoid the energy levels of the crystal becoming saturated the flashlamp pumps electrons from an energy level below the energy levels used in the creation of the photon up into energy levels above the energy levels used for photon creation[19,26]. The YAG lasers used in this thesis have an energy gap which generates a photon of 1.064 µm.

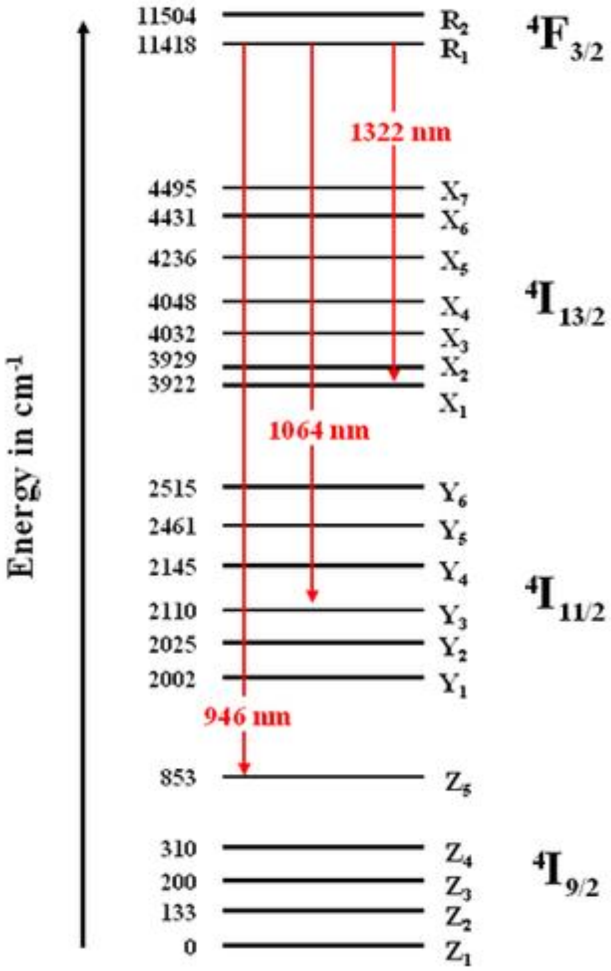

Figure 2.5: Diagram showing energy levels involved in the emission of a laser beam of 946 nm, 1064 nm and 1322 nm. Taken from Ref 39.

The OPO contains no light source of its own and so is pumped by the Nd:YAG laser which for the Nd:YAG in this thesis has been tripled from 1.064 µm to 355nm. Two conservation rules are fundamental for the function of the OPO, the conservation of energy and the conservation of momentum.

The initial beam from the Nd:YAG is split into two different wavelengths which in total conserve the total energy of the original beam. The OPO contains a non-linear crystal which conserves the momentum of the system is part of the optical cavity which amplifies the desired wavelength. By rotating the crystal the wavelength that is amplified changes, this allows the OPO to scan across a range of wavelengths. For the OPO in this thesis a final doubler is used. The entire process greatly reduces the energy of the laser produced from the initial laser.

Two OPO lasers used to acquire the data presented in this thesis with each one accompanying each mass spectrometer. The range of powers used in the OPO lasers is 0-10 mJ in the UV wavelength range with pulses per second of 10 Hz.

2.4.1 Additional Apparatus for Laser Interfaced Mass Spectrometer Experiments

The diode and YAG lasers both used a series of optics to direct the beam into the mass spectrometer ion trap. The optics used quartz prisms for the redirecting of the beam, a lens for focusing the beam with a focal point just before the entrance to the ion trap and adjustable irises to reduce beam power as required.

An electronic shutter was purchased from Thor Labs, model SH05, and was also included which is capable of opening and closing automatically once activated, blocking the laser beam from entering the ion trap. When in use the shutter would be in synchronisation with the filling of the ion trap and would only open for the fragmentation phase of the cycle and closed for the rest of the cycle.

Chapter 3: Investigating Fragmentation of Nuc$\cdot$I$^-$ Clusters with UV Photons Combined with CID Excitation

3.1.1 Introduction

ESI Mass spectrometry is an important method for characterizing the structure of biomolecules via the fragmentation of mass-selected parent ions and analysis of fragmentation patterns[40]. However, the fragmentation of the ions requires many different fragmentation methods to provide the broadest range of structural information. Therefore, considerable current emphasis is placed on developing new fragmentation methods. In this chapter, we explore a new fragmentation method which combines a UV diode laser combined with CID excitation for the first time.

Presently laser fragmentation combined with mass spectrometry uses the OPO and Dye lasers. However, each has various analytical constrictions such as recording time per single data point, a high level of user skill required to operate as well as the fragility of components which leads to a high degree of maintenance. There are also logistical factors to consider such as their large size, high cost of purchase and running as well as a high health and safety risk. A diode laser can be considered an excellent alternative to high powered pulsed lasers as a cheap, user friendly photon source. This chapter will cover the experimental investigation of a UV diode laser combined with CID excitation and whether this dual excitation tool can excite an $Nuc{\cdot}I^-$ complex across the electron detachment threshold, initiating an electron transfer from the I^- to the nucleobase[41,42,43], which can then fragment via dissociation of a temporary nucleobase anion.

The fixed wavelength diode laser used in this thesis generates a continuous wave UV laser beam at 375 nm (3.31 eV). As an independent fragmentation tool this is a limited device capable of being applied only to molecular systems that contain absorption bands capable of fragmentation at energies below 3.31 eV. To effect electron detachment, the photon energy, E_{hv}, must be greater than the VDE of the target, $E_{hv} > \text{VDE}$. When the photon energy equals or exceeds the VDE electron detachment can occur. Alternatively if the photon energy is even slightly lower than the VDE value then no detachment occurs. With most biomolecule anions possessing VDE > 3.3 eV this greatly limits the ability of the diode laser in use with biomolecule analysis[44]. However, this example contains a crucial assumption that the target system was initially in its ground state. If the system was instead excited through the vibrational/rotational energy levels then the total energy of the system plus photon energy could exceed the electron detachment energy. In this chapter CID was investigated as a source of internal ion excitation as a precursor for UV photon absorption.

CID is the process of engaging the target ion with collisions with a neutral buffer gas, converting kinetic energy of the ions into internal energy with the goal of breaking apart the bonds in molecular ions. However, for this project instead of breaking bonds, the goal of the CID excitation is to only transfer enough energy to raise the internal energy of the molecular ion to allow subsequent UV photon absorption to then exceed the detachment energy of the anionic system studied here. In this work, we use CID in a quadrupole ion trap which has one major advantage of allowing small incremental increases in the ion energy via the alteration of the strength of the electric field in the ion trap which controls the ion kinetic energy. The advanced software in the commercial mass spectrometer allows for a great level of accuracy in the ion kinetic energy selected.

The diode laser combined with the CID excitation can therefore be capable of removing an electron through exceeding the electron detachment threshold and subsequently leading to a free electron initiated chemical reactions such as those described in Section 3.4.2. For the first experiments, the source of the electrons was decided to be provided from a halide ion, specifically from iodide while the electron transfer acceptors were the nucleobase biomolecules adenine, A, uracil, U, cytosine, C, and thymine, T, guanine was not studied due to being insoluble in common solvents. The nucleobase-halide complexes shall be referred to hereon as $\mathrm{Nuc{\cdot}X^{-}}$ while the nucleobase-iodide anion complexes shall be referred hereon as $\mathrm{Nuc{\cdot}I^{-}}$ with the corresponding complexes for uracil, thymine, adenine and cytosine complexed to iodide referred to as $\mathrm{U{\cdot}I^{-}}$, $\mathrm{T{\cdot}I^{-}}$, $\mathrm{A{\cdot}I^{-}}$ and $\mathrm{C{\cdot}I^{-}}$ respectively.

Halide ions have relatively low detachment energies and are also known to form stable molecular clusters with polar molecules. Iodide was chosen as the halide for these experiments as it possesses the lowest detachment energy. This trend continues for the respective nucleobase complex with the $\mathrm{Nuc{\cdot}I^{-}}$ complexes having the lowest detachment energy of all the $\mathrm{Nuc{\cdot}X^{-}}$ complexes[31]. This was an important factor as the required precluding CID excitation energy necessary to enable UV photon excitation, E_{CID+UV}, for CID+UV analysis could potentially exceed the energy required for complex dissociation, E_{CID}, breaking bonds apart before the UV photon is capable of excitation.

$$E_{CID+UV} < E_{CID} \tag{3.1a}$$

$$E_{CID+UV} > E_{CID} \tag{3.1b}$$

Equation 3.1a shows the desirable system where the amount of CID energy required for UV excitation to take place is lower than the amount for dissociation whereas Equation 3.1b is the unfavourable scheme where dissociation of the complex will have already occurred before UV excitation could take place. Ana Martı´nez and group[31] have published abinitio calculation of the dissociation energy and VDEs for uracil complexes to different halogens which are as follows. All $U{\cdot}X^-$ complexes are predicted to possess cluster dissociation energy of 1.2 eV with the exception of $U{\cdot}F^-$ which had an energy of 3.7 eV. This distinctive value is due to $U{\cdot}F^-$ adopting a distinctive structure. The VDEs for the remaining three $U{\cdot}X^-$ complexes are $U{\cdot}Cl^-$, 4.7 eV, $U{\cdot}Br^-$, 4.4 eV, and $U{\cdot}I^-$, 4.2 eV. When considering the energy of the UV photon, 3.31 eV, that means that the E_{CID+UV} from Equations 3.1a and 3.1b required for each halogen would be 1.39 eV, 1.09 eV and 0.89 eV for $U{\cdot}Br^-$, $U{\cdot}Cl^-$ and $U{\cdot}I^-$ respectively. $U{\cdot}Cl^-$ and $U{\cdot}I^-$ are the only two complexes that pass the requirement of possessing an E_{CID+UV} below their respective E_{CID} values of 1.2 eV. Although $U{\cdot}Cl^-$ was a possible choice, however, it was decided that $U{\cdot}I^-$, with the largest margin between E_{CID+UV} and E_{CID}, would generate the best results[45].

3.1.2 Nuc·I^{-} Complexes

The main objective of this experimental work was to investigate the capacity of the diode laser when combined with CID excitation as a fragmentation tool for the analysis of biomolecules. Firstly, the actual ability of the UV photon, assisted by CID, to be absorbed needed to be proven possible, and secondly, it was necessary to compare the findings against previously published data of the mechanisms of Nuc·I^{-} complex fragmentation. As such, it was of interest to understand the nature of the intercluster bonding in the Nuc·I^{-} complex.

The bonding in the Nuc·I^{-} complex arises from the attraction of the negative I^{-} and the electropositive hydrogen atom/s of the nucleobase, thus forming strong ionic hydrogen bonds[41,42]. Recent work by Ana Martı´nez and group involved abinitio calculations on non-conventional hydrogen bonding systems, which included the U·I^{-} complex[45]. The results showed that for the particular case of uracil complexed to a halide the bond could be classified as an ‘ionic conventional hydrogen bond’, a conclusion that was based on the complex’s dissociation energy, 1.2 eV, intermolecular bond length, N1-H; 1.0 Å and H1-I; 2.6 Å, and bond angle, N1-H1-I; 145^{o}.

Fig.3.1 shows the bonding in the U·I^{-} complex. It can be clearly seen from Fig.3.1 that the iodide is bonded at the positive end of the uracil molecular dipole, which is in agreement with the hydrogen bonding assignment above. In addition, this structure can be seen in Fig.3.2 to also occur for the T·I^{-} complex with the iodide bonding in a similar way as in U·I^{-}.

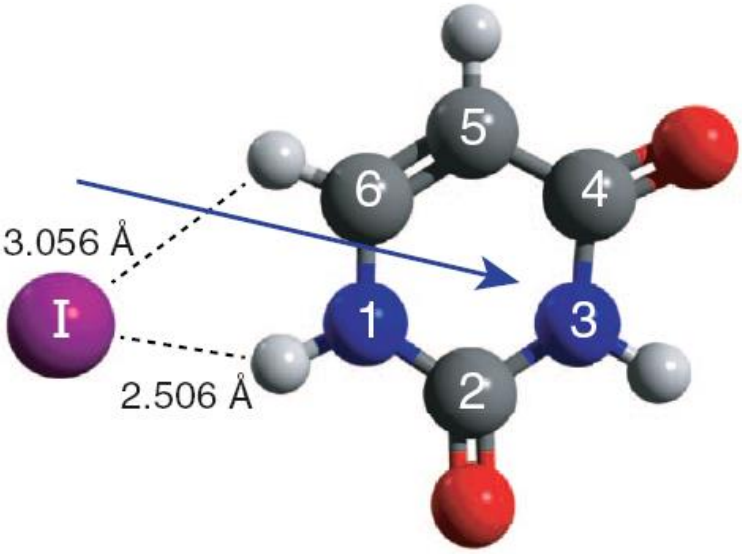

Figure 3.1: Diagram of the abinitio calculated structure of $U{\cdot}I^-$ with the arrow indicator the dipole direction for the nucleobase. Hydrogen bond lengths are marked on the diagram as is the atom numbering scheme with 1,3 representing nitrogen and 2,4,5,6 representing carbon. Taken from Ref 41.

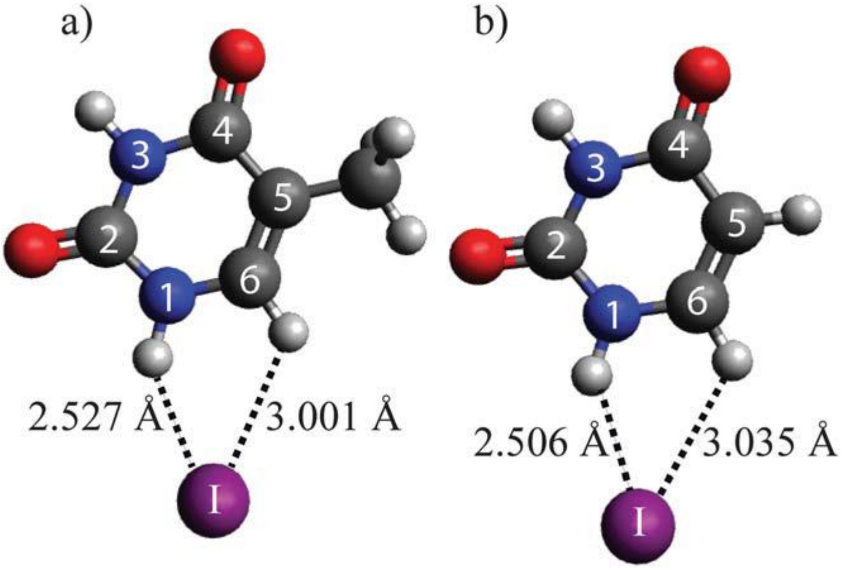

Figure 3.2: Diagram of the abinitio calculated structure of the (a) $T{\cdot}I^-$ and (b) $U{\cdot}I^-$ complexes with bond distances for the hydrogen bond lengths labelled. Also, atom numbering is shown with 1,3 representing nitrogen, and 2,4,5,6 representing carbon. Taken from Ref 42.

3.2.1 Experimental

To analyse whether any interaction between the UV photon and cluster had occurred, all the results were recorded for a range of CID energies both with and without the diode laser entering the ion trap for comparison. Results solely from CID interaction shall henceforth be labelled simply as CID, while results recorded with the combination of CID and UV photons will be labelled CID+UV for the remainder of this thesis. Results were recorded over a range of CID energies where a span from 0.00 V to complete depletion of the parent peak shall be referred to hereon as a “single run” with each data point recorded representing a different CID energy. An automated method was set up using the mass spectrometer software for varying the CID energy. At minute intervals the program would increase the CID voltage by 0.01 V, commencing after the completion of the first reading at 0.00 V for one minute, which would then repeat continuously until the selected range of values was recorded. After ESI injection the cluster is mass selected and isolated in the ion trap with an accuracy of ±0.05 *m/z*.

Each run was repeated until the data obtained was consistent. Any anomalous readings were omitted from the results so as not to incorrectly affect any conclusions. Typical running settings of the AmaZon for the results recorded in this chapter are presented below in Table 3.1.

Table 3.1: Table displaying typical running settings for the AmaZon mass spectrometer used to acquire data in this chapter.

Mass Range:	70-2200 *m/z*	Polarity:	Negative
Scan Speed:	32500 *m/z/sec*	Scan Range:	50-1000 *m/z*
Capillary Voltage:	2700 V	Averages:	1 per data point
End Plate Offset:	-500 V	Smart Frag:	Off
Nebulizer:	10.00 psi	Frag time:	1000 ms
Dry Gas Flow:	6.00 l/min	Frag Delay:	0 s
Dry Temp:	100 ^{o}C	Frag Width:	4 *m/z*
Syringe Flow Rate:	250 µl /h	Isolation Width *m/z*:	1 *m/z*

The automatic ion tuning function of the mass spectrometer was employed to optimize the clusters of the different nucleobases. The ion current control, ICC, is a setting on the mass spectrometer that controls the amount of ions present in the ion trap. The ICC is variable between different $\text{Nuc}{\cdot}\text{I}^-$ complexes with it on for $\text{U}{\cdot}\text{I}^-$ and off for the other three complexes. $\text{U}{\cdot}\text{I}^-$ had a target of ions of 1000000 and a max accrue time of 300 ms. $\text{T}{\cdot}\text{I}^-$ and $\text{C}{\cdot}\text{I}^-$ had a set accrue time of 1000 ms. $\text{A}{\cdot}\text{I}^-$ had a set accrue time of 50 ms. These variations in settings adjusted the parent peak intensity to be closer to the optimum amount for the QIT. Once the complex was isolated the trap settings were then altered to deliver the optimum complex intensities for each system independently by adjusting ion trap values until the intensity of the parent peak was judged to be a maximum compared to the background noise, but without loss of resolution of the peak.

After initial alignment of the diode laser the beam was then blocked from entering the mass spectrometer, and the I^- peak was isolated in the ion trap with its intensity noted. Then the UV beam was unblocked and the amount of depletion of parent I^- ion was observed. If full depletion occurred then the beam path was deemed sufficient, if partial/no depletion was observed then the optics were adjusted, translating the laser beam on an x/y axis parallel to the entry to the ion trap until a reading of sufficient depletion was noted.

All chemicals were purchased from Sigma Aldrich, with tetrabutylammonium iodide used as the source of iodide ions. Nucleobases and tetrabutylammonium iodide were diluted in a methanol solvent to a concentration of approximately 10^{-4} M before being mixed in a 50/50 ratio tetrabutylammonium iodide to nucleobase.

3.3.1 Results

Figs.3.3-3.6 display the negative mode ESI-MS of the $Nuc{\cdot}I^-$ solutions, illustrating formation of the required clusters. The spectra show that there are three significant peaks observed for each nucleobase complex over this mass range. The peak with the highest intensity at 126.8/126.9 *m/z* corresponds to the iodide ion. The other two peaks correspond to the deprotonated nucleobase anion, $[Nuc\text{-}H]^-$, and $Nuc{\cdot}I^-$ clusters.

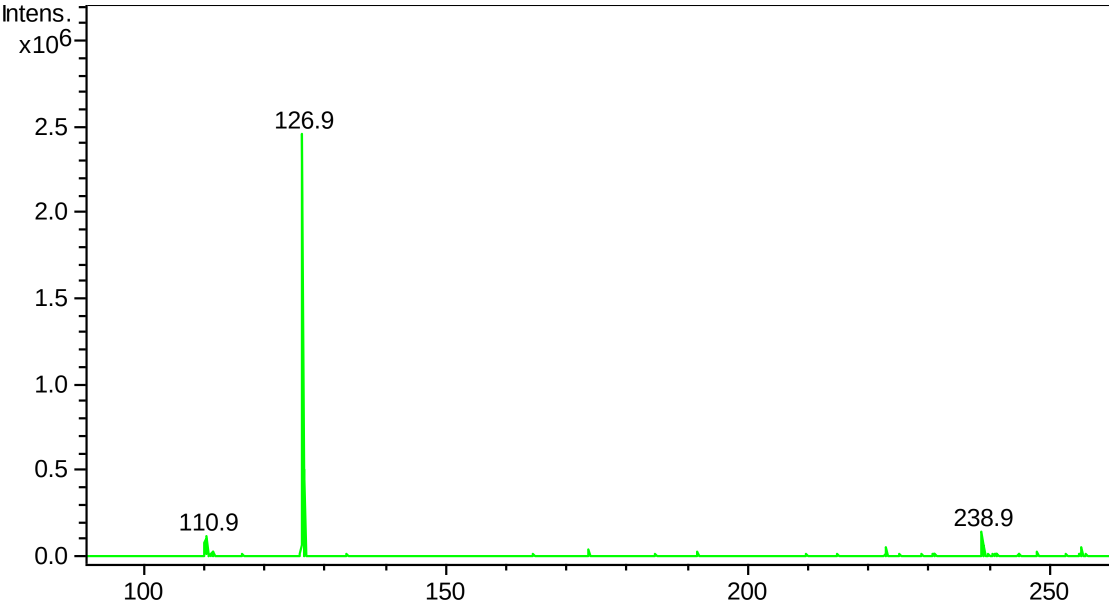

Figure 3.3: Negative ion mode ESI-MS of the $U{\cdot}I^-$ *complex. Peaks; 110.9 m/z, 126.9 m/z, 238.9 m/z represent* $[U\text{-}H]^-$, I^- *and* $U{\cdot}I^-$ *respectively.*

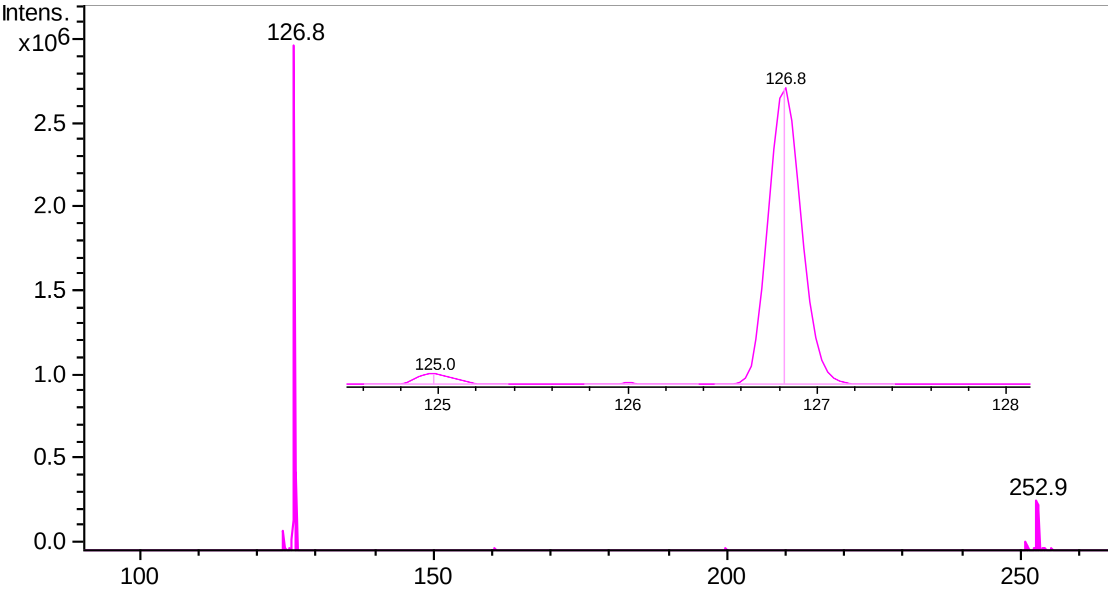

Figure 3.4: Negative ion mode ESI-MS of the $T{\cdot}I^-$ *complex. Peaks; 125.0 m/z, 126.8 m/z, 252.9 m/z represent* $[T\text{-}H]^-$, I^- *and* $T{\cdot}I^-$ *respectively. Zoomed section represented by insert highlights peak m/z.*

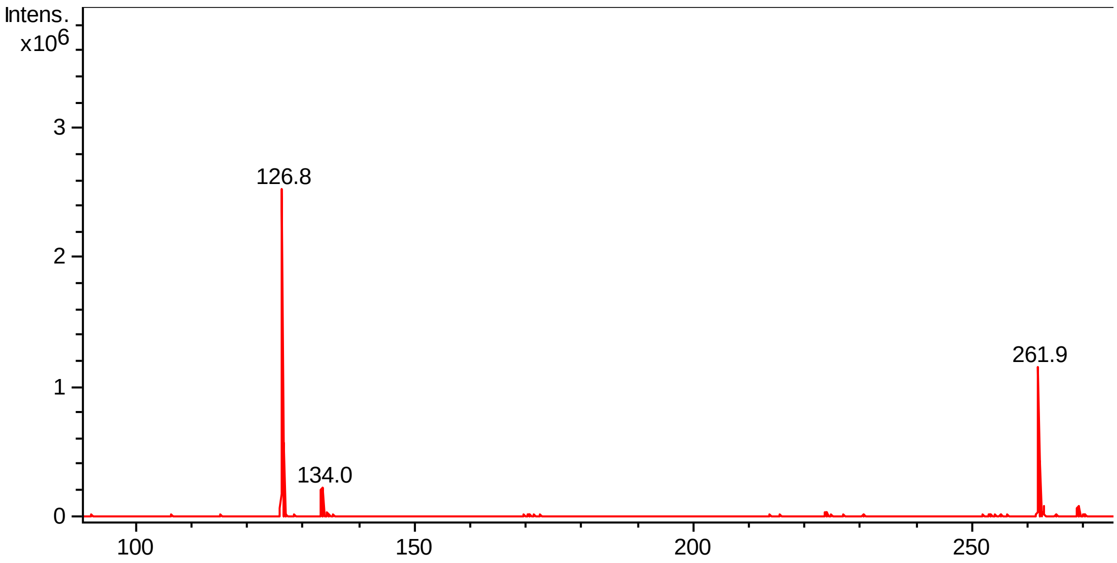

Figure 3.5: Negative ion mode ESI-MS of the $A{\cdot}I^-$ *complex. Peaks; 126.8 m/z, 134.0 m/z, 261.9 m/z represent* I^-, $[A\text{-}H]^-$ *and* $A{\cdot}I^-$ *respectively.*

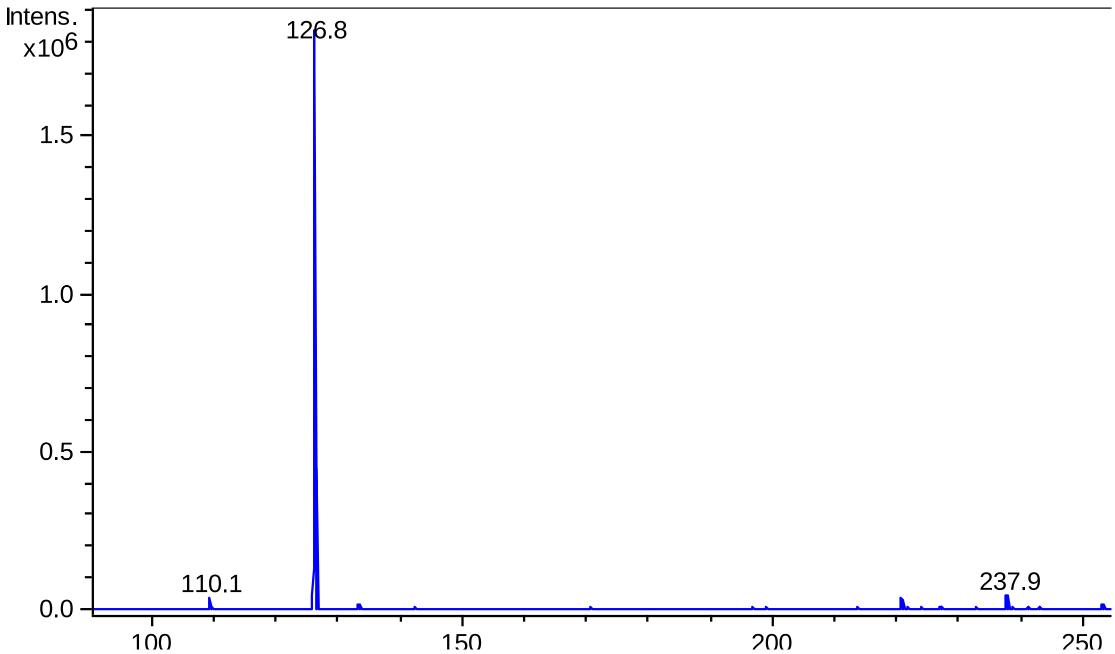

Figure 3.6: Negative ion mode ESI-MS of the $C{\cdot}I^-$ *complex. Peaks; 110.1 m/z, 126.8 m/z, 237.9 m/z represent* $[C\text{-}H]^-$, I^- *and* $C{\cdot}I^-$ *respectively.*

The isolation and induced fragmentation of the Nuc·I⁻ complexes in the ion trap allowed for the intensity of the complex peak to be recorded at different CID energies. This enabled the tracking of both the depletion of the parent peak and the production of any fragments throughout the process. The analysis of the data generated from the experiments for CID excitation saw a depletion in the parent peak for all Nuc·I⁻ with a single fragment peak for I⁻, Fig.3.7 to 3.10. Analysis of the CID+UV results were, however, less informative with no fragments detectable in the mass spectra and have thus not been included.

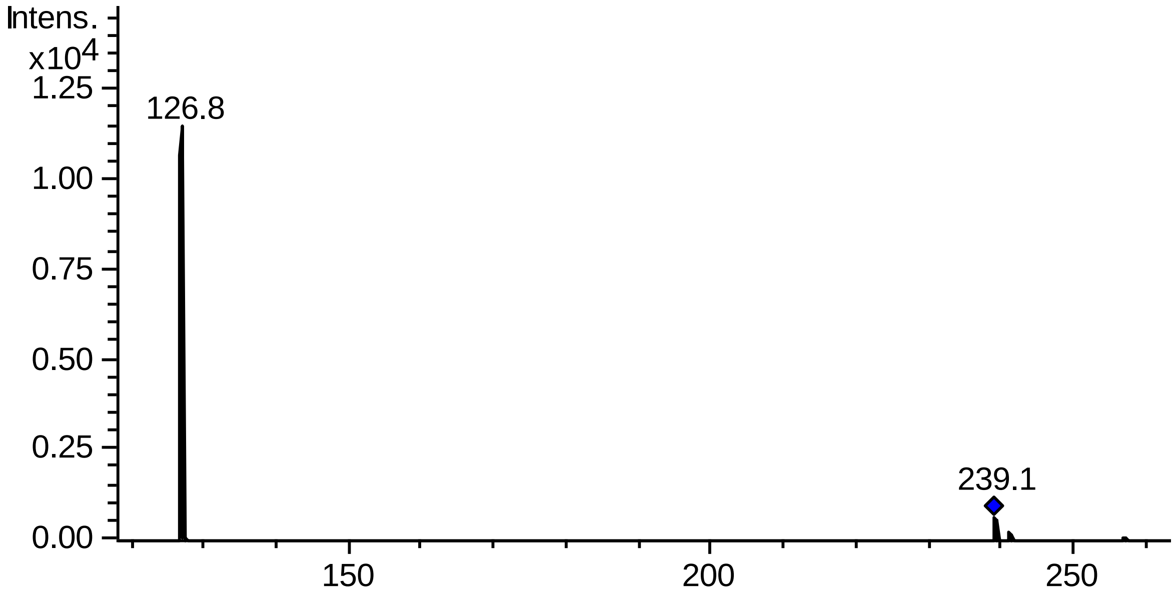

Figure 3.7: Mass spectrum of U·I⁻ complex, CID excitation energy 0.34 V. Peaks at 126.8 m/z, 239.1 m/z represent I⁻ and U·I⁻ respectively.

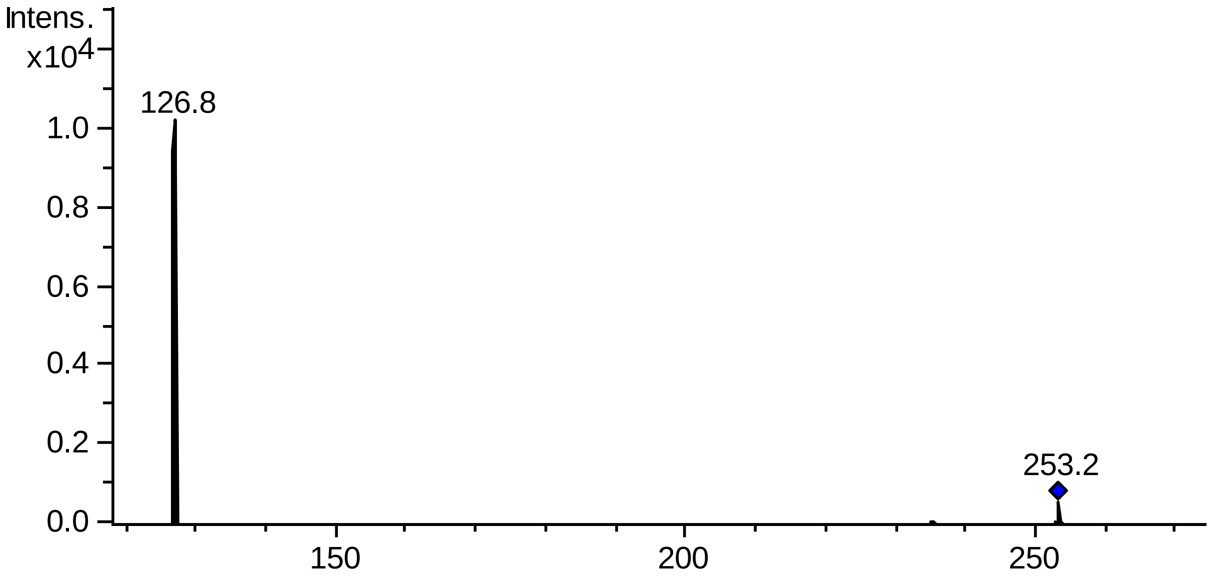

Figure 3.8: Mass spectrum of $T{\cdot}I^{-}$ *complex, CID excitation energy 0.34 V. Peaks at 126.8 m/z, 253.2 m/z represent* I^{-} *and* $T{\cdot}I^{-}$ *respectively.*

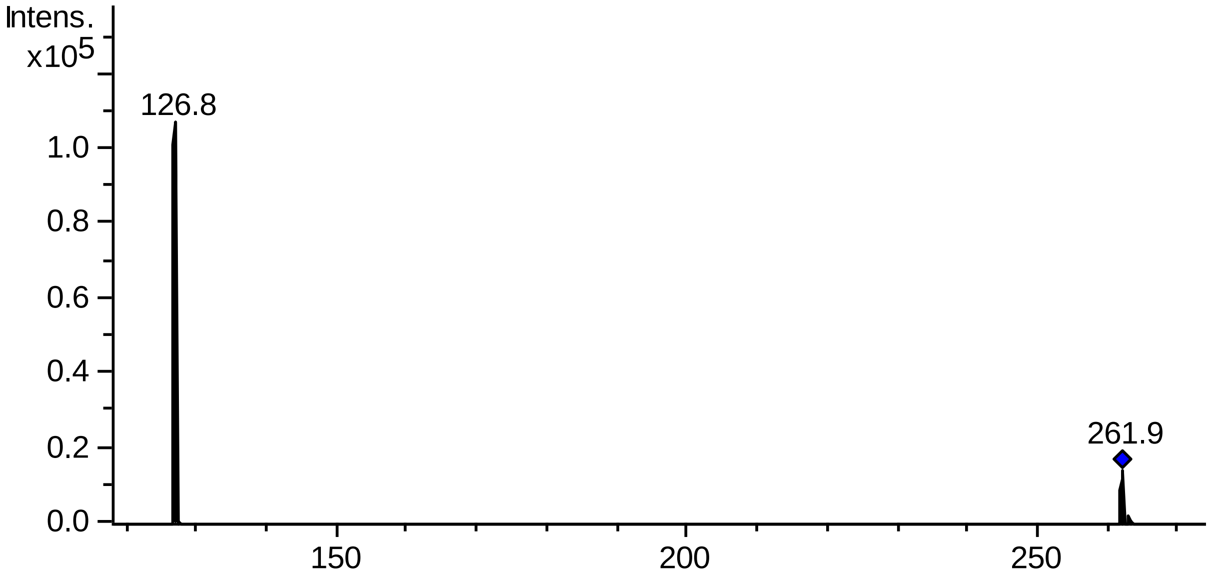

Figure 3.9: Mass spectrum of $A{\cdot}I^{-}$ *complex, CID excitation energy 0.34 V. Peaks at 126.8 m/z, 261.9 m/z represent* I^{-} *and* $A{\cdot}I^{-}$ *respectively.*

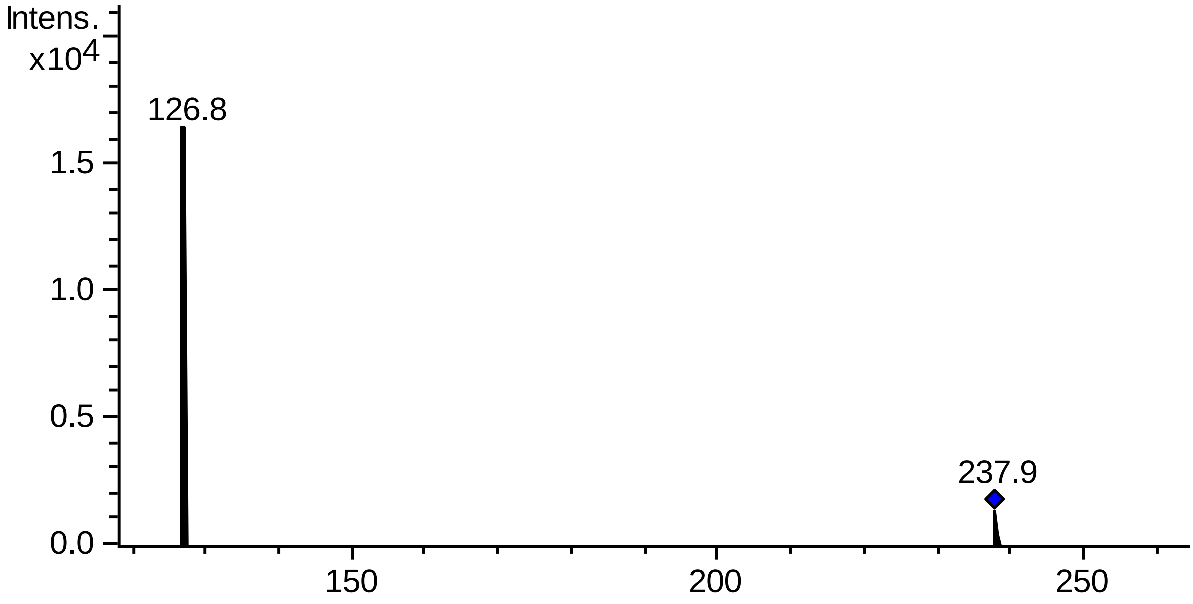

Figure 3.10: Mass spectrum of $C\cdot I^-$ *complex, CID excitation energy 0.34 V. Peaks at 126.8 m/z, 237.9 m/z represent* I^- *and* $C\cdot I^-$ *respectively.*

By normalizing the data for the CID results it was possible to plot the parent peak intensities, I_P, and fragment peak intensities, I_F. The data was normalized using Equations 3.2.a and 3.2.b with the results for the parent peak normalized, P_N, and fragment peak normalized, F_N, plotted as Fig.3.11 to 3.14. The half energy, E_h, where the intensity of the parent peak drops to half its initial value after normalization, can be read from the normalized data.

$$I_P / (I_P + I_F) * 100 = P_N \qquad 3.2.a$$

$$I_F / (I_P + I_F) * 100 = F_N \qquad 3.2.b$$

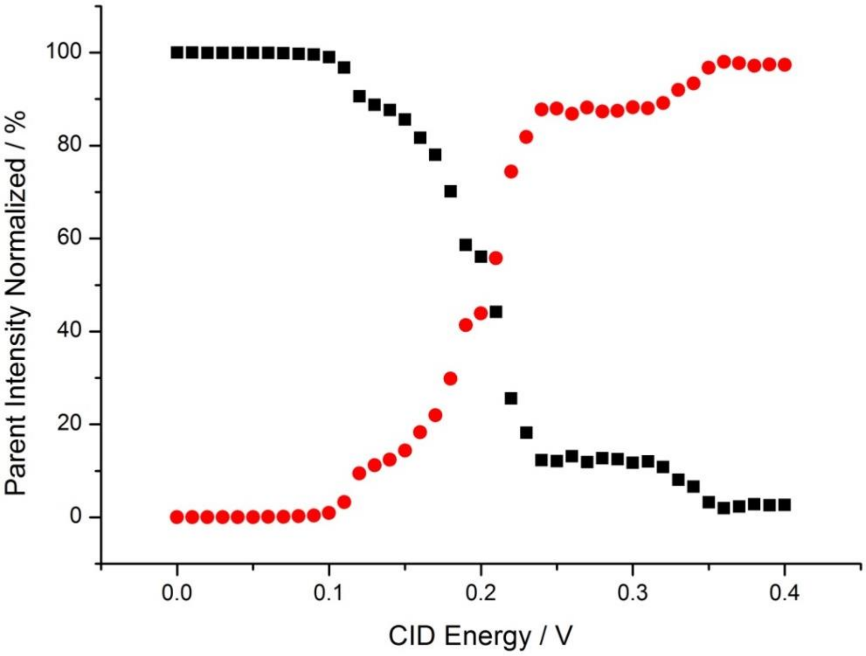

Figure 3.11: % fragmentation curves for $U^{\cdot}I^{-}$. Square symbols represent intensity of parent complex $U^{\cdot}I^{-}$ while circle symbols represent intensity of fragment I^{-}.The E_h is 0.20-0.21 V. An average variation of less than 5% recorded between repeats.

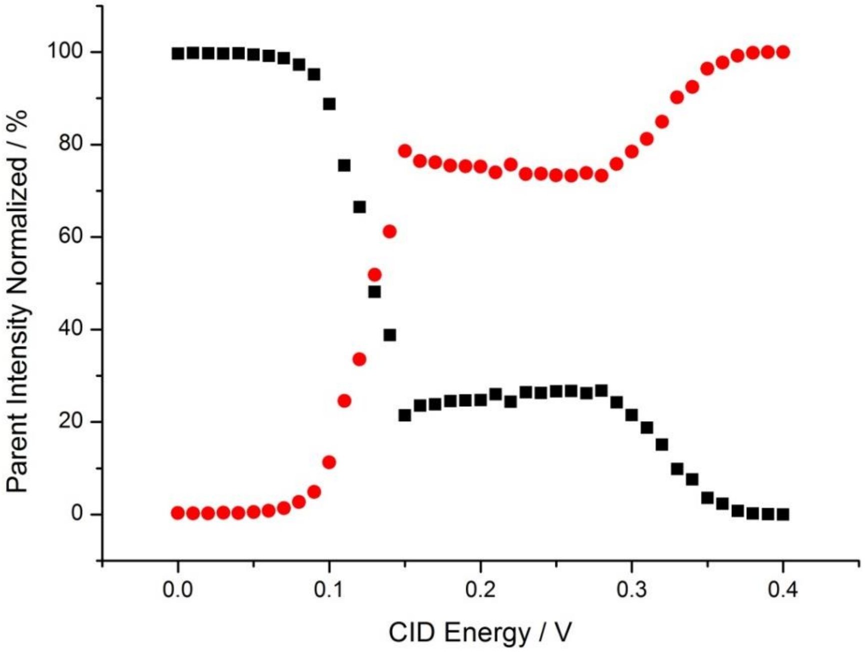

Figure 3.12: % fragmentation curves for $T^{\cdot}I^{-}$. Square symbols represent intensity of parent complex $T^{\cdot}I^{-}$ while circle symbols represent intensity of fragment I^{-}. The E_h is 0.12-0.13 V. An average variation of less than 10% recorded between repeats.

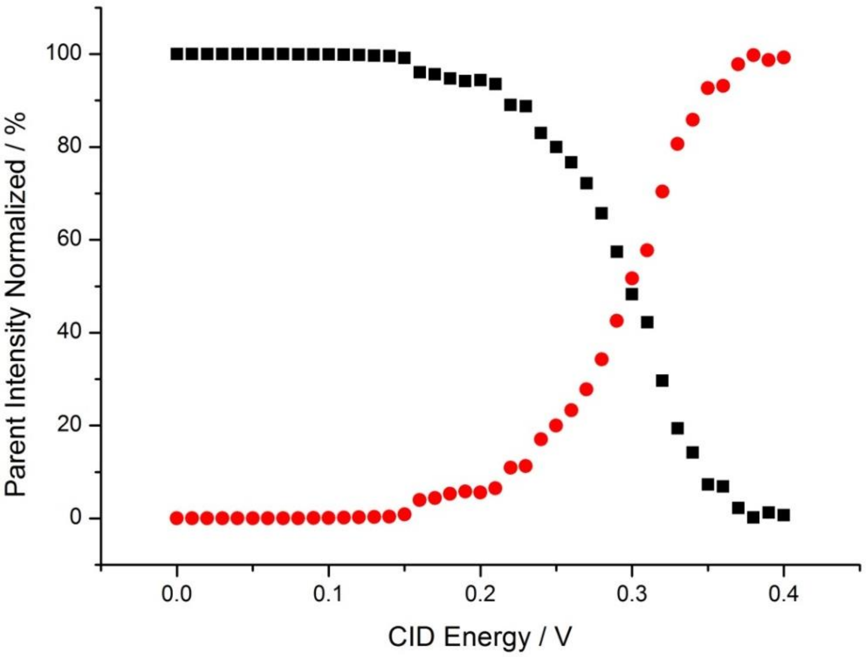

Figure 3.13: % fragmentation curves for $A{\cdot}I^{-}$. Square symbols represent intensity of parent complex $A{\cdot}I^{-}$ while circle symbols represent intensity of fragment I^{-}. The E_h is 0.29-0.30 V. An average variation of less than 8% recorded between repeats.

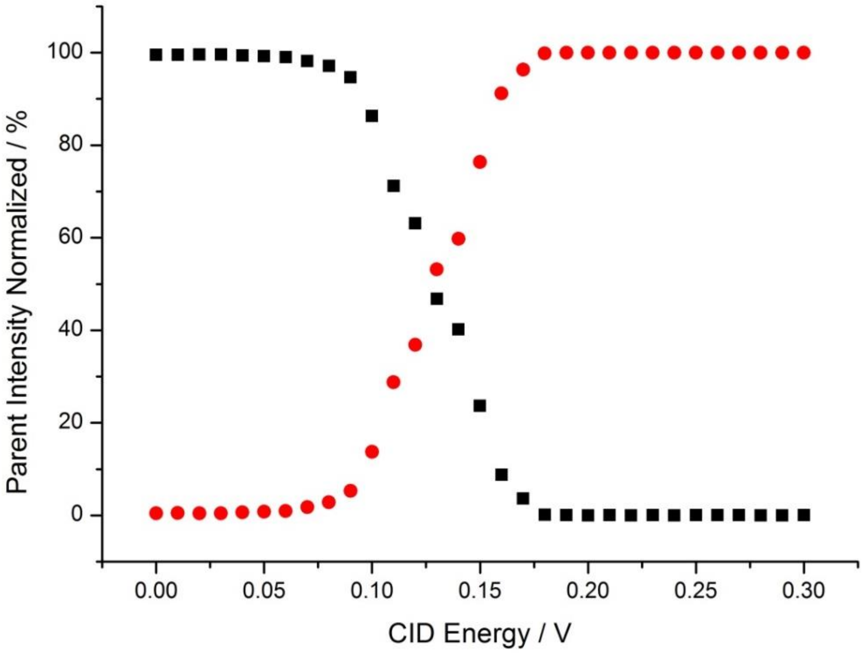

Figure 3.14: % fragmentation curves for $C{\cdot}I^{-}$. Square symbols represent intensity of parent complex $C{\cdot}I^{-}$ while circle symbols represent intensity of fragment I^{-}. The E_h is 0.12-0.13 V. An average variation of less than 9% recorded between repeats.

3.3.2 $U{\cdot}I^{-}$ Cluster

The parent peak intensity for the $U{\cdot}I^{-}$ complex is displayed in Fig.3.15 for both the CID and CID+UV results with a zoomed section plotted as Fig.3.16. There is a significant difference for the $U{\cdot}I^{-}$ cluster intensity between the CID and the CID+UV parent intensities for excitation energies between 0.13-0.24 V and 0.28-0.38 V which, for the remainder of this chapter, are referred to as S2 and S4 respectively, while the regions 0.00-0.12 V and 0.25-0.28 V are referred to as S1 and S3, respectively. The data displayed in Fig.3.15 shows that the parent peak intensity for both CID and CID+UV remains at a constant value through region S1 followed by a significant separation of parent ion depletion over the S2 region. The parent ion intensity falls to 5% of the initial parent intensity for both sets of conditions over S3.

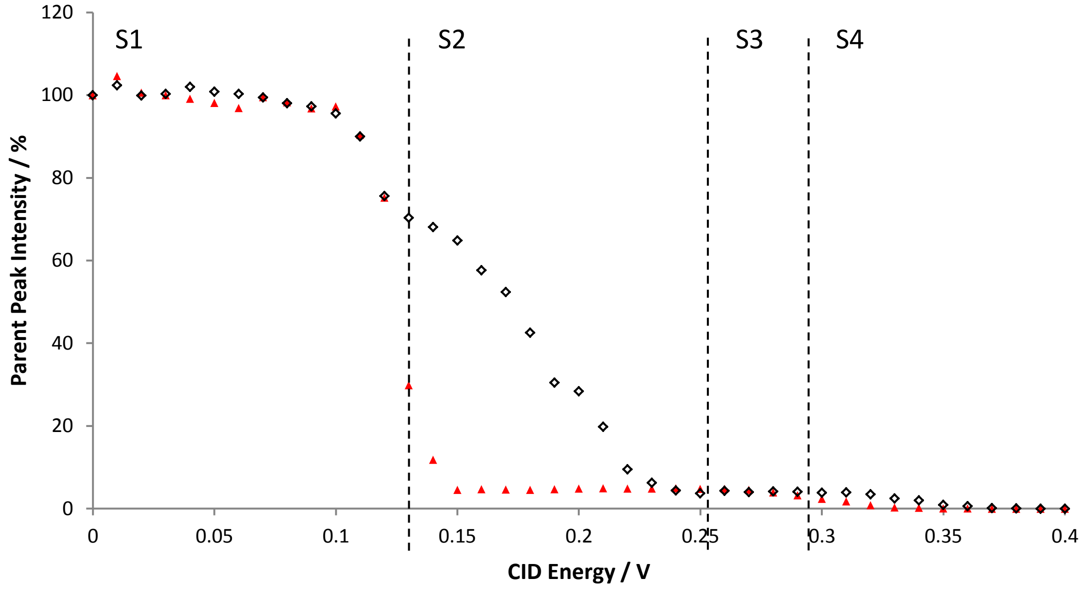

Figure 3.15: % decay curves for $U^{\cdot}I^{-}$. Open symbols represent CID data and closed symbols represent CID+UV data. The three lines on the graph split the data into the four different sections with S1 ranging from 0.00-0.12 V, S2 from 0.13-0.24 V, S3 from 0.25-0.28 V and S4 which ranges from 0.29-0.40 V. An average variation for CID+UV of less than 8% recorded between repeats.

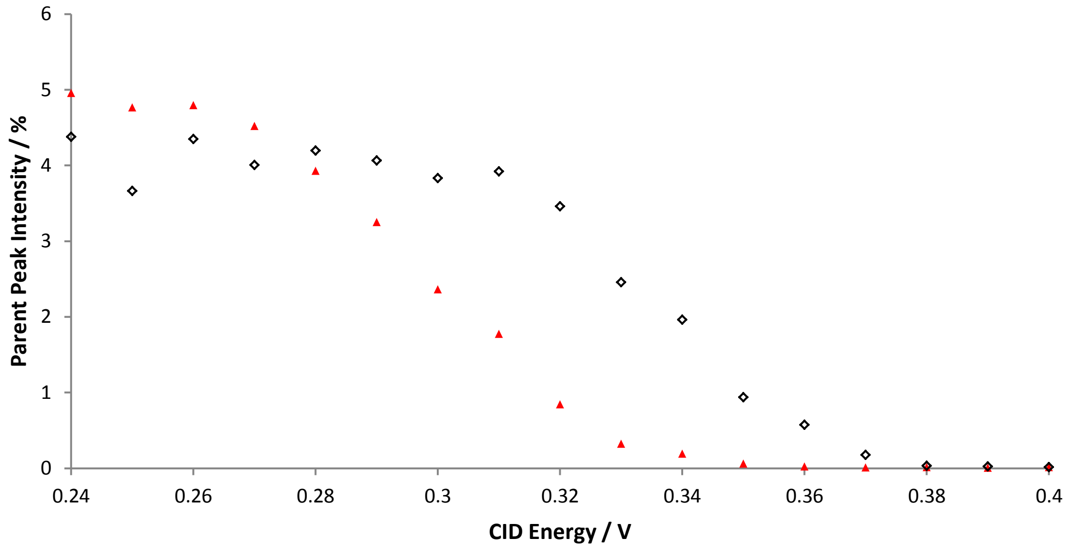

Figure 3.16: Expanded view of regions S3 and S4 from Fig.3.15 highlighting difference in parent intensity between the CID and CID+UV curves.

By replotting the CID excitation data, Fig.3.15, as a difference in intensity between one data point and its previous data point shows distinctive peaks which represent the maximum change in intensity for a respective increase of 0.01 V in electric field strength, Fig.3.17. Three peaks have distinctive maximum points labelled A-C with values of 0.12, 0.19 and 0.22 V respectively and a broader area labelled D with a range across 0.33-0.35 V also detectable.

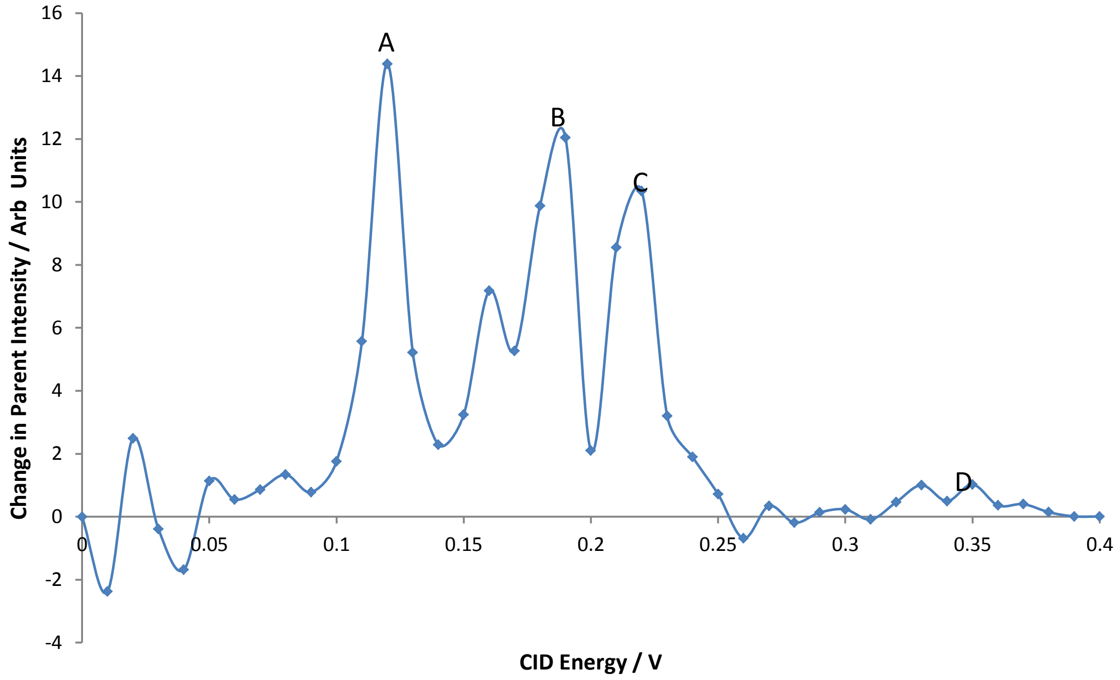

Figure 3.17: The change in parent peak intensity for the $U^{\cdot}I^{-}$ *complex for CID of the selected data point (X) in respect to the previous data point (X-1) using the formula: (X-1) – X = Change in intensity. Peaks labelled A-C are maximum changes in intensity at points 0.12, 0.19 and 0.22 V respectively while peak D is less distinct and resides between the values 0.33-0.35 V.*

The same analysis of the CID+UV data, Fig.3.15, was carried out and replotted in Fig.3.18. The peaks E and F are marked representing maximum changes in intensity for each data point respective of the previous data point. Point E has a value of 0.13 V while point F has a broad curve with a maximum between the values 0.30-0.32 V, extrapolated from the zoomed section in Fig.3.19.

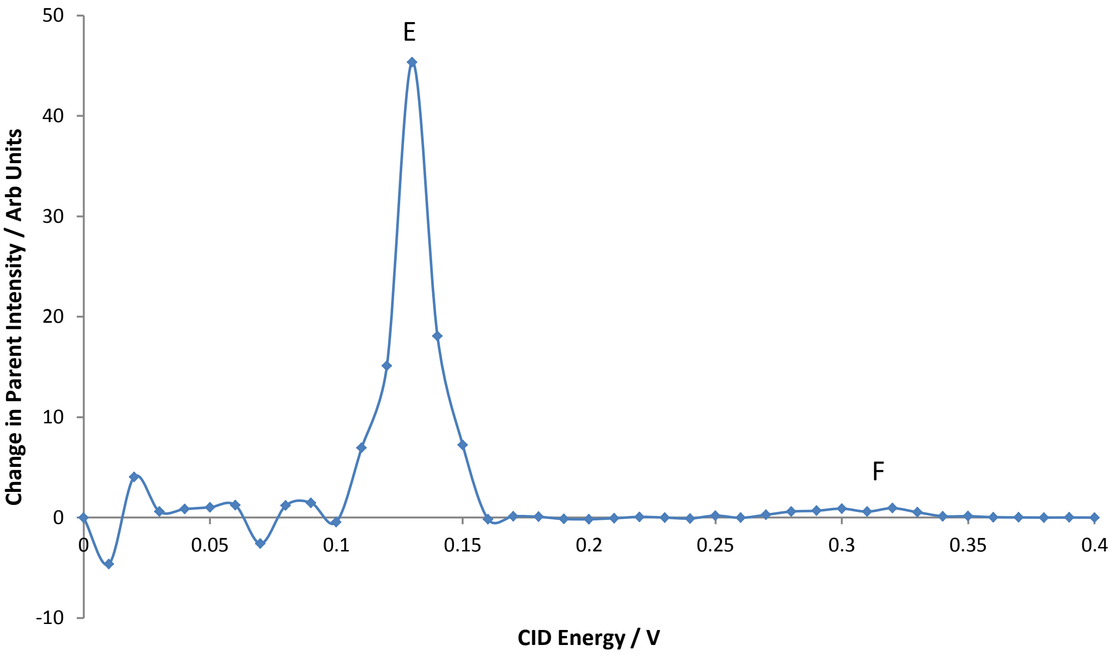

Figure 3.18: The change in parent peak intensity for the $U \cdot I^-$ *complex for CID+UV of the selected data point (X) in respect to the previous data point (X-1) using the formula: (X-1) – X = Change in intensity. Peak labelled E is a maximum change in intensity at point 0.13 V while peak F is less distinct and resides between the values 0.30-0.32 V.*

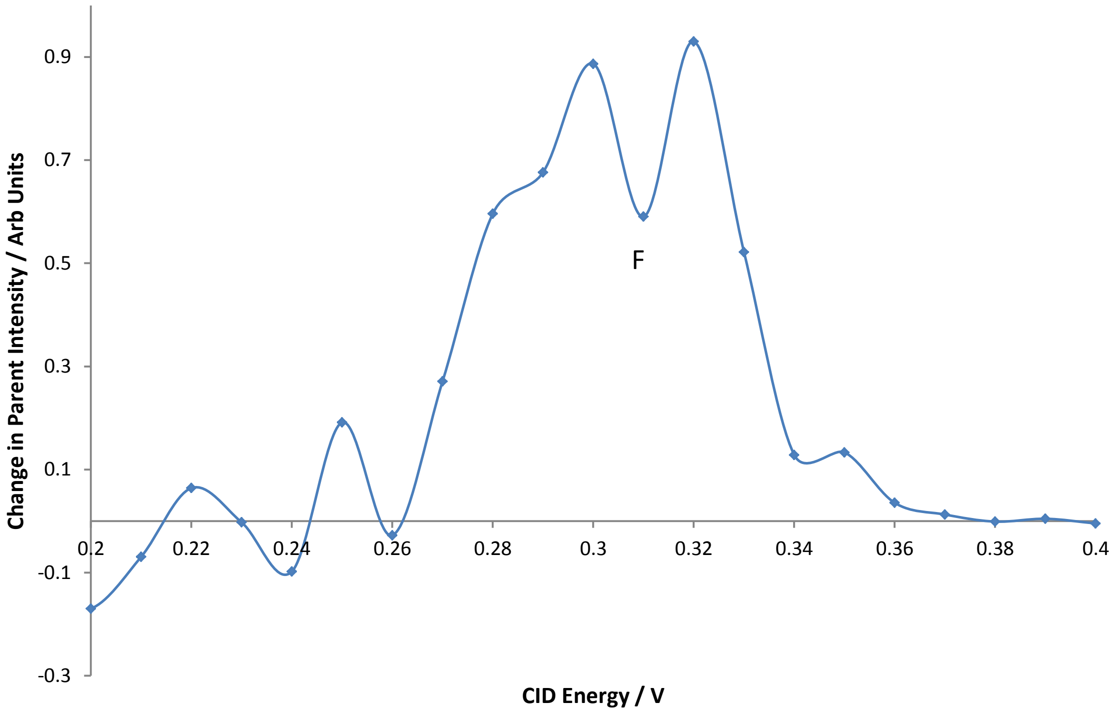

Figure 3.19: Zoomed section from Figure 3.18 highlighting change in parent peak intensity for CID+UV results.

When comparing the results from Fig.3.17 and Fig.3.18 the peaks A and E although appear close in CID energy to each other are almost certainly two independent peaks. This could be verified by referencing back to Fig. 3.15 in which the parent peak depletion of the CID+UV was the same as the parent peak depletion for the CID data for the values up to 0.12 V (peak A) yet CID+UV was vastly higher than CID for 0.13 V (peak E). Another observation regarding the same data is between the peaks D and F which appear in similar CID ranges for CID and CID+UV although peak F is from midpoint to midpoint 0.03 V shifted lower than peak D. This is backed by the results seen in Fig.3.15 where the parent peak depletion for the CID+UV is higher than that of the CID data.

3.3.3 $T\cdot I^{-}$ Cluster

The parent peak intensity for the $T\cdot I^{-}$ complex was plotted as Fig.3.20 for both the CID and CID+UV results. From Fig.3.20 it is unclear whether there is any difference between the CID and CID+UV curves as data values from both sets are all within a small intensity difference of each other. The gradient of the curve for the CID+UV data is greater than for CID between the values 0.12-0.13 V. However, the slight difference that occurs at this range between the two sets of data could be theorised as just being a low initial average for the CID+UV results as raising this value brings the two sets into closer alignment although this alteration has not been plotted or used in this thesis beyond this statement. The $T\cdot I^{-}$ complex results show that a proportion of the initial intensity of between 10-15% is stable over a long range of CID values, drawing parallels to the results from $U\cdot I^{-}$.

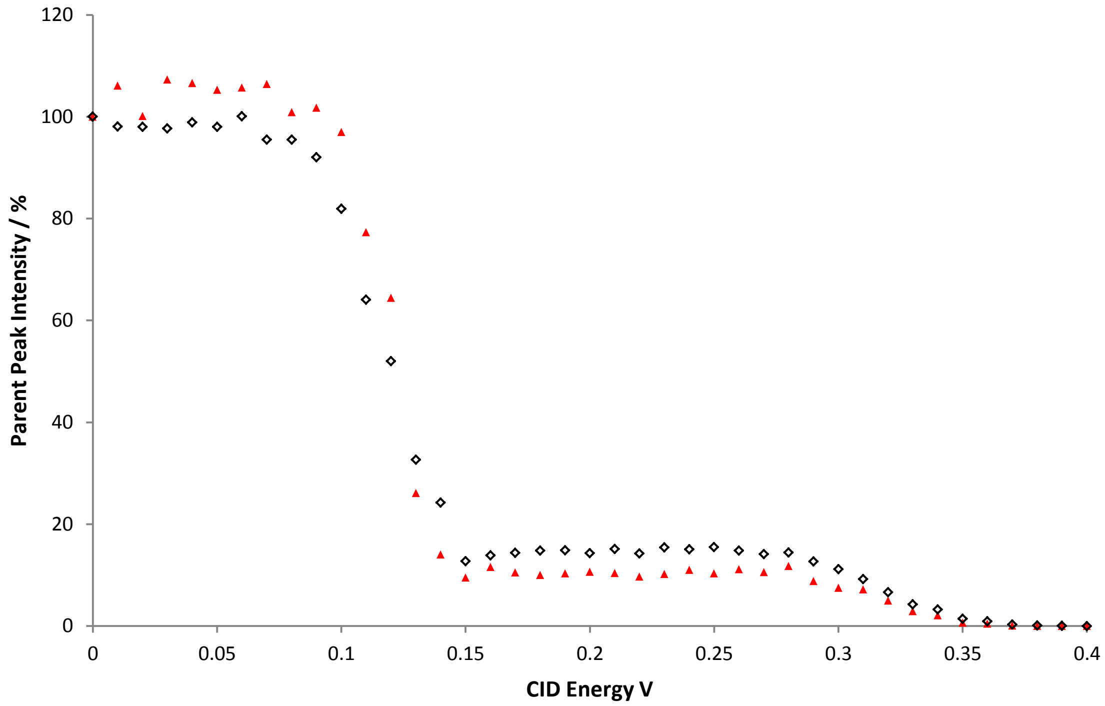

Figure 3.20: % decay curves for $T{\cdot}I^{-}$*. Open symbols represent CID data and closed symbols represent CID+UV data. An average variation for CID+UV of less than 10% recorded between repeats.*

3.3.4 $A{\cdot}I^{-}$ Cluster

The parent peak intensity for the $A{\cdot}I^{-}$ complex was plotted as Fig.3.21 for both the CID and CID+UV results. There is a significant difference between the CID and the CID+UV data points which occurs between values 0.16-0.36 V.

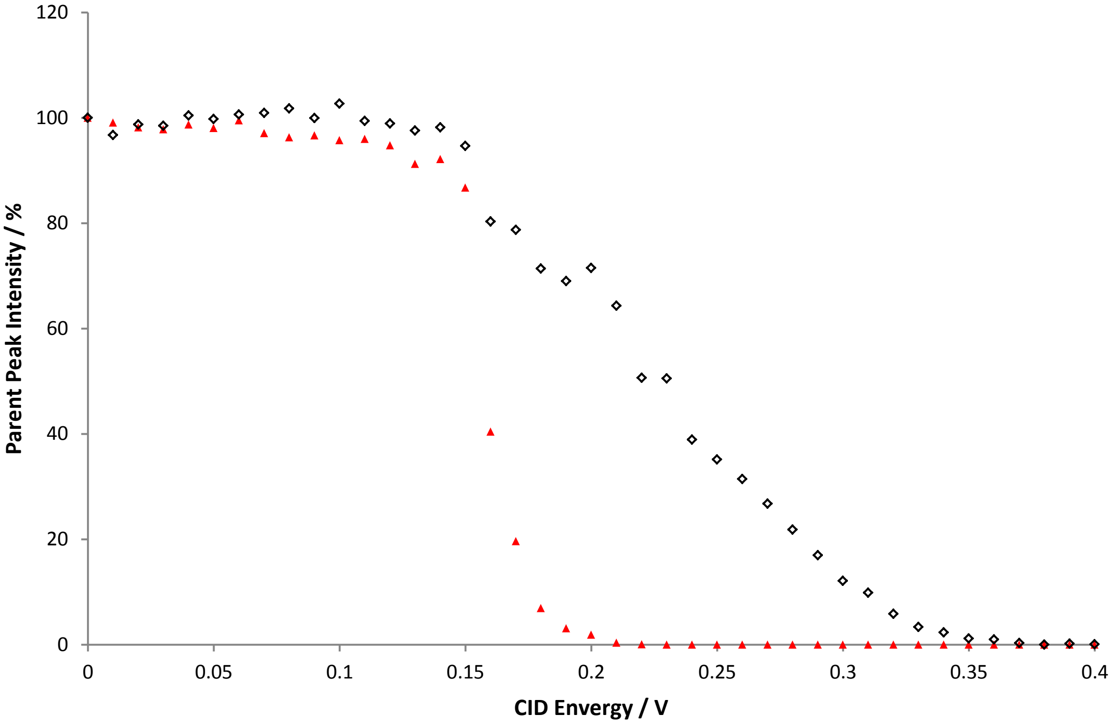

Figure 3.21: % decay curves for $A\cdot I^-$*. Open symbols represent CID data and closed symbols represent CID+UV data. An average variation for CID+UV of less than 9% recorded between repeats.*

The depletion curve for the CID interaction of $A\cdot I^-$ draws a similarity to the $U\cdot I^-$ results as the data shows a similar irregular pattern for the depletion of the complex parent intensity with several areas of no depletion throughout the results. As the same with the $U\cdot I^-$ results, by replotting the $A\cdot I^-$ data, Fig.3.21, as a difference in intensity between one data point and its previous data point, distinctive peaks in depletion can be observed, Fig.3.22. Between the ranges of 0.14-0.25 V almost every alternative data point drops to approximately zero depletion followed by a rapid increase in depletion which repeats creating four distinct drops and four rises in intensity.

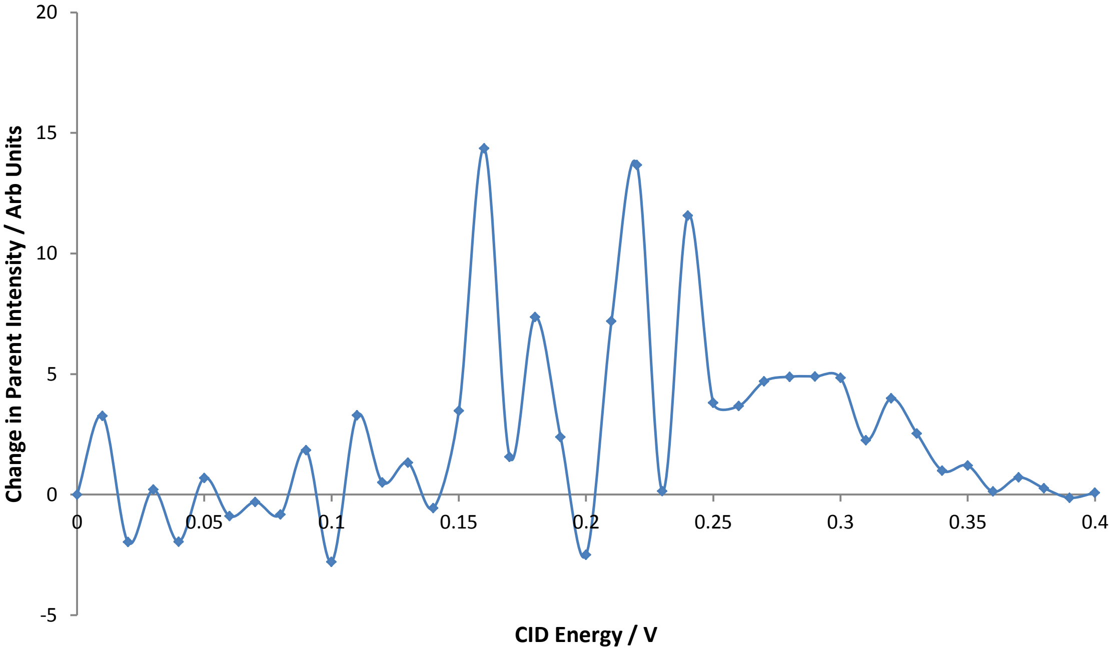

Figure 3.22: The change in parent peak intensity for the $A{\cdot}I^{-}$ *complex for CID of the selected data point (X) in respect to the previous data point (X-1) using the formula: (X-1) – X = Change in intensity. Values between the ranges of 0.14-0.25 show a very inconsistent amount of depletion with almost every alternative value having approximately zero depletion.*

3.3.5 $C{\cdot}I^{-}$ Cluster

The results for $C{\cdot}I^{-}$ are similar to that of $T{\cdot}I^{-}$ as the there is no clear observation from plotted data for UV interaction impacting on the parent peak intensity for the CID+UV results, Fig.3.23. However, after close examination the gradient for the data, once again like $T{\cdot}I^{-}$, for CID+UV is slightly greater than that for CID during the depletion curve although the significance of such a relatively small difference is highly questionable.

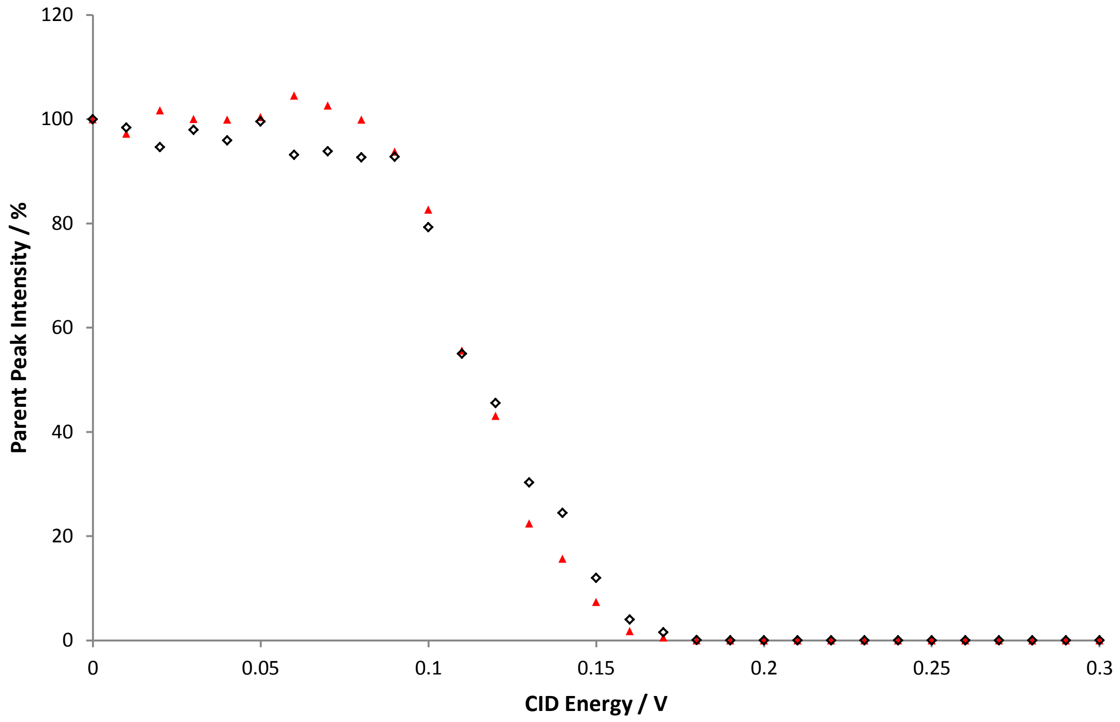

Figure 3.23: % decay curves for C·I⁻. Open symbols represent CID data and closed symbols represent CID+UV data. An average variation for CID+UV of less than 14% recorded between repeats.

3.4.1 Discussion

Comparison of the half energies for all Nuc·I⁻ shows that A·I⁻ has the highest half energy, 0.29-0.30 V, followed by U·I⁻, 0.20-0.21 V, and then C·I⁻ and T·I⁻ are approximately equal to each other with respective values of 0.13-14 V and 0.12-0.13 V. This shows good correlation with the dipole value which for the nucleobases starts lowest with adenine, 2.56 D[46], thymine, 4.31 D[46], uracil, 4.37 D[46], and then highest with cytosine at 6.39 D[46]. With the exception of thymine the increasing dipole value of the nucleobase decreased the amount of energy required to fragment the complex using CID. The CID fragmentation of $A{\cdot}I^{-}$ takes approximately 0.20 V to go from zero fragmentation to complete depletion. This is the longest of all the nucleobases with $U{\cdot}I^{-}$ taking 0.12 V, $C{\cdot}I^{-}$ taking 0.08V and $T{\cdot}I^{-}$ taking only 0.06 V although these values for $U{\cdot}I^{-}$ and $T{\cdot}I^{-}$ are only for the first depletion curve. Total depletion occurs at approximately the same CID value for $A{\cdot}I^{-}$, $T{\cdot}I^{-}$ and $U{\cdot}I^{-}$ at approximately 0.37 V, 0.36 V and 0.38 V respectively while $C{\cdot}I^{-}$ is drastically quicker at only approximately 0.18 V. While these CID fragmentation ranges for the different nucleobases vary considerably in length the CID+UV depletion always completes in a range of always less than 0.10 V for all nucleobases.

For the $U{\cdot}I^{-}$ complex despite vastly different depletion speeds during the range of CID values for S2 both CID and CID+UV results reach a level in S3 at approximately 5% initial intensity which remains at a constant intensity value until S4. As this value is shared by both CID and CID+UV results implies that there are almost certainly two different channels in effect in the $U{\cdot}I^{-}$ results. $T{\cdot}I^{-}$ shows the same as from $U{\cdot}I^{-}$ that two different channels are in effect for the $T{\cdot}I^{-}$ complex. The CID+UV data for all $Nuc{\cdot}I^{-}$ complexes showed no fragment peaks in the results. A proposed theory regarding this is that if any I^{-} fragments are formed from the CID excitation component then the UV photons from the diode laser become capable of ionizing the I^{-} due to the removal of the solvating effect of the nucleobase, an effect which shifts the VDE of the iodide above the diode laser energy.

An additional point to consider is the fact that for the CID data a complete transformation from parent to daughter peak is not observed with a final intensity for the iodide peak being considerably lower than the initial parent peak intensity. This could be due to multiple fragmentation pathways with only one creating the observed I^- peak and another creating a final product without a charge and thus undetectable using this experimental setup. Alternatively the loss might simply be a related to the experimental setup such as the detector’s differing sensitivity for I^- and $Nuc^{\cdot}I^-$ complexes.

3.4.2 Further Discussion of the $U^{\cdot}I^-$ Cluster

From Fig.3.15 it is clear that the UV photon is interacting with the $U^{\cdot}I^-$ complex once CID excitation energy has occurred with several different channels occurring labelled as Peaks E and F. However, the exact total energy for the channels at these peaks is uncertain as CID is a measure of electric field strength in the QIT while the laser beam is in eV per photon, two values which are not directly compatible for addition without further analysis so instead an indirect approach was undertaken by comparison to published literature. Table 3.2 shows the CID electric field values for the Peaks A – F and the ratio between these values and the value for Peak A.

Table 3.2: Table displaying CID electric field values for $U\cdot I^-$ depletion maximums, peaks A - F from Fig.3.17 and Fig.3.18, and the ratio between each peak's value and the value for Peak A. Mid points were taken for the values for the broad peaks D and F. Peaks E and F are in bold as the photon energy has not been included in this table.

	A	B	C	D	**E**	**F**
CID Energy of Depletion Maximum / V	0.12	0.19	0.22	0.34	**0.13**	**0.31**
Ratio To Peak A	1.00	1.58	1.83	2.83	**1.08**	**2.58**

The group by Burrow[47,48,49,50] have published several papers regarding dissociative electron attachment to the uracil molecule. They demonstrated that in the production of the dehydrogenated uracil anion there were two sharp peaks at the electron energies of 0.69 eV and 1.01 eV and one broad peak at 1.7 eV[47,48,49,50].

The values 0.69 eV and 1.01 eV matched to vibrational feshbach resonances between the dipole bound anion and neutral uracil molecule for the second and third vibrational energy levels of the neutral caused by hydrogen tunnelling through the energy barrier to dissociation[48,49,50]. The neutral uracil has a value for the N_1-H vibrational stretch's first vibrational level of 0.432 eV[49] while the dipole bound anion state has a electron binding energy calculated twice as 93±7 meV[51] and 86±8 meV[52]. This value is very low due to the electron in the dipole bound state of uracil having no significant effect on the geometric structure[48], existing instead in a diffuse orbital cloud of the molecule position off the molecular framework[48,] Fig.3.24. This is in contrast to the valence bound state in which the electron occupies the π* orbital of the uracil, altering the molecular geometry by causing ring puckering to take place[48]. The broad value at 1.7 eV was explained as the energy equal to the ^{2}π orbital anion state for uracil[49].

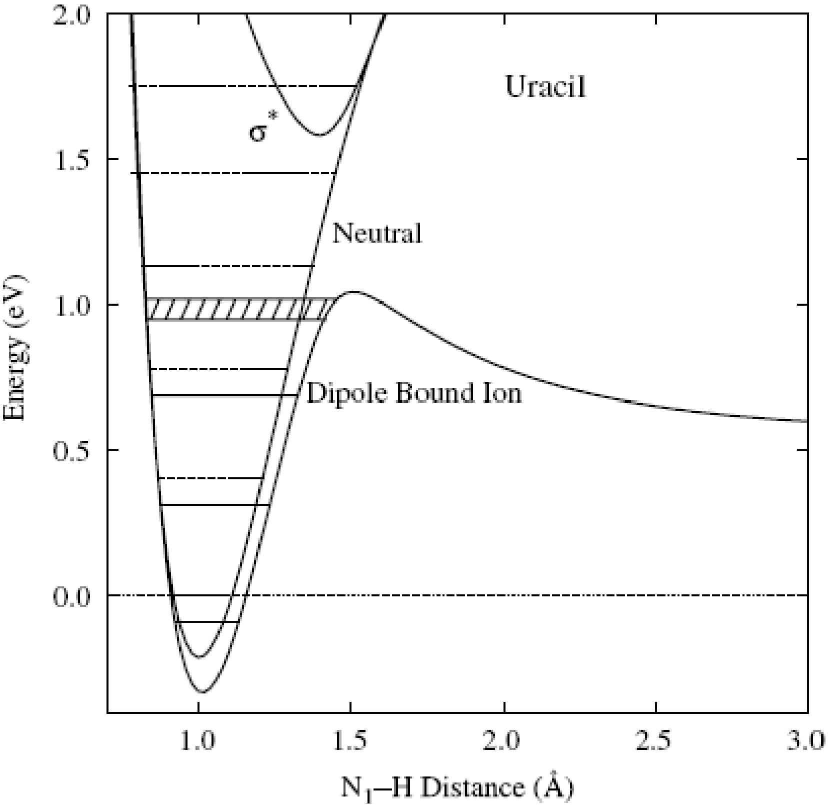

Figure 3.24: Diagram of energy levels of the electron in the dipole bound state, the energy level of the σ* and the neutral state for uracil. Taken from Ref 49.

The ratio between the quoted values of 0.69 eV, 1.01 eV and 1.7 eV from the Burrows results are in a 1 : 1.46 : 2.46 ratio with each other. These line up within 10% of the ratio values for peaks A, B with D being less accurate at just under 15% difference, Table 3.3.

Table 3.3: Table displaying CID energy values and ratios from Table 3.2 with values and ratios from Ref 48 and 49 included.

	A	B	C	D	**E**	**F**
CID Energy of Depletion Maximum / V	0.12	0.19	0.22	0.34	**0.13**	**0.31**
Ratio To Peak A	1.00	1.58	1.83	2.83	**1.08**	**2.58**
Dissociation Energy from Burrow Group from Ref 34 and 35 / eV	0.69	1.01	-	1.7	**-**	**-**
Ratio of Burrow Group Values	1.00	1.46	-	2.46	**-**	**-**

Table 3.3 shows evidence that the peaks A, B and D are connected to the mechanisms from the published data by the Burrow group[47,48,49,50] and that the published values in eV could be used as benchmarks in the construction of a relationship between the strength of the CID electric field and total energy of complex in eV for the $U^{\cdot}I^{-}$ complex, Equation 3.5.

$$(5*E_V)+0.1 = E_{eV} \tag{3.3}$$

Equation 3.5 shows the calculated linear relationship between the electric field strength of the CID, E_V, and the total energy in eV, E_{eV}, with an additional constant added as an adjustment which can be understood as the complex having to already possess energy greater than zero regardless of other factors.

The second and third vibrational feshbach resonances are two of the values used to construct the above relationship for CID into eV, with the first vibrational level not included as there were no published results for that point. This is due to the energy level of the first vibrational level being equal to 0.432 eV[49] which can be seen from Fig.3.24 as lower than the dissociation level disallowing hydrogen tunnelling as a form of dissociation and removing the possibility for the Burrow's experimental setup to record it. However, the cluster excitation presented in this chapter do not relying on this mechanism, so it was possible that evidence for this level would be observable using the current experimental setup. On inspection of Fig.3.15 there is a potentially small dip in the parent peak intensity depletion between the values of 0.10-0.40 V which would correspond to a conversion of 0.15-0.30 eV using Equation 3.3. This is lower than the quoted value for the first vibrational level which might imply that the two are actually not connected or that Equation 3.3 is not fully complete. As an alternative explanation for the dip in intensity the first vibrational stretching band for the dipole bound uracil has a value of 0.34 eV[48] which is closer to the calculated value in eV stated above.

As noted in section 3.1.1, the Martı´nez group[45] have published abinitio calculations of the $U{\cdot}I^-$ complex, specifically a value of 1.2 eV for the dissociation energy of the complex. When that value is used in Equation 3.3 a result of 0.22 V is produced which is in perfect agreement with peak C. This adds further evidence to the relationship created using Equation 3.3 and implying that peak C is related to the dissociation of the complex.

Equation 3.3 was used to convert the CID energy results into total energy in eV plots which are presented in Fig.3.25 and Fig.3.26. Fig.3.26 represents CID+UV results so when interaction with the UV photon is considered combined with CID energy a value of the photon energy, 3.31 eV, must be added to the eV scale to create a value for the total energy of interaction for the complex. This would take the initial range from 0.00-2.10 eV to a new range of 3.31-5.41 eV.

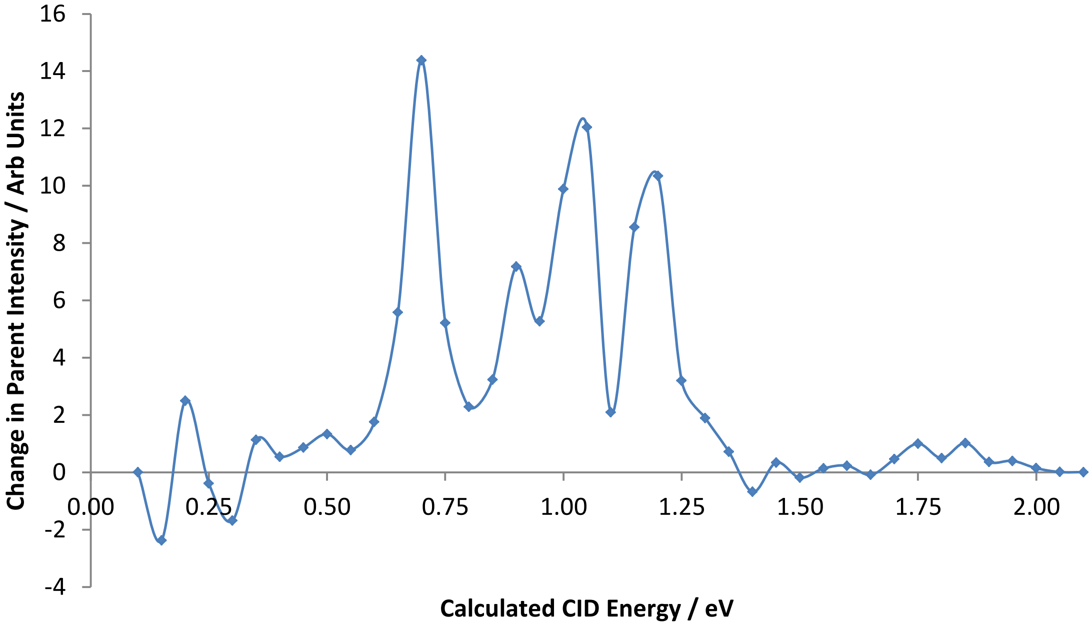

Figure 3.25: Figure 3.17 replotted using Equation 3.3 to convert CID energy to total energy in eV.

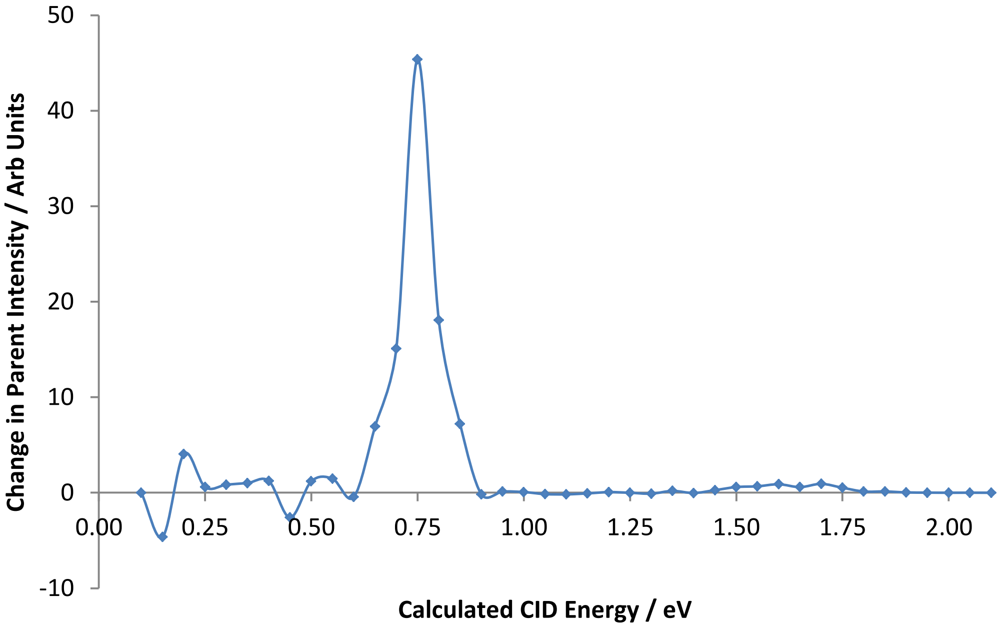

Figure 3.26: Figure 3.18 replotted using Equation 3.3 to convert CID energy to total energy in eV.

Dan Neumark and group have published several papers containing both abinitio calculations and experimental data on the $U{\cdot}I^-$ and the $T{\cdot}I^-$ complexes.[41,42,43]. The experimental work used femtosecond time-resolved photoelectron spectroscopy which gathered experimental results showing time evolution of the energies of the photodetached electron and time dynamics, with computational work including geometric structures for the complexes of the $U{\cdot}I^-$ and $T{\cdot}I^-$ and their charge transferred complexes. The UV energy employed for photoionization of the electron ionizes it from the iodide, and the resulting free electron would either escape from the complex or interact with the π* antibonding orbital of the nucleobase and form a Nuc^- associated to the iodine atom.

The first two papers of Neumark and co-workers studied transient negative ions of the U·I⁻ complex, with the second also covering the T·I⁻ complex. By using two lasers, one to excite the iodide electron until photoionization and the other to probe the electrons kinetic energy and thus to deduce the binding energy, the lifetime and kinetics of the ejected electron were measured and information was extrapolated by the group to fit proposed theories regarding the mechanics of the electron within the complex[43]. The results of the experimental work carried out by the Neumark group are shown in Fig. 3.27 and Fig. 3.28 with key features A – D labelled.

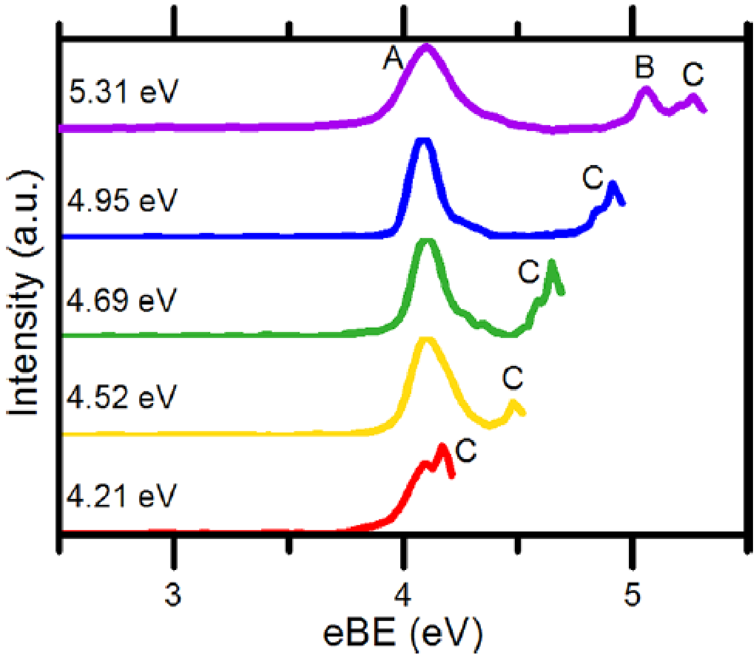

Figure 3.27: One photon photoelectron spectroscopy results for the U·I⁻ complex at different excitation energies with peaks labelled A-C. Taken from Ref 43.

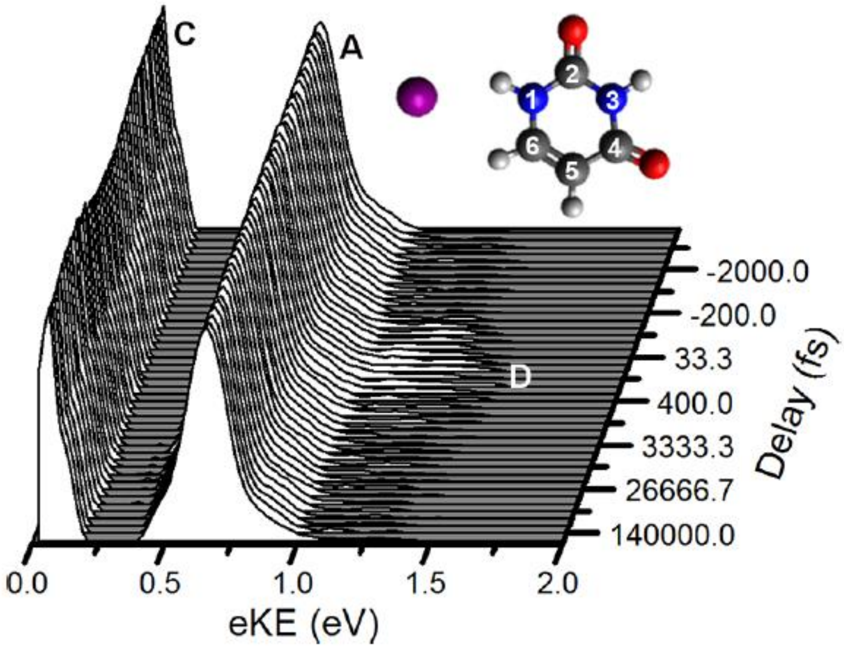

Figure 3.28: Time resolved photoelectron spectroscopy and optimized $U\cdot I^-$ *complex with peaks A, C and D labelled. Taken from Ref 43.*

Feature A, Fig.3.27, has its centre at the binding energy of 4.11±0.05 eV[53], and represents the VDE of iodide in the complex having been shifted due to the interaction with uracil. This is in alignment with the peak E from Fig.3.18 of this work, which is calculated using Equation 3.3 to have an energy of 4.06 eV. Calculations carried out by the Neumark group calculated the VDE at 4.13 eV in good agreement with the above values[53]. Feature C, Fig.3.27 and Fig.3.28, represents zero, or near zero, energy kinetic electrons theorised to have been ejected from the charge transferred state via vibrational autodetachment. The results show it could be seen to exist at a wide range of excitation energies with the most prominent at 4.69 eV[43] and 4.77 eV[42]. However, investigation regarding the results generated in this chapter showed no evidence of any resonance in the results presented here at these energies.

As discussed above, a number of different processes can follow photoexcitation[42,43].

$$[I \cdot U]^{*-} \longrightarrow [I \cdot U] + e^{-} \qquad 3.4a$$

$$[I \cdot U]^{*-} \longrightarrow I \cdot [U - H]^{-} + H \qquad 3.4b$$

$$[I \cdot U]^{*-} \longrightarrow I + U^{*-} \qquad 3.4c$$

$$U^{*-} \longrightarrow U + e^{-} \qquad 3.4d$$

If the assumption is made that the electron does not charge transfer onto the uracil then the depletion for peak E from Fig.3.19 can be assigned to the VDE. However, if the assumption is made that the charge transfer does take place then a number of channels are possible from Equation 3.4a-d that match the results for CID+UV.

One channel is that photoexcitation or vibrational dissociation of the electron occurs after charge transfer which would leave a neutral $U \cdot I$ complex which would be undetectable, Equation 3.4a.

The CID+UV data had no uracil ions detected in the results so Equation 3.4c cannot be the correct channel unless immediately progressing to Equation 3.4d. In Equation 3.4d the uracil anion was formed and the iodine was dissociated followed by the uracil anion then immediately ionized or vibrationally dissociated before reaching the detector which would also account for no fragments in the results.

Hydrogen atom loss from the complex, Equation 3.4b, is the final possibility which would leave a detectable fragment that was different from the parent peak. The Neumark group were unable to detect any evidence for the fragment in their results as the VDE of the electron in that system was calculated to have a value above 3 eV which was impossible to detach using their setup[42,43]. However, this value is in the range of the UV photon from the diode laser from this chapter's setup so the probability of this being formed but also ionized before detection is possible.

In addition to the above there were two further alternative mechanisms that were discussed by Neumark and co-workers but not which should be noted:

- Excitation of the π electron in uracil into the π* orbital which is then followed by charge transfer across from the iodide into the now available π orbital. However, this was deemed unlikely due to trends in recorded results[43].
- A value of 5.30 eV was quoted for a detachment feature to the $^2P_{1/2}$ state of iodide. However, at that high energy all parent intensity would have been depleted using this chapters experimental setup, presuming the equation for CID to eV is correct, so there would be no possibility to observe that channel[29].

A third paper by Neumark and co-workers[41] used the same experimental set up but applied excitation energies that were lower than used before, this time focusing at energies around the VDE of the $U\cdot I^-$ electron, 4.11 eV. The focus of the results of this paper was on the two different bound states of the charge transferred uracil, the dipole bound and the valence bound state[41]. From experimental work the diagram in Fig.3.29 was produced showing the relationship between the dipole bound, valence bound and neutral uracil plotted against energy and ring puckering. It was theorised that there were two different mechanisms for the formation of the valence bound state of the uracil anion both using the dipole bound state as an intermediate, the first mechanism at an energy range of (-110)–100 meV either side of the VDE of the complex, 4.11 eV, and the second mechanism at an energy range of 550-790 meV above the VDE of the complex which are labelled as B and A on Fig.3.29 respectively.

Although there is at first glance a good correlation between the CID+UV data and the transition between states to explain the two depletion curve results of the complex the argument cannot include the UV photon energy in its explanation as the CID data also has the same two depletion curves. This means that any mechanism involvement has to solely depend on the CID excitation energy. That being said, the possibility of the enhanced dissociation of the CID+UV through the change in states as opposed to the CID mechanisms is a possibility.

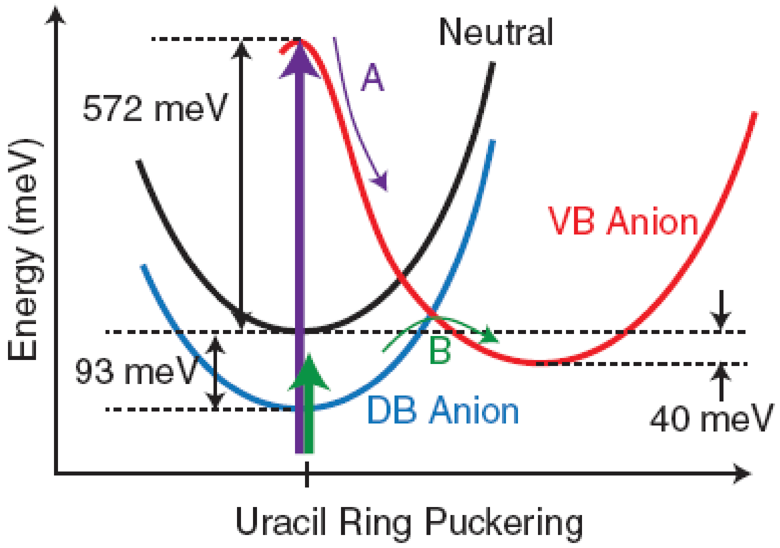

Figure 3.29: Energy level diagram for uracil neutral, dipole bound states, DB anion, and valence bound states, VB anion. Notations A and B represent theorised mechanisms for the transition from DB to VB state. Taken from Ref 41.

3.4.3 $\mathrm{U{\cdot}I^-}$ Cluster Tautomers

The two depletion curves for the $\mathrm{U{\cdot}I^-}$ complex can be explained in terms of tautomers. If the uracil molecule that formed the complex with the iodide was a tautomer of the standard uracil then the chemistry of the complex could be vastly altered, especially if the changes affected the N1 or C6 atoms where the iodide hydrogen bonds onto the nucleobase. A charge transferred state can undergo tautomerization using vibrational energy with an energy barrier quoted as 40 kcal mol^{-1} [42], or approx. 1.7 eV, which matches perfectly with the value of peaks D and F. The increase of the iodide fragment peak intensity increases with increasing CID until the ranges for peaks D and F where any increase is either so low as to be unobservable or none. This would imply that there is a second mechanism at work, different from the first mechanism for the first depletion curve that is depleting the remaining parent peak intensity but not releasing an iodide as a fragment.

If a portion of the solution of complex gathered enough energy in the transfer from solution phase to gas phase that the complex was already in the dipole bound state when it was isolated then the mechanisms from Fig.3.22 can be used with the dipole bound state as an alternative starting point for the complex. In addition Neumark quotes a value of between 550 meV[41] and 790 meV[41] to excite the dipole bound state to form a valence bound state with an approximately average value of 0.670 eV. As already mentioned the calculated value for peak D using Equation 3.3 was 1.8 eV. This value is the right amount for a dipole bound ion to be vibrationally excited enough to transform into a valence bound state which would immediately emit excess energy as the downward vertical transition takes place back to a valence bound ground state which could then continue to be vibrationally excited until dissociation from the valence state took place.

3.5.1 Conclusion

This chapter had the objective of researching the combination of the UV photon with CID excitation energy for the fragmentation and analysis of nucleobases in both experimental work and literature review. There is significant evidence to show that the $U{\cdot}I^-$ and $A{\cdot}I^-$ complexes for the CID+UV excitation data showed enhancement in parent peak depletion over CID excitation. However, there was considerably less, if any, depletion for the $T\cdot I^-$ and $C\cdot I^-$ complexes. This is possibly due to the dissociation energy being lower than the amount of energy required to reduce the electronic energy transition gap, Equation 3.1b.

However, despite its success the UV laser has flaws as a fragmentation tool as discovered in this experimental setup. A major problem is that any fragments created in the ion trap are unable to be shielded from the continuous beam of UV photons and have the possibility of absorbing an additional photon and undergoing secondary reactions. This was demonstrated in the results generated in this chapter where no fragments for CID+UV were recorded despite CID data showing a large peak for iodide for all nucleobases. This means that with the present experimental setup the results recorded cannot be assumed to be only parent peak fragmentation. Alternatively the problem may reside in the continuous wave properties of the diode laser. If this was the case then the addition of a beam chopper would reduce exposure time and could significantly impact results gathered.

Throughout this chapter CID data was collected for the nucleobases with a noticeable trend in the amount of energy required to dissociate the complex, a value that is strongly related to bonding strength of the complexes, compared to the dipole moment, with the exception of $T\cdot I^-$. $A\cdot I^-$ required the largest CID energy to dissociate followed by $U\cdot I^-$, $C\cdot I^-$ then $T\cdot I^-$ compared with the trend in increasing dipole moments with $A\cdot I^-$ as the lowest followed by $T\cdot I^-$, $U\cdot I^-$ and $C\cdot I^-$ as the strongest.

The range of the depletion for each Nuc$^{\cdot}$I^{-} complex with CID interaction varied considerably for each nucleobase. One possible explanation of these observations is the presence of tautomers (Section 3.4.3) where uracil and thymine have significant differences between tautomers that two separate depletion curves are recorded which can be expanded to include the adenine results. For adenine there was a considerably long depletion curve recorded which could be possible if, like uracil and thymine, there existed multiple tautomers of adenine which were close enough in their chemistry with the iodide that the separate depletion curves overlap to the extent that it appears only a single curve exists.

Chapter 4: UV Laser Photodisociation Spectroscopy of the $U^{\cdot}I^{-}$ and $T^{\cdot}I^{-}$ Complexes

4.1 Introduction

In the present day the link between UV radiation and damage caused to DNA is widely known with the photons causing a variety of alterations to the double helix sequence[54,55,56]. However, more recent work has been involved in redefining how the damage is done to the DNA with the inclusion of an indirect channel for radiation damage to DNA as well as the traditional direct channel. Low energy, <3 eV, electrons formed from the absorption of high energy UV photons can cause fragmentation in molecules adjoining the site of absorption leading to fragmentation and recorded loss of hydrogen from the nucleobases[57,58].

Isolated, gas phase anion nucleobase complexes have been the focus of several recent laser spectroscopy studies. Laser photoexcitation of such clusters can provide insight into nucleobase excited state dynamics, as well as nucleobase-free electron interactions. The Dessent group have published results regarding the laser photodisociation spectroscopy of the $U^{\cdot}Pt(CN)_4^{2-}$ and the $U^{\cdot}Pt(CN)_6^{2-}$ complexes[53,59]. Results showing absorption bands in the regions of 4.70eV[59] and 4.90 eV[59] which were assigned to the π–π* chromophore with fragmentation products quoted for complex fission, nucleobase proton transfer and electron detachment.

In Chapter 3 a UV diode laser was used in combination with CID energy to initiate fragmentation of Nuc$\cdot$I^{-} complexes. Although, CID excitation alone resulted in production of the I^{-} fragment for all of the Nuc$\cdot$I^{-} complexes, the UV+CID experiments gave no observable fragment ions despite an enhanced parent ion depletion being observed for U$\cdot$I^{-} and A$\cdot$I^{-}. In this chapter, it is explored whether ionic photofragments are produced by single photon excitation of the Nuc$\cdot$I^{-} complexes using a tuneable pulsed Nd:YAG OPO laser source.

While the UV diode laser generates a continuous laser beam, the OPO laser is a pulsed laser which operates at 10 Hz. When additionally combined with a shutter, the beam was chopped, reducing the amount of laser pulses that interact with an isolated ion packet in the QIT over one isolation phase. This has the advantage of reducing the probability of any ionic fragments absorbing a second photon and thus undergoing secondary fragmentation or electron loss. In addition, the tuneable wavelengths produced by the OPO allow investigation into how cluster fragmentation and cluster depletion varies as a function of wavelength. The wavelength dependant cluster depletion can then be compared to the CID and CID+UV cluster depletion measurements presented in Chapter 3.

The U$\cdot$I^{-} and T$\cdot$I^{-} were chosen for study in this set of experiments, as these cluster have been previously studied by Neumark and co-workers using time resolved photoelectron photodetachment spectroscopy[41,42,43]. These experiments provided evidence for nucleobase-free electron interactions (nucleobase transient negative ions), but key questions remained about the resulting fragmentation channels since ionic photofragments could not be detected with the experimental set up.

4.2 Experimental

The mass spectrometer instrumental details and the ESI processes adopted in this chapter are the same as those outlined in Section 3.2.1. All variable settings, including the ion trap, were adjusted to optimize the required cluster complex intensity in the parent ion mass spectrum. The chemicals used in this chapter are the same as those detailed in Section 3.2.1. The results for the $U{\cdot}I^{-}$ cluster were obtained using the Bruker Esquire mass spectrometer, while the $T{\cdot}I^{-}$ cluster results were obtained on the Bruker AmaZon.

The UV photons were supplied by the Nd:YAG OPO’s outlined in the experimental section. The complexes were scanned by the OPO with a range of set wavelength intervals. For each wavelength a measurement of the parent peak initial intensity was recorded with the laser beam blocked from entering the ion trap, I_O, followed immediately afterwards by a second recording of the parent intensity with the laser beam allowed into the ion trap, I.

The action spectra for both the $U{\cdot}I^{-}$ and $T{\cdot}I^{-}$ complex were recorded across a range of wavelengths with analysis focused on the amount of depletion of the parent peak and any fragments produced. By monitoring the amount of depletion, a measurement that is equivalent to the level of UV absorption for the complex, across a range and by converting the wavelength of the laser beam into eV the results could be plotted in the style of absorption against energy. The absorption of UV photons for parent peaks of both complexes were normalized using Equation 4.1, this allowed for each data point to be more accurately compared to each other with I and I_O representing parent peak intensity with and without laser interaction respectively and with λ and E representing wavelength and energy, in joules, of the laser beam respectively.

$$\frac{\ln\left(\frac{I_O}{I}\right)}{\lambda * E} \qquad 4.1$$

4.3 Results

A representative parent ion mass spectrum is displayed in Fig.4.1, to illustrate that the $U \cdot I^-$ cluster is produced at good ion intensity. A peak corresponding to uncomplexed iodide is also visible.

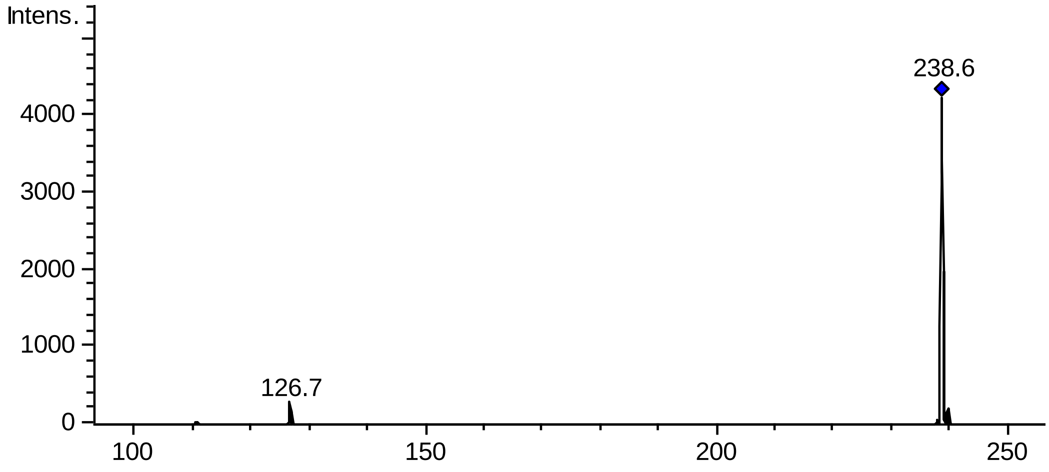

Figure 4.1: Negative ion photofragment mass spectrum of the solution $U \cdot I^-$ *complex. Laser set at 260 nm with energy 0.3 mJ. Peaks 238.6 m/z, 126.7 m/z represent* $U \cdot I^-$ *and* I^- *respectively.*

Fig.4.2 and Fig.4.3 show a distinct increase in the absorption by the parent peak at a maximum energy value of 4.84 eV. A fragment iodide peak is recorded which increases in intensity to coincide with the parent peak reduction with a maximum also at 4.84 eV. This maximum absorption value of 4.84 eV is close to the midpoint for the second depletion curve calculated for $U{\cdot}I^-$ from Chapter 3 of 4.96 eV. The slight difference in the two values can be explained by Equation 3.3 for the conversion of CID to eV producing values that are slightly high once extrapolated above 1.2 eV, the highest value from Chapter 3 that produced good agreement with published data.

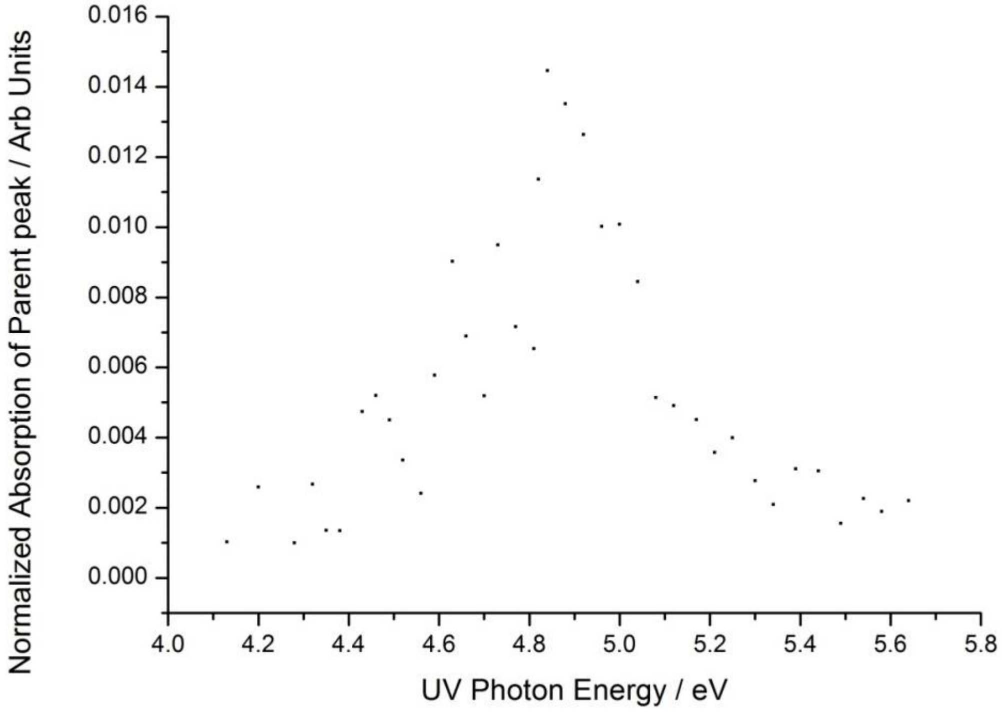

Figure 4.2: Photodepletion (absorption) spectra of $U{\cdot}I^-$ complex parent peak across the 4.0−5.8 eV range.

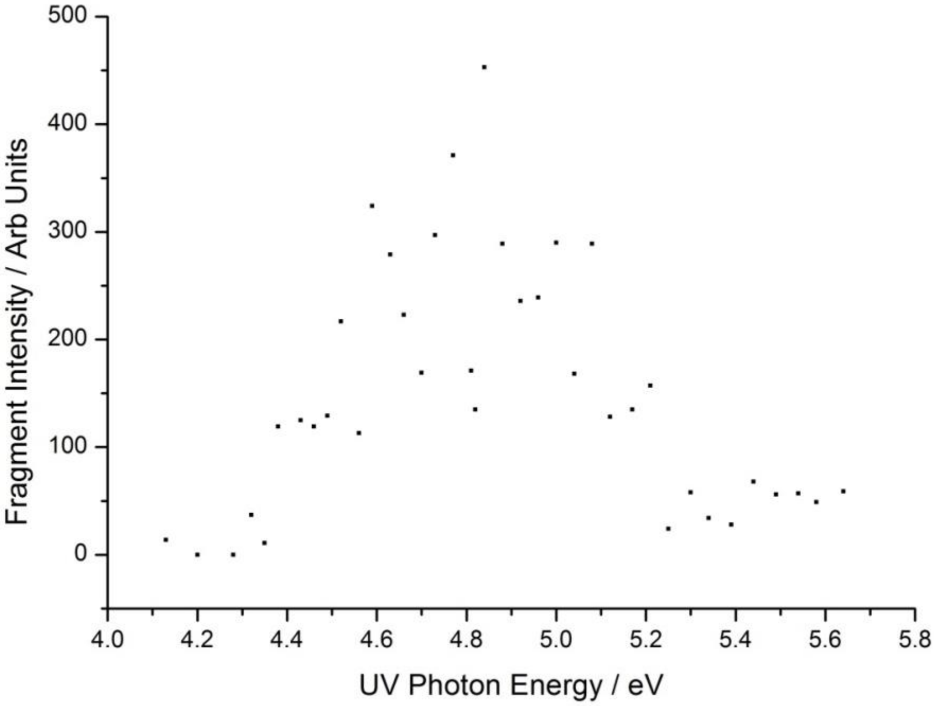

Figure 4.3: Photofragment action spectra of I⁻ complex parent peak across the 4.0−5.8 eV range.

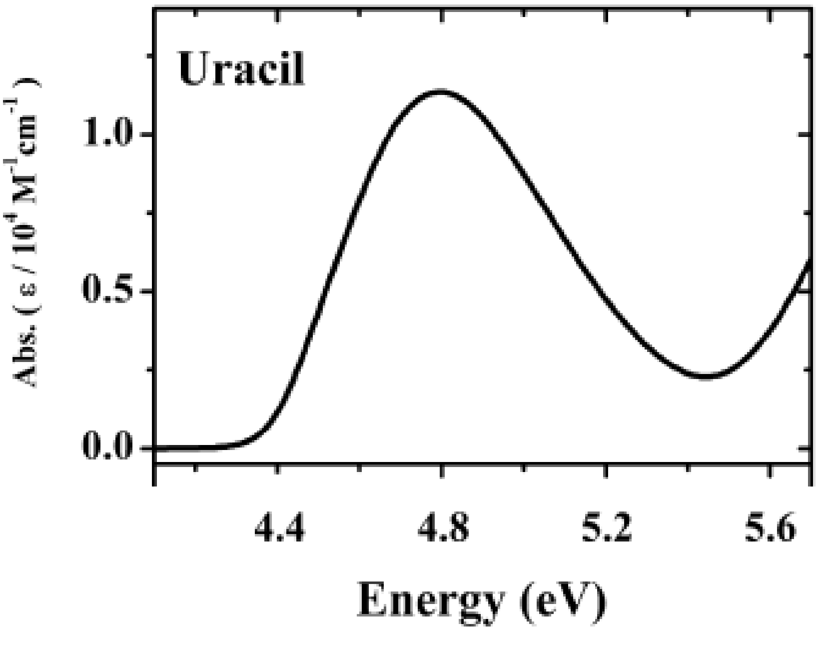

Figure 4.4: Aqueous absorption spectra of Uracil, 0.1 mM highlighting absorption band at 4.8 eV. Taken from Ref 59.

A representative mass spectrum can be seen in Fig.4.5 for the results for the $T^{\cdot}I^{-}$ complex with peaks recorded at 252.6 and 126.6 *m/z* for $T^{\cdot}I^{-}$ and I^{-} respectively.

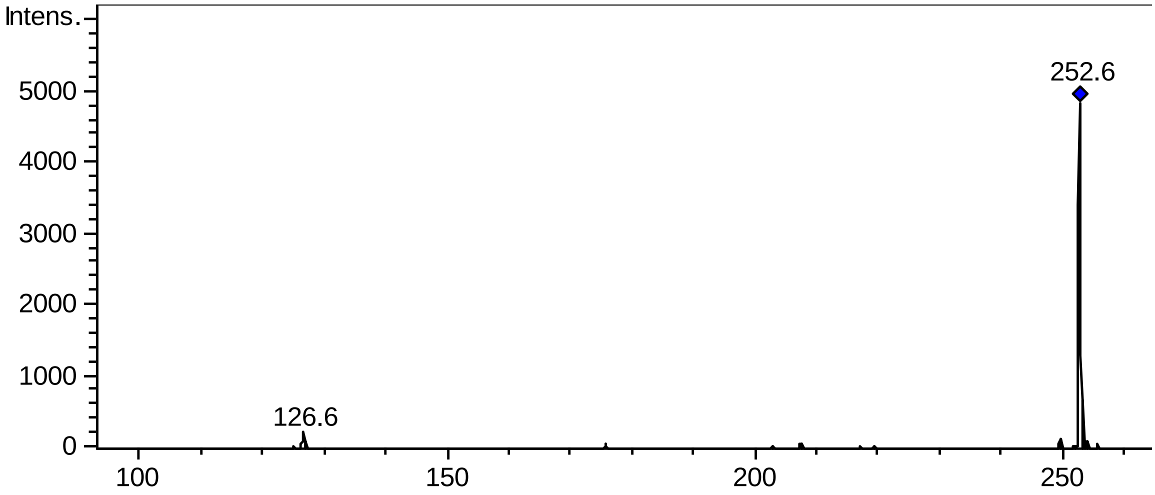

Figure 4.5: Negative ion photofragment mass spectrum of the solution $T^{\cdot}I^{-}$ *complex. Laser set at 260 nm with energy 0.4 mJ. Peaks 252.6 m/z, 126.6 m/z represent* $T^{\cdot}I^{-}$ *and* I^{-} *respectively.*

The results for the thymine complex were repeated twice with two different ranges for photon energy and with different laser beam powers which are displayed in Fig.4.6 and Fig.4.7. Both plots show a distinct increase in both the depletion of the parent peak and a rise in the fragment produced at maximum energy of 4.59-4.86 eV and 4.84 eV respectively while Fig.4.7 shows a second absorption curve with a maximum between 4.00-4.07 eV with iodide also being the only recorded fragment produced for both recorded ranges.

As mentioned iodide was an observable peak in the results and the intensity matched up with the absorption maximums for the parent peak. However, because of the large variation in intensity due to the values being near zero for the iodide peaks the results have not been plotted.

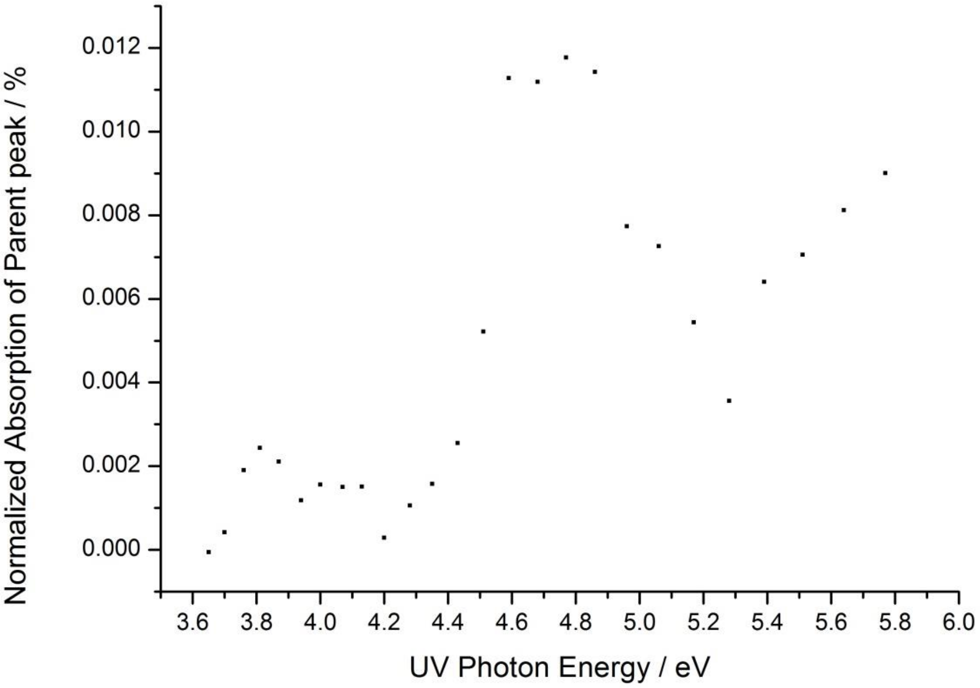

Figure 4.6: Photodepletion (absorption) spectra of $T\cdot I^-$ complex parent peak across the 3.6−5.8 eV range.

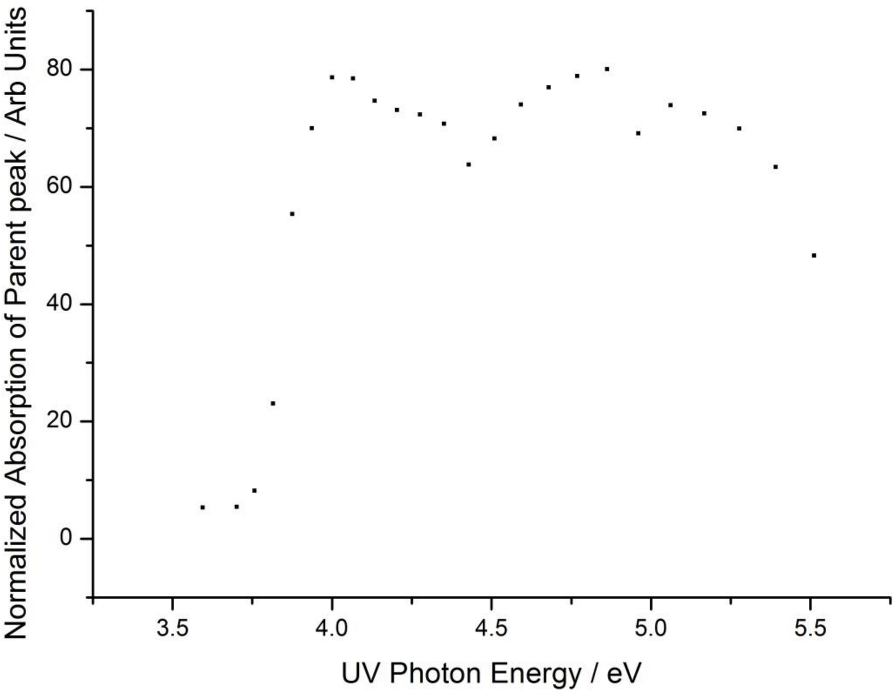

Figure 4.7: Photodepletion (absorption) spectra of $T\cdot I^-$ complex parent peak across the 3.5−5.5 eV range.

4.4 Discussion

The values for the maximum absorptions of the $U{\cdot}I^-$ and $T{\cdot}I^-$ complexes at 4.84 eV and 4.59-4.86 eV respectively compare to the second depletion curves calculated from Chapter 3 with both sets of thymine results having values slightly shifted to lower energies than the uracil results. An alternative theory is that the interaction of the UV photon is at a similar maximum because the iodide is interacting with the photon and not the nucleobase. The reason why the thymine result would be slightly shifted to a lower energy could be explained by the solvating effect of the thymine being slightly less shielding than the effect of the uracil. The maximum absorption of $U{\cdot}I^-$ also matches well with the quoted values from the Dessent group of 4.90 eV and 4.70 eV as maximum absorptions for $Pt(CN)_6^{2-}{\cdot}U$ and $Pt(CN)_4^{2-}{\cdot}U$ complexes respectively[59] and an absorption maximum of 4.8eV can be observed in Fig4.4. These values are reported as being related to the π-π* absorption band for the uracil molecule which was mentioned in Chapter 3 as being antibonding along the N_1-H bond, weakening the complex bonding causing iodide to fragment which is reflected in the results recorded in this chapter.

The results for $T{\cdot}I^-$ in Fig.4.7 show two absorption curves at close proximity while $U{\cdot}I^-$ only shows evidence of one curve. It might have been possible that $U{\cdot}I^-$ would show a second absorption curve but the laser beam energy dropped significantly at the edge of the scanning range, possibly to a point below the required energy to detect fragmentation. If the wavelength range could have been extended below 4 eV with significant laser energy then a different set of results might be possible.

In the $\mathrm{U{\cdot}I^-}$ results there were a few small data points at 111.1 *m/z* which would represent the deprotonated uracil anion. However, this result is highly sceptical due to the almost zero intensity of these peaks with coincidental noise peaks being a more likely explanation.

Although a fragment peak for iodide was recorded for both complexes the difference between parent intensity depleted and iodide fragment formed is very high. For $\mathrm{U{\cdot}I^-}$ the conversion between parent peak depletion and fragment peak formation only equals approximetely 5% at the data point 4.84 eV. This leaves a considerable amount of the parent peaks intensity unacounted for which could be explained by either a second fragmentation mechanism which left only neutral fragments, undetectable by the mass spectrum or simply a problem in the experimental setup such as the detector sensitivity mentioned in Section 3.4.1.

4.5 Conclusion

The results from Chapter 3 for both the $\mathrm{U{\cdot}I^-}$ and $\mathrm{T{\cdot}I^-}$ complexes show second depletion curves. These curves match in energy with the results from this chapter's experimental work. In Chapter 3 one proposal for these second depletion curves was conversion between the dipole and valence bound states using CID energy to convert between the two. However, in this chapter there was no CID energy involved in the experimental procedure so for the proposal of transfer from dipole to valence bound states to still be true the absorption bands from this chapter would have to be coincidentally in the same energy region.

Chapter 5: Study of the Interactions of UV Photons Combined with CID Excitation Energy on Proteins Melittin and Angiotensin

5.1.1 Introduction

The process of UV photodetachment dissociation, UVPD, is an important tool for the gathering of data regarding the sequencing of biomolecules. UVPD is a process which uses UV laser irradiation to ionize an electron from a multiply charged anion to create a oxidised radical species which is often unstable and thus leads to fragmentation[24,61,62,63]. Using the tandem properties of the mass spectrometer the oxidised target ion can be isolated and fragmented using CID excitation in a process labelled activated electron photodetachment, activated-EPD[24]. To photodissociate an electron from the target ion the electron must overcome its binding energy which generally exists across an energy range of 0–5 eV[24]. The diode laser used in this experiment only covers the lower half of this range, 3.31 eV, so if proved plausible there exists a high potential for the preliminary CID excitation in combination with the diode laser for the purpose of sequencing biomolecules.

Comparison of the reaction mechanisms between a UV activated target ion which is then CID fragmented against a target ion which is only CID excited has provided considerable interest regarding the sequencing of peptides and proteins. Work by Dugourd and co-workers has published results for the peptides leucine-enkephalin (protonated) and gramicidin A (sodiated) which has shown that using activated-EPD as a fragmentation tool revealed multiple fragment peaks in the mass spectrum that were not observable with CID excitation alone[60].

Chapter 3 has shown strong evidence for the agreement that CID+UV can fragment a molecular ion, as illustrated for Nuc$\cdot$I^{-} clusters. In this chapter this excitation method is applied to protein ions to observe the effects of the same method on a considerably larger biomolecule and record any findings that occur. In this chapter, the interaction of CID+UV with two proteins is investigated, namely melittin and angiotensin I human acetate, referred hereafter as angiotensin. The structure of angiotensin is displayed in Fig.5.1.

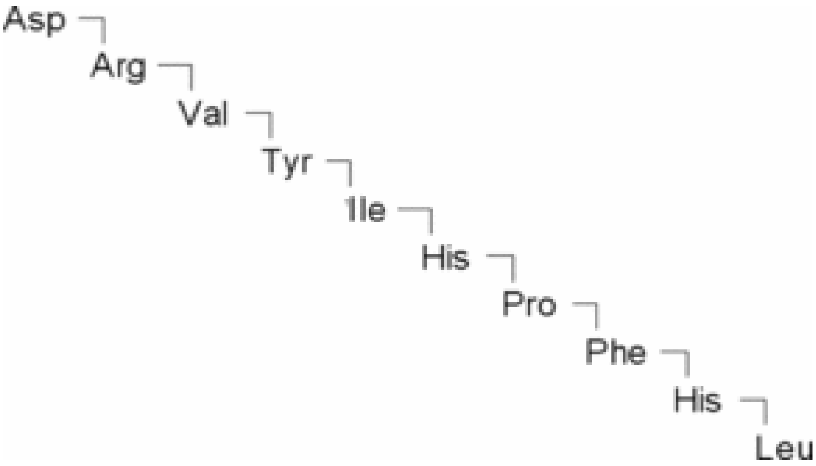

Figure 5.1: The sequence of amino acids in angiotensin. Taken from Ref 64. Asp, aspartic acid, Arg, argenine, Val, valine, Tyr, tyrosine, Ile, isoleucine, His, histidine, Pro, proline, Phe, phenylalanine, Leu, leucine.

Fig 5.2 and Fig.5.3 represent results taken from Ref 24 for the CID and the UVPD fragmentation methods for angiotensin. Fig.5.3 highlights the observable difference in the fragmentation mass spectra obtained using these two methods.

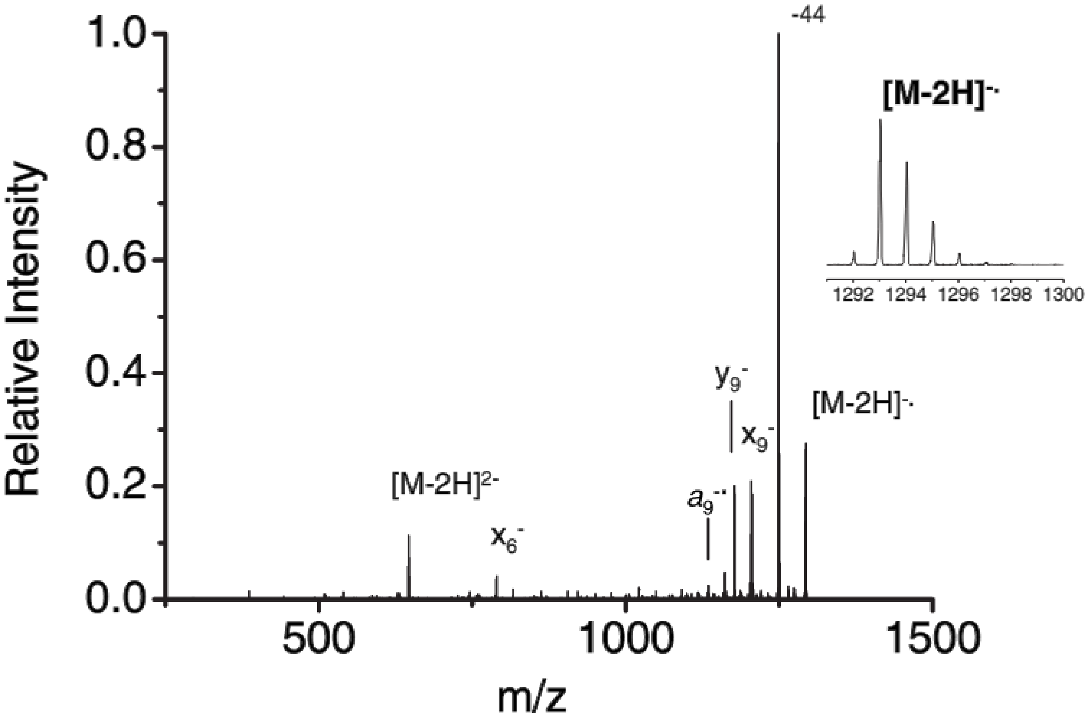

Figure 5.2: Mass spectrum of $[M\text{-}2H]^{2-}$ angiotensin after laser irradiation of 262 nm with parent peak of 647.25 m/z with zoomed insert highlighting doubly deprotonated singly charged angiotensin. Taken from Ref 66.

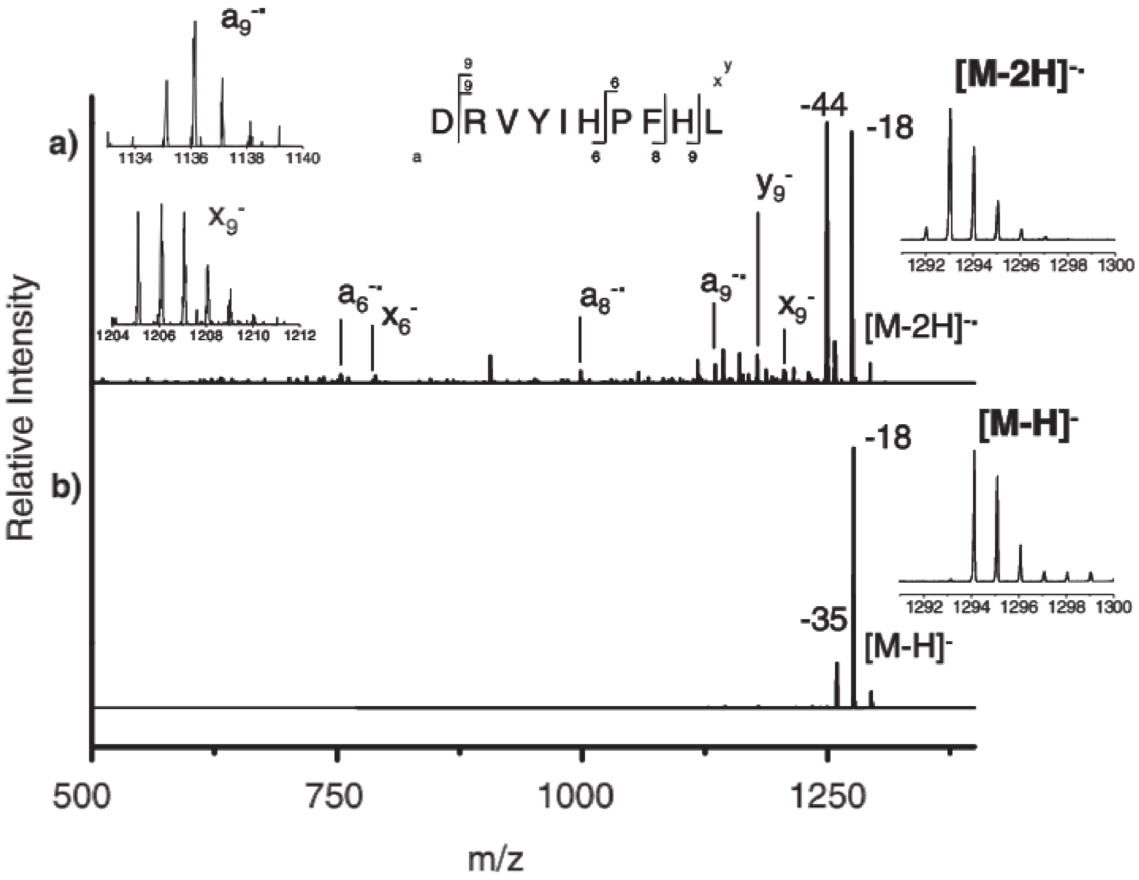

Figure 5.3: a) MS^3 of the isolated [M-2H]$^{2-\cdot}$ Fragment and subsequent CID fragmentation with insert highlighting isolated peak. The isolated fragment was formed via UV ionization of the [M-2H]$^{2-}$ parent peak. b) MS^2 of [M-H]$^-$ parent ion with subsequent CID fragmentation with insert highlighting isolated peak. Significant differences in fragment mass spectra are clearly observed between the two methods. Taken from Ref 66.

5.2.1 Experimental

Both the mass spectrometer setup and the ESI methods employed in this chapter are the same as those described in section 3.2.1. All variable instrument settings were adjusted for detection of the maximum intensity for the target ion. The proteins used in this chapter were purchased from Sigma-Aldrich in solid form powder and dissolved in methanol in a volumetric flask. The proteins studied were isolated in their doubly deprotonated 2- charge states. The dianionic species were selected so that if electron detachment occurred a monoanionic fragment would remain which is still detectable in the mass spectrometer.

5.3.1 Melittin Results

The effects of photodetachment dissociation on melittin were studied by Lemoine and co workers[65]. Using a QIT to isolate the target $[M\text{-}2H]^{2-}$ ion a UV laser beam of 260 nm from a Nd:YAG OPO was applied which was capable of producing the $[M\text{-}2H]^{-\cdot}$ photofragment which was then fragmented further using CID[65].

The $[M\text{-}2H]^{2-}$ anion of Melittin were inside the operating *m/z* range of the mass spectrometer at an *m/z* value of 1422.0 the doubly deprotonated 1- anions, *m/z* of 2844.0, were too high. The AmaZon mass spectrometer settings were altered to run at an extended range to include the 1- charge states but this, however, had a significant trade off against the resolution of the mass spectrometer. The mass spectrum of the Melittin sample with under high resolution settings is displayed in Fig.5.4 with the peak 1422.0 representing the $[M\text{-}2H]^{2-}$ anion.

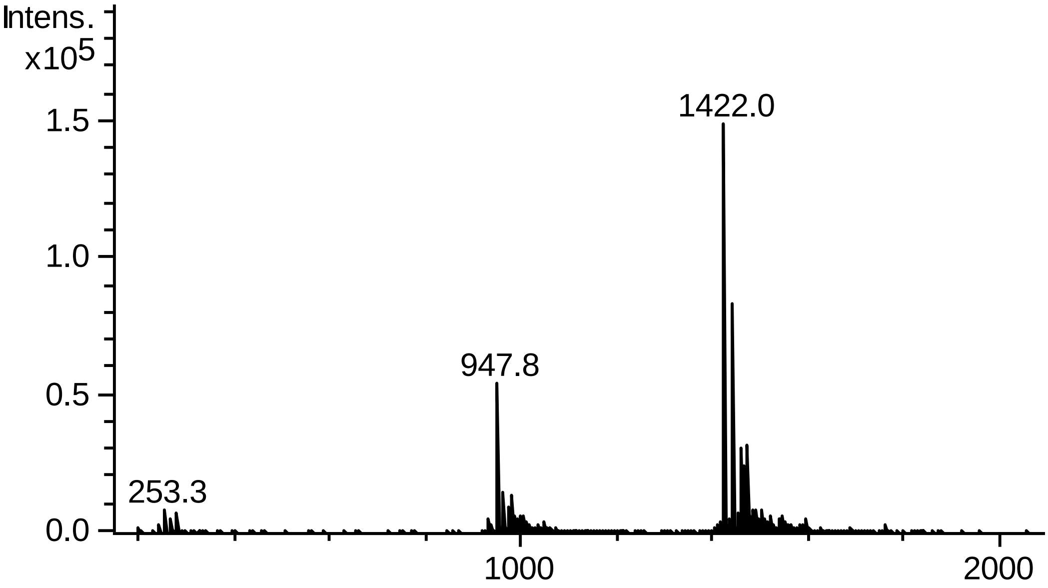

Figure 5.4: Mass spectrum of melittin solution with high resolution.

The chemistry was expected to allow for the ionization of one of the 2- charge state electrons for the doubly deprotonated melittin followed by the CID induced fragmentation of the photofragments[48.] However, due to this it was deemed that melittin was unable to be analysed further using the present experimental setup.

5.3.2 Angiotensin Results

The angiotensin ion contains two different chromophores that can absorb UV photons which are phenol and phenyl[60]. The effects of photodetachment dissociation on angiotensin were also studied by Lemoine and co workers[66]. Using a QIT the target $[M-2H]^{2-}$ ion a UV laser beam of 262 nm from a Nd:YLF was applied which was capable of producing the $[M-2H]^{-\cdot}$ photofragment which was then fragmented further using CID[66]. A second isolation stage on the $[M-2H]^{-}$ photofragment with subsequent low energy CID excitation produced a considerable range of fragments. This is in contrast with the fragmentation peaks observed by just performing isolation plus low energy CID on the [M-2H]$^{-}$ parent ion, where very little fragmentation was observed[66].

Angiotensin has a mass of 1296.48 which means that the [M-2H]$^{2-}$ anion equals a value of 647.24 *m/z* and a [M-2H]$^{-}$ anion equal to 1294.48 *m/z*. As both of these values fit into the mass spectrometer m/z range with the original high resolution settings the analysis could continue with 647.24 as the parent peak.

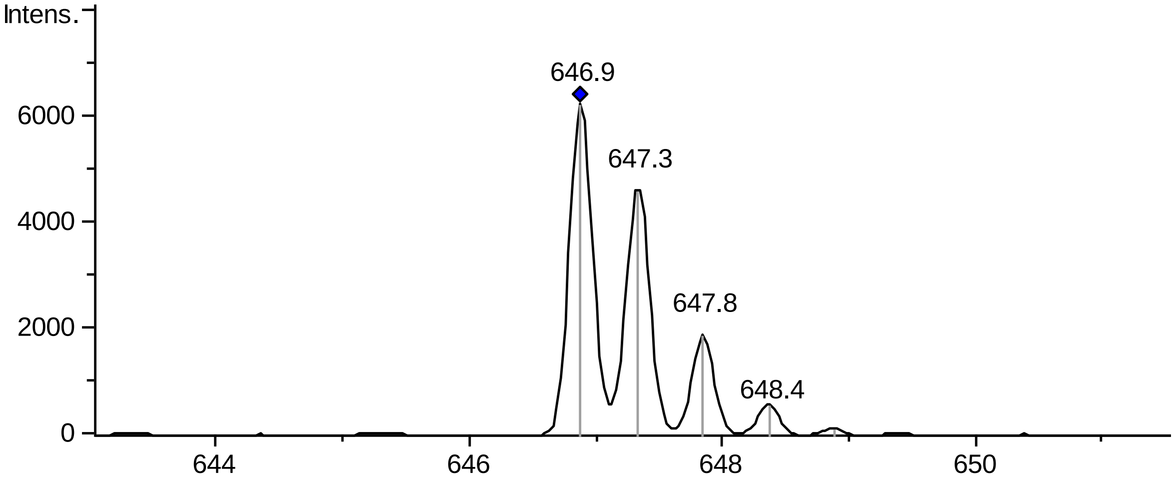

Figure 5.5: Mass spectrum of angiotensin parent peak for [M-2H]$^{2-}$.

Table 5.1 shows results for both observed peaks and not observed peaks from the CID and CID+UV results obtained in this experiment. Values 624.8 *m/z*, 1234.8 *m/z* and 1293.8 *m/z* in bold were not observed in any results but respective 2-/1- *m/z* charged peaks were.

Table 5.1: Table of $[M\text{-}A]^{2-}$ and $[M\text{-}B]^{-}$ fragment peaks from parent peak $[M\text{-}2H]^{2-}$ at 646.9 m/z. ***Bold*** *values* ***624.8*** *m/z,* ***1234.8*** *m/z and* ***1293.8*** *m/z were not observed in results but respective 2-/1- m/z charged peaks were. Peak 1217.7 m/z and peak 1218.6 m/z are from CID+UV and CID results respectively.*

$[M\text{-}A]^{2-}$ Peak / *m/z*	$[M\text{-}B]^{-}$ Peak / *m/z*
599.8	1199.6
608.8	1217.7 / 1218.6
617.4	**1234.8 *(Not Observed)***
624.8 *(Not Observed)*	1249.6
629.9	1258.7
638.3	1275.7
646.9	**1293.8 *(Not Observed)***

Fig.5.6 and Fig.5.7 both show mass spectra of results for angiotensin with CID+UV interaction and represent all the observed peaks in the 2- charge state. There was no observable difference between the fragment peaks for both the CID and CID+UV excitation within the range 598-621 *m/z* so only one set of fragment mass spectra has been included in this thesis. The fragments were observed in groups of approximately 4-6 peaks with each peak approximately 0.5 *m/z* separate. This presented excellent evidence for the parent peak/fragments existing in the 2- charge state as a difference of 0.5 *m/z* equals a gain/loss of 1 mass unit for an ion that is in the 2- charge state. Fig.5.8 and Fig.5.10 display results for CID+UV interaction while Fig.5.9 and Fig.5.11 show results for CID interaction with significant differences between the two sets of results.

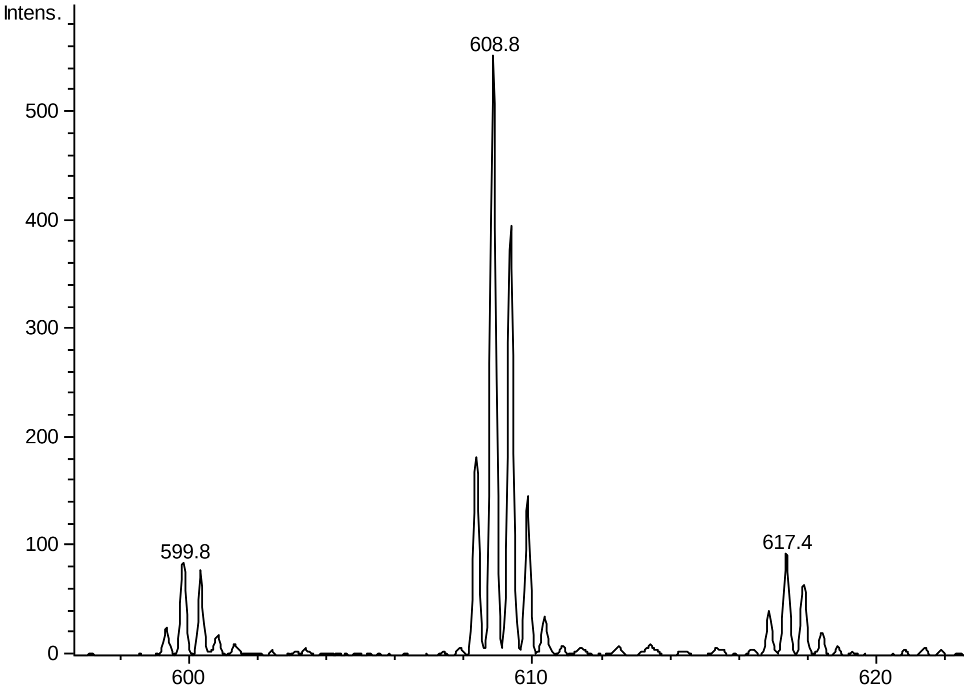

Figure 5.6: Fragment mass spectrum of angiotensin peak 646.9 m/z with CID+UV interaction at a zoomed section of 598-621 m/z. Individual peaks within group have a separation of 0.50 m/z which is representative of 2- charged peaks.

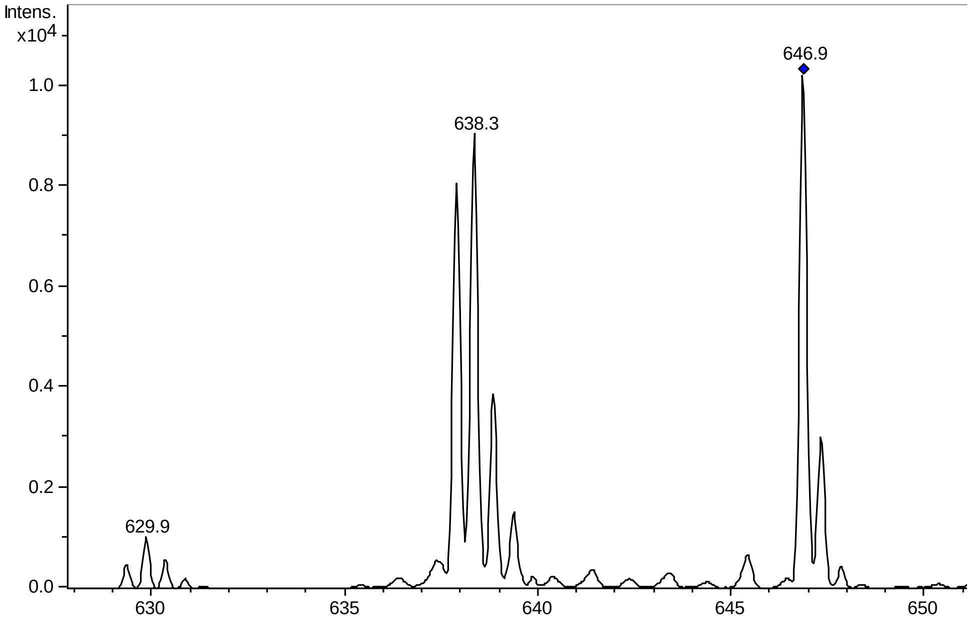

Figure 5.7: Fragment mass spectrum of angiotensin peak 646.9 m/z with CID+UV interaction at a zoomed section of 628-651 m/z. Individual peaks within group have a separation of 0.50 m/z which is representative of 2- charged peaks.

Fig.5.8 and Fig.5.9 show two peaks for the interaction of CID+UV at 1199.5 *m/z* and 1217.7 *m/z* and while the second peak was observable with only CID it was at a considerably lower intensity while the first peak was not observable at all.

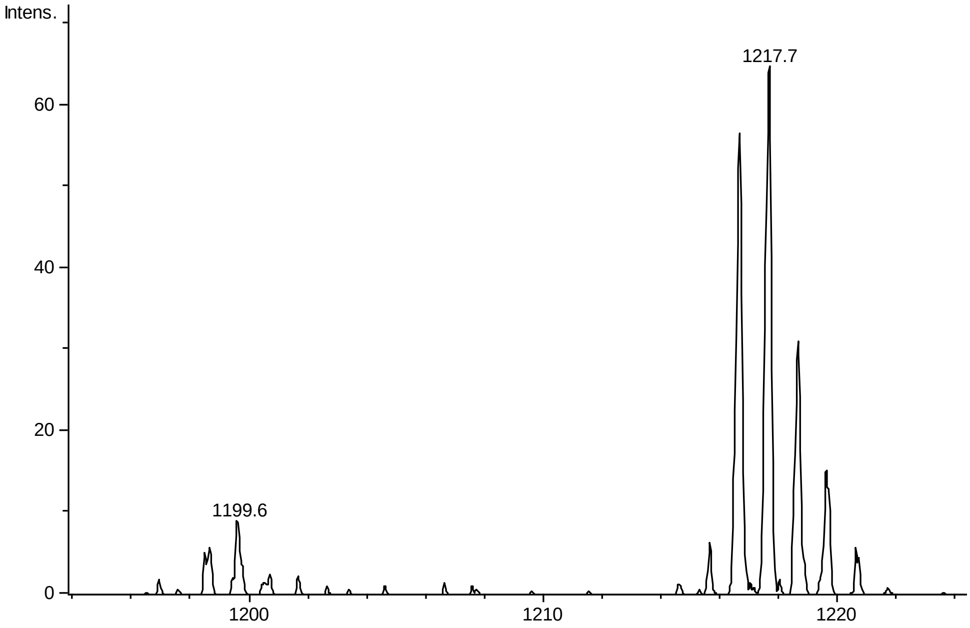

Figure 5.8: Fragment mass spectrum of angiotensin peak 646.9 m/z with CID+UV interaction at a zoomed section of 1217-1223 m/z. Individual peaks within group have a separation of 1.0 m/z which is representative of 1- charged peaks.

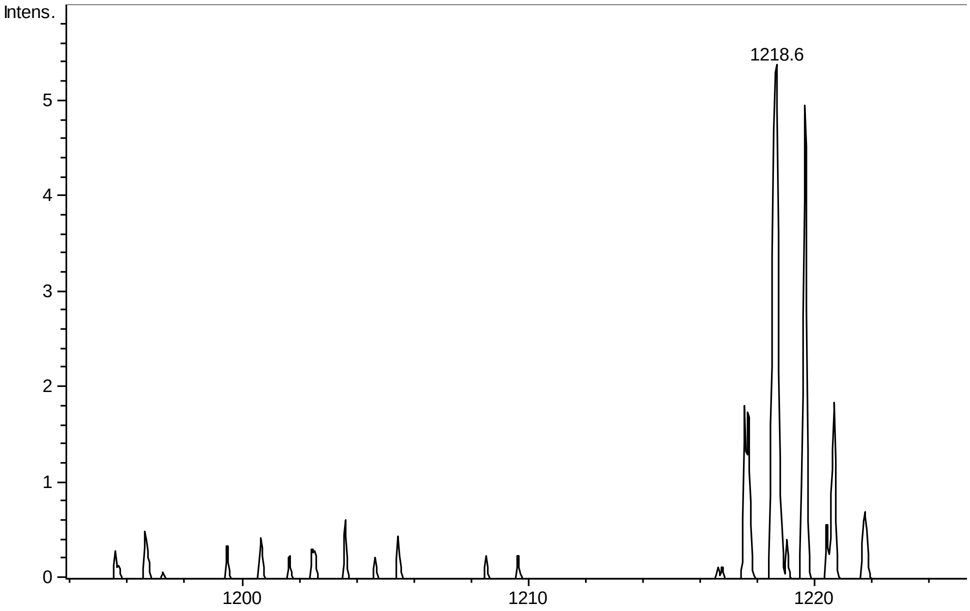

Figure 5.9: Fragment mass spectrum of angiotensin peak 646.9 m/z with CID interaction at a zoomed section of 1217-1223 m/z. Individual peaks within group have a separation of 1.0 m/z which is representative of 1- charged peaks.

For Fig.5.10 and Fig.5.11 three peaks were observable for CID+UV at 1249.6 *m/z*, 1258.7 *m/z* and 1275.7 *m/z* while the same range for CID interaction was without observable fragments.

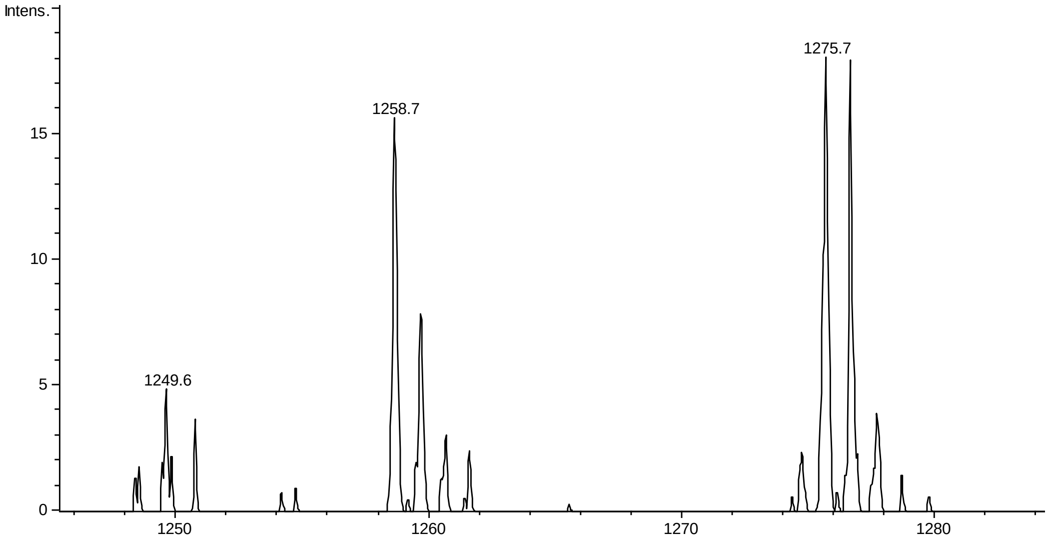

Figure 5.10: Fragment mass spectrum of angiotensin peak 646.9 m/z with CID+UV interaction at a zoomed section of 1248-1282 m/z. Individual peaks within group have a separation of 1.0 m/z which is representative of 1- charged peaks.

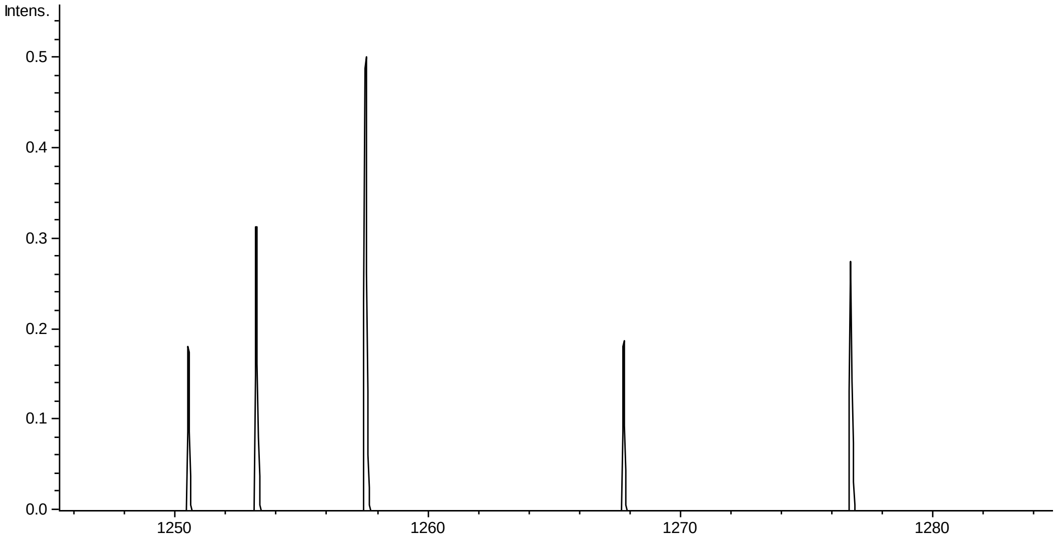

Figure 5.11: Fragment mass spectrum of angiotensin peak 646.9 m/z with CID interaction at a zoomed section of 1248-1282 m/z. Note intensity scale is on a magnitude of 10x Fig.5.10 and without observable peaks.

Further isolation on the fragment peaks for a subsequent further CID stage was not possible in the current experiment as the intensity of the CID+UV fragment ions was not sufficient to allow further analysis.

5.4.1 Discussion

The fragments in the range of 1217-1223 *m/z* showed considerable difference regarding the mass spectra generated for CID and CID+UV. The CID+UV results had a greater population of peaks in this range which lead to a variety of different potential reaction channels. Three different mechanisms are proposed below for the reaction channels regarding these additional CID+UV fragment peaks observed in the data, this is then followed by assignment of each fragment peak to the most likely proposed mechanism:

1. The parent peak ion was fragmented by CID and the resulting fragments were ionized by the UV photon.
2. The parent peak ion was ionized by the UV photon. The oxidised fragment was then fragmented by CID and/or formed an unstable radical anion species which fragmented.
3. The parent peak ion was fragmented by CID and the resulting fragments were ionized by the UV photon. These created oxidised fragments were unstable species which leads to a second fragmentation.

Mechanisms 2 and 3 are supported by research which claims that fragmentation can take place for oligonucleotides in a relatively short period of time after ionization. This was coined as the formation of a ‘hot’ oxidized product where the ionizing photon was greater than the binding energy of the removed electron leaving additional energy in the ion[24].

Peaks 1199.6 *m/z*, 1258.7 *m/z* and 1275.7 *m/z* are observed $[M\text{-}B]^{-}$ fragment peaks and all have respective $[M\text{-}A]^{2-}$ charge peaks observed in the fragmentation mass spectra, Table 5.1. These $[M\text{-}B]^{-}$ peaks are thought to be formed via the photodetachment dissociation from their respective $[M\text{-}A]^{2-}$ fragments, mechanism 1.

Peak 1249.6 *m/z* had no $[M\text{-}A]^{2-}$ peak in the results which eliminates mechanism 1 as a possible source of this peak although both mechanism 2 and 3 are still plausible. The mass of this peak is approximately the loss of a CO_2 group from the $[M\text{-}2H]^{2-}$ parent peak. There has been recorded evidence for the formation of a CO_2^{-} anion via CID excitation which supports the possibility for mechanism 2[67,68]. In Ref 66 a peak was recorded for this mass in regards to UV activation for the ionization of the $[M\text{-}2H]^{2-}$ angiotensin to $[M\text{-}2H]^{-}$ which then fragmented with a loss of 44 *m/z*. This peak was not observed when analysis of the $[M\text{-}2H]^{-}$ charge state was isolated and fragmented without the initial UV activation.

The analysis of the peaks at 1217.7/1218.6 *m/z* was more complex than the previous fragments. This peak was present in both the CID and CID+UV mass spectrum results which would initially imply a reaction channel that was producible through CID alone. However, the intensity was considerably higher for the CID+UV interaction and the ratio of intensities for the individual peaks either side of the central peak were greatly different, thus the different *m/z* values used. This indicates the possibility for a second formation channel with a possible channel outlined below.

The 2- charge state fragment at *m/z* 608.8 was formed through CID as it is present in both CID and CID+UV mass spectra. This fragment peak was then ionized by UV photon interaction into the 1- charge state. This ionized fragment would possess an *m/z* value of 1217.6 which effectively identical to the results for the CID+UV interactions recorded, mechanism 1.

5.5.1 Conclusion

There is significant recorded evidence that CID+UV fragmentation has produced a range of peaks from the model protein angiotensin that would have been unavailable if only one of the tools had been implemented or using both tools to independently generate data.

An analysis of the fragment ions produced indicates that radical formation occurs in the CID+UV fragmentation method which suggests that the process of CID+UV as an ionization tool was successful, however, without the $[M-2H]^{-}$ peak recorded it cannot be certain.

Chapter 6: Final Conclusions

This thesis researched the possibility to link a diode laser with CID excitation to create a new tool for the mass spectrometry analysis of biomolecules. Throughout this thesis there has been significant data both recorded and discussed showing evidence that this new tool has been effective. Chapter 3 showed excellent agreement with the enhancement of parent peak depletion for two of the complexes studied with Chapter 4 showing additional data on the photofragmentation of the uracil and thymine iodide complexes. Chapter 5 created fragment peaks unique to either CID or UV used independently on the protein angiotensin.

Further Work

The research conducted in Chapters 3 and 4 can be furthered by the analysis of different biomolecules and comparing the resulting fragment mass spectra for CID, CID+UV and UV photons from Nd:YAG OPO. As only the uracil and adenine nucleobases when complexed to iodide showed any CID+UV enhanced interaction by using different biomolecules the capabilities of this potential new fragmentation tool could be deduced. Biomolecules that would be of immediate interest would be the nucleosides and nucleotides which contain the original nucleobases in their structure but have additional chemical side chains, which could have varying effects on the reaction channels.

In Chapter 5 the use of CID+UV compared to CID created several different peaks in the fragment mass spectrum. However, the ionized parent peak was unable to be isolated. An alternative experimental setup to the CID excitation would be using IRMPD. The IR laser would be capable of exciting all the bonds in the target ion simultaneously without the intermediate step of a high local energy through collision that requires distribution. The IRMPD+UV ionization tool has the potential to be a significant analytical tool in the analysis of proteins. However, due to the larger activation times required for IRMPD compared to CID an FTICR would be more compatible with the laser.

Abbreviations

A	Adenine
C	Cytosine
CA	Collisional Dissociation
CAD	Collision Activated Dissociation
CID	Collision Induced Dissociation
ECD	Electron Capture Dissociation
EDD	Electron Detachment Dissociation
E_h	Half Energy
EID	Electron Induced Dissociation
EPD	Electron Photodetachment Dissociation
ESI	Electrospray Ionization
ESI-MS	Electrospray Ionization Mass Spectrometry
ICC	Ion Current Control
ICR-SORI CA	Ion Cyclotron Resonance Sustained Off-Resonance Irradiation Collisional Activation
IRMPD	Infrared Multiphoton Dissociation

Nuc	Nucleobase
SID	Surface Induced Dissociation
T	Thymine
U	Uracil
UV	Ultraviolet
UVPD	Ultraviolet Photodisociation
VDE	Vertical Dissociation Energy

References

1. H. E. Duckworth. *Mass spectroscopy*. Great Britain: University Press; 1960.
2. F. W. Aston. *Mass Spectra and isotopes*. London: Edward Arnold Publishers Ltd; 1960.
3. F. A. White. *Mass Spectrometry in Science and Technology*. New York: John Wiley and Sons, Inc; 1968.
4. E. Hoffmann. Tandem Mass Spectrometry: A Primer. *Journal of Mass Spectroscopy.* 1996; **31**, 129-137.
5. B. B. Schneider, D. J. Douglas and D. D. Y. Chen. Ion fragmentation in an electrospray ionization mass spectrometer interface with different gases. *Rapid Communications in Mass Spectrometry*. 2001; **15**: 249-257.
6. R. B. Cole ed. *Electron ionization mass spectrometry. Fundamentals instrumentation and applications*. USA: John Wiley and Sone, Inc; 1997.
7. K. Kowalewska, P. Stefanowicz, T. Ruman, T. Fraczyk, W. Rode and Z. Szewczuk. Electron capture dissociation mass spectrometric analysis of lysine-phosphorylated peptides. *Biosci. Rep*. 2010; **30**: 433-443.
8. S. A. McLuckey and D. E. Goeringer. Slow Heating Methods in Tandem Mass Spectrometry. *Journal of Mass Spectrometry*. 1997; **32**: 461-474.
9. J. M. Wells and S. A. McLuckey. Collision-Induced Dissociation (CID) of Peptides and Proteins. *Methods in Enzymology*. 2005; **402**: 148-185.
10. L. Sleno and D.A. Volmer. Ion activation methods for tandem mass spectrometry. *J. Mass Spectrometry*. 2004; **39**: 1091-1112.
11. J. H. Gross. *Mass Spectrometry*. Second Edition. London: Springer; 2011.

12. E. Hoffmann and V. Stroobant. *Mass Spectrometry*. Principles and Applications. Second Edition. Chichester: John Wiley and Sons, LTD; 2007.
13. R. A. Zubarev, D. M. Horn, E. K. Fridriksson, N. L. Kelleher, N. A. Kruger, M. A. Lewis, B. K. Carpenter and F. W. McLafferty. Electron capture dissociation for structural characterization of multiply charged protein cations. *Anal. Chem*; 2000: **72**, 563-573.
14. H. J. Cooper, K. Hakansson and A. G. Marshall. The role of electron capture dissociation in biomolecular analysis. *Mass Spectrometry Reviews*; 2005: **24**, 201-222.
15. I. Anusiewiez, J. Berdys-Kochanska and J. Simons. Electron attachment step in electron capture dissociation (ECD) and electron transfer dissociation (ETD). *J. Phys. Chem. A*. 2005; **109**, 5801-5813.
16. S. L. Cook, O. L. Collin and G. P. Jackson. Metastable atom-activated dissociation mass spectrometry: leucine/isoleucine differentiation and ring cleavage of proline residues. *Journal of Mass Spectrometry.* 2009: **44**, 1211-1223.
17. J. J. Wolff, T. N. Laremore, F. E. Leach, R. J. Linhardt and I. J. Amster. Electron capture dissociation, electron detachment dissociation, and infrared multiphoton dissociation of sucrose ocatsulfate. *Eur. J. Mass Spectrom*. 2009; **15**, 275-281.
18. R. A. Zubarev. Electron-capture dissociation tandem mass spectrometry. *Current Opinion in Biotechnology*; 2004: **15**, 12-16.
19. D. L. Andrews. *Lasers in Chemistry*. Third Edition. Berlin: Springer; 1997.
20. V. Balzani and F. Scandola. *Supramolecular Photochemistry*. Ney York: Ellis Horwood; 1991.

21. P. Borrell. *Photochemistry: A Primer*. Bungay: Richard Clay, Ltd; 1973.

22. R. B. Cundall and A. Gilbert. *Photochemistry*. London: Nelson; 1970.

23. R. P. Wayne. *Principles and Applications of Photochemistry*. Oxford: Oxford University Press; 1991.

24. R. Antoine, J. Lemoine and P. Dugourd. Electron photodetachment dissociation for structural characterization of synthetic and bio-polymer anions. *Mass Spectrometry Reviews*; 2014: **33**, 501-522.

25. R. J. Nieckarz, J. Oomens, G. Berden, P. Sagulenko and R. Zenobi. Infrared multiple photon dissociation (IRMPD) spectroscopy of oxazine dyes. *Phys. Chem. Chem. Phys*. 2013; **15**, 5049-5056.

26. B. M. Ham. *Even Electron Mass Spectrometry with Biomolecule Applications*. New Jersey: John Wiley and Sons, Inc; 2008.

27. S. Banerjee, S. Mazumdar. Electrospray ionization mass spectrometry: A technique to access the information beyond the molecular weight of the analyte. *International Journal of Analytical Chemistry*. 2012; ID 282574.

28. J. A. Loo. Studying nonconvalent protein complexes by electrospray ionization mass spectrometry. *Mass Spectrometry Reviews*. 1997, **16**, 1-23.

29. J. S. Page, R. T. Kelly, K. Tang and R. D. Smith. Ionization and transmission efficiency in an electrospray ionization-mass spectrometry interface. *American Society for Mass Spectrometry.* 2007, **18**, 1582-1590.

30. J. R. Chapman. *Practical organic mass spectrometry: A guide for chemical and biochemical analysis.* Second Edition. Ney York: John Wiley and Sons, Ltd; 1993.

31. R. B. Cole and A. K. Harrata. Solvent effect on analyte charge state, signal intensity, and stability in negative ion electrospray mass spectrometry;

implications for the mechanism of negative ion formation. *American Society for Mass Spectrometry*. 1993; **4**, 546-556.

32. M. Peschke, U. H. Verkerk and P. Kebarle. Features of the ESI mechanism that affect the observation of multiply charged noncovalent protein complexes and the determination of the association constant by the titration method. *American Society for Mass Spectrometry*. 2004; **15**, 1424-1434.

33. J. D. Williams, K. A. Cox and R. G. Cooks. Resonance Ejection ion trap mass spectrometry and nonlinear field contributions: The effect of scan direction on mass resolution. *Anal. Chem*. 1994; **66**, 725-729.

34. R. E. March. An introduction to quadrupole ion trap mass spectrometry. *Journal of Mass Spectrometry*. 1997; **32**, 351-369.

35. *http://www.doping.chuv.ch/en/lad_home/lad-prestations-laboratoire/lad-prestations-laboratoire-appareils/lad-prestations-laboratoire-appareils-ms.htm* (Accessed 26th July 2015).

36. H. Benson. *University Physics*. Revised Edition. USA: John Wiley and Sons, Inc; 1996.

37. P. Atkins and J. Paula. *Elements of Physical Chemistry*. Fourth Edition. Oxford: Oxford University Press; 2005.

38. F. G. Smith and J. H. Thomson. *Optics*. Second Edition. Chichester: John Wiley and Sons Ltd; 1996.

39. *http://www.optique-ingenieur.org/en/courses/OPI_ang_M01_C01/co/Contenu_21.html* (Accessed 26th July 2015).

40. A. Weinecke and V. Ryzhov. Fundamentals of biomolecule analysis by electrospray ionization mass spectrometry. *Journal of Chemical Education*. 2005; **82**, 99-102.

41. S. B. King, M. A. Yandell, A. B. Stephansen and D. M. Neumark. Time-resolved radiation chemistry: Dynamics of electron attachment to uracil following UV excitation of iodide-uracil complexes. *The Journal of Chemical Physics*. 2014; **141**, 224310.

42. S. B. King, M. A. Yandell and D. Neumark. Time-resolved photoelectron imaging of the iodide-thymine and iodide-uracil binary cluster systems. *The Royal Society of Chemistry*. 2013; **163**, 59-72.

43. M. A. Yandell, S. B. King and D. M. Neumark. Time-resolved radiation chemistry: Photoelectron imaging of transient negative ions of nucleobases. *Journal of the American Chemical Society*. 2013; **135**, 2128-2131.

44. Y. A. Yang and L. A. Bloomfield. Ultraviolet photoelectron spectroscopy and photofragmentation studied of excess electrons in potassium iodide cluster anions. *J. Chem. Phys.* 1992; **96**, 2453-2459.

45. A. Martı´nez, O. Dolgounitcheva, V. G. Zakrzewski and J. V. Ortiz. Nonconventional hydrogen bonds: A theoretical study of $[\text{uracil-L}]^-$ (L=F,Cl, Br, I, Al, Ga, In) complexes. *J. Phys. Chem, A*. 2008; **112**, 10399-10404.

46. J. Sponer, J. Leszczynski and P. Hobza. Electronic properties, hydrogen bonding, stacking, and cation binding of DNA and RNA bases. *Wiley Periodicals, Inc*. 2002; 3-31.

47. P. D. Burrow. Comment on “Radiation damage of biosystems mediated by secondary electrons: Resonant precursors for uracil molecules”. *The Journal of Chemical Physics*. 2005; **122**, 087105.

48. A. M. Scheer, K. Aflatooni, G. A. Gallup and P. Burrow. Bond breaking and temporary anion states in uracil and halouracils: Implications for the DNA bases. *Physical Review Letters*, 2004; **92**, 068102.
49. A.M. Scheer, C. Silvernail, J. A. Belot, K. Aflatooni, G.A. Gallup and P.D. Burrow. Dissociative electron attachment to uracil deuterated at the N_1 and N_3 positions. *Chemical Physics Letters*, 2005; **411**, 46-50.
50. P. D. Burrow, G.A. Gallup and A. M. Scheer. Vibrational feshbach resonances in uracil and thymine. *The Journal of Chemical Physics*, 2006; **124**, 124310.
51. J. H. Hendricks, S. A. Lyapustina, H. L. Clercq. J. T. Snodgrass and K. H. Bowen. Dipole bound, nucleic acids base anions studied via negative ion photoelectron spectroscopy. *The Journal of Chemical Physics*. 1996; **104**, 7788.
52. J. Schiedt, R. Weinkauf, D. M. Neumark and E. W. Schlag. Anion spectroscopy of uracil, thymine and the amino-oxo and amino-hydroxy tautomers of cytosine and their water clusters. *Chemical Physics*. 1998; 511-524.
53. A. Sen, T. F. M. Luxford, N. Yoshikawa and C. E. H. Dessent. Solvent evaporation versus proton transfer in nucleobase-$Pt(CN)_{4,6}^{2-}$ dianion clusters: a collisional excitation and electronic laser photodissociation spectroscopy study. *Phys. Chem. Chem. Phys*. 2014; **16**, 15490-15500.
54. R. P. Sinha and D. Hader. UV-induced DNA damage and repair: A review. *The Royal Society of Chemistry and Owner Societies*.2002; **1**, 225-236.

55. R. P. Rastogi, Richa, A. Kumar, M. B. Tyagi and R. P. Sinha. Molecular mechanisms of ultraviolet radiation-induced DNA damage and repair. *Journal of Nucleic Acids*. 2010; **592980**.

56. D. T. Ribeiro, C. Madzak, A. Sarasin, P. D. Mascio, H. Sies and C. F. M. Menck. Singlet oxygen induced DNA damage and mutagenicity in a single-stranded SV40-based shuttle vector. *Photochemistry and Photobiology*. 1992; **55**, 39-45.

57. I. Bald, E. Illenberger and J. Kopyra. Damage of DNA by low energy electrons (<3eV). *Journal of Physics*. 2012; **373**, 012008.

58. J. Ravanat, T. Douki and J. Cadet. Direct and indirect effects of UV radiation on DNA and its components. *Journal of Photochemistry and Photobiology B*. 2001; **63**, 88-102.

59. A. Sen and C. E. H. Dessent. Mapping the photophysics of platinum metal complexes bound to nucleobases: Laser spectroscopy of isolated $\text{uracil}{\cdot}\text{Pt(CN)}_4^{2-}$ and $\text{uracil}{\cdot}\text{Pt(CN)}_6^{2-}$ complexes. *The Journal of Physical Chemistry Letters*. 2014; **5**, 3281-3285.

60. T. Tabarin, R. Antoine, M. Broyer and P. Dugourd. Specific photodissociation of peptides with multi-stage mass spectrometry. *Rapid Communications in Mass Spectrometry*. 2005; **19**, 2883-2892.

61. J. P. Reilly. Ultraviolet photofragmentation of biomolecular ions. *Mass Spectrometry Reviews*. 2009; **28**, 425-447.

62. S. Soorkia, C. Dehon, S. S. Kumar, M. Pedrazzani, E. Frantzen, B. Lucas, M. Barat, J. A. Fayeton and C. Jouvet. UV photofragmentation dynamics of protonated cysteine: Disulfide bond rupture. *J. Phys. Chem. Lett.* 2014; **5**, 1110-1116.

63. M. S. Thompson, W. Cui and J. P. Reilly. Factors that impact the vacuum ultraviolet photofragmentation of peptide ions. *J. Am. Soc. Mass Spectrom.* 2007;**18**, 1439-1452.
64. *http://www.sigmaaldrich.com/catalog/product/sigma/a9650?lang=en&region=GB* (Accessed 28Jun2015).
65. V. Larraillet, R. Antoine, P. Dugourd and J. Lemoine. Activated-electron photodetachment dissociation for the structural characterization of protein polyanions. *Anal. Chem*. 2009; **81**, 8410-8416.
66. R. Antoine, L. Joly, T. Tabarin, M. Broyer, P. Bugourd and J. Lemoine. Photo-induced formation of radical anion peptides. Electron photodetachment dissociation experiments. *Rapid Communications in Mass Spectrometry*. 2007; **21**, 265-268.
67. D. Schröder, C. A. Schalley, J. N. Harvey and H. Schwarz. On the formation of the carbon dioxide anion radical $CO_2^{-\cdot}$ in the gas phase. *International Journal of Mass Spectrometry*. 1999; **185-187**, 25-35.
68. M. V. Muftakhov, Y. V. Vasil’ev and V. A. Mazunov. Determination affinity of carbonyl radicals by means of negative ion mass spectrometry. *Rapid Communications in Mass Spectrometry*. 1999; **13**, 1104-1108.
69. J. Hawkes and I. Latimer. *Lasers*. Theory and Practice. New York: Pearson Education; 1995.